

Dielectric Resonator Antenna and Array Concepts based on Glass, Ceramics and Glass-ceramics

Dem Fachbereich Elektrotechnik und Informationstechnik der
Technischen Universität Darmstadt zur Erlangung des
akademischen Grades eines Doktor-Ingenieurs (Dr.-Ing.) vorgelegte

Dissertation

von

M.Sc.

Arshad Mehmood

geboren am 01. March 1984 in Peshawar, Pakistan.

Referent: Prof. Dr.-Ing. Rolf Jakoby
Korreferent: Prof. Dr.-Ing. Klaus Solbach
Tag der Einreichung: 02.02.2017
Tag der mündlichen Prüfung: 23.06.2017

D17

Darmstadt 2017

Mehmood, Arshad : Dielectric Resonator Antenna and Array Concepts based on Glass, Ceramics and Glass-ceramics
Darmstadt, Technische Universität Darmstadt,
Jahr der Veröffentlichung der Dissertation auf TUpriints: 2018
Tag der mündlichen Prüfung: 23.06.2017

Veröffentlicht unter CC BY-SA 4.0 International

Abstract

The focus of this work has been the exploration of different concepts of the dielectric resonator antennas. Mainly, a new kind of glass-ceramic material was characterized and used for making different dielectric loaded or dielectric resonator antennas and corresponding arrays based on such radiating elements. The measurements were carried out on different glass-ceramic compositions and showed a permittivity ϵ_r ranging from 21 to 38 with Qf product in the range from 1500 to 10 000 GHz. Patch antennas for the GPS band using glass-ceramic loading were successfully fabricated and tested. The transparent property of the non-ceramized glass was used for making transparent antennas in combination with a solar-cell module for future energy-autonomous units. Its functionality was demonstrated with a measured gain of 4 dB. Another novel concept of tilted beam dielectric resonator antenna was also successfully tested. The beam was measured to be tilted at 30° from the broadside. The prototype was manufactured by using commonly available alumina substrate material and cutting it with laser, thus providing an easy fabrication method. The tilted dielectric resonator antenna element has also been used to fabricate fixed beam arrays at 0° , 30° and 60° beams. This proved the concept of using the tilted beam dielectric resonator antennas for better lower elevation angle coverage.

Another major part of the work was concerned with realizing the phased arrays with dielectric resonator antennas as radiating elements. Two phased array demonstrators were fabricated in 1×4 configuration. One of the array consisted of liquid crystal based delay lines in inverted microstrip technology. It was fabricated with 10 GHz target frequency and successfully showed steering of the beams in -25° and $+25^\circ$. The second array was based on Barium Strontium Titanate phase shifters in the metal-insulator-metal configuration. This array used stacked dielectric resonator antennas for a wide bandwidth at center frequency of 8 GHz and showed beam steering of -30° and $+30^\circ$.

Kurzfassung

Der Fokus der vorliegenden Arbeit liegt auf der Untersuchung verschiedener Konzepte für dielektrische Resonatorantennen. In erster Linie wurde dazu eine neueartige Glaskeramik charakterisiert und zur Herstellung unterschiedlicher dielektrisch belasteter Antennen bzw. dielektrischer Resonator-Antennen genutzt und zu Arrays verbaut. Die Messungen wurden an verschiedenen Zusammensetzungen der Glaskeramik durchgeführt und lieferten Permittivitäten ϵ_r im Bereich von 21 bis 38 bei einem Qf Produkt im Bereich von 1500 bis 10 000 GHz. Patchantennen auf Basis der Glaskeramiken wurden für das GPS-Band entworfen, aufgebaut und getestet. Die nicht-keramischen Gläser wurden aufgrund ihrer Lichtdurchlässigkeit zur Herstellung transparenter Antennen zusammen mit Solarzellen genutzt, was in Zukunft kombinierte Module für energieautonome Systeme ermöglicht. Ihre Funktion wurde anhand eines Moduls mit 4 dB Gewinn demonstriert. Ein weiteres neuartiges Konzept, eine dielektrische Resonatorantenne mit einem gegenüber Broadside um 30° geneigten Strahl (tilted beam) wurde ebenfalls erfolgreich vermessen. Der Prototyp wurde auf handelsüblichem Aluminasubstrat hergestellt und mit Laser zugeschnitten, so dass eine einfache Herstellung sichergestellt ist. Mit dem Konzept der geneigten dielektrischen Resonatorantenne wurden statische Arrays mit Strahlrichtung von 0° , 30° und 60° hergestellt. Damit konnte gezeigt werden, dass geneigte dielektrische Resonatorantennen geeignet sind, um niedrige Elevationswinkel besser abzudecken. Ein weiterer wesentlicher Teil der vorliegenden Arbeit beschäftigt sich mit der Realisierung von phasengesteuerten Gruppenantennen mit dielektrischen Resonatoren als Einzelemente. Zwei Antennendemonstratoren in 1×4 -Konfiguration wurden aufgebaut. Der erste basiert auf flüssigkristallbasierten Verzögerungsleitungen in invertierter Mikrostreifenleitungstopologie. Er wurde für den Betrieb bei 10 GHz entworfen und demonstrierte einen Strahlschwenk von -25° bis 25° . Der zweite basiert auf Barium-Strontium-Titanat-Phasenschiebern in Metall-Isolator-Metall-Konfiguration. Er nutzt gestapelte dielektrische Resonatorantennen, um eine hohe Bandbreite um die Mittelfrequenz von 8 GHz und einen Strahlschwenk von -30° bis 30° zu erzielen.

Acknowledgements

This thesis is the result of the research i undertook at the Institute of Microwaves and Photonics. In the first place i am very grateful to the support from the Higher Education Commission(Pakistan) and German Academic Exchange Program(DAAD) who made it possible for me.

I would like express my deepest gratitude to Prof. Rolf Jakoby for providing me the opportunity. Not only for the research opportunity but also the support, trust and openness that is a part of your personality.

Next, i would like to appreciate all the help i got from the colleagues at work. Dr.-Ing Yuliang Zheng and Dr.-Ing Andreas Penirschke were my first mentors into the topics, so thank you for that. Thank you to my office mate Dr.-Ing. Bernd Kubina, for the discussions and help especially for various German translations. I would also thank Dr.-Ing Holger Maune for instantly solving the problems whenever i approached him.

Dr. Martin Letz at SCHOTT AG was always very helpful and understanding in the course of the project. Dr. Martun Hovhanisyan and Dr. Hubertus Braun who always had a lot of new samples for the measurements, sometimes with quite artistic textures.

My colleagues in the ALCAN project Muhammed Ayluctarhan, Muhammad Kashan Mobeen, Esat Sibay, Mustafa Bülbül and Christian Weickhmann who always reminded me and kept me on my toes for writing up this thesis along with the project work. At the finish line i can thank you all for that indeed. A special thanks goes to Dr.-Ing Onur Hamza Karabey who is good friend and always took special interest in the completion of my thesis.

In the end i must also acknowledge my family (Parents and siblings) who waited for a long time to see this day and always had the question of 'when are you finishing'. At this very moment i must acknowledge my father, without whom i would not be here, not just biologically but in all other aspects as well. I will end, by mentioning my wife who had to spent many evenings/weekends without me due to the double work i had in the last months. A mere thank-you would be just a small word for all the toll my wife had to bear with three small (but naughty) girls at home when i was working in the odd timings.

Contents

Abstract	ii
Kurzfassung	iii
1 Introduction	1
2 Fundamentals of Dielectric Resonator Antennas and Glass-Ceramics	3
2.1 Dielectric resonator antennas	3
2.2 Glass, ceramics and glass-ceramics	6
2.3 Microwave characterization of bulk-glass ceramics	9
2.4 Homogeneity test of bulk-glass ceramic	14
2.5 Chemical etching of non-ceramized glass	16
2.6 Results of promising glass-ceramic materials	17
3 Dielectric Resonator Antenna (DRA) Elements	18
3.1 Dielectric resonator antennas based on glass-ceramics	18
3.1.1 Glass-ceramic based patch antennas	18
3.1.2 Dielectric resonator antenna modes	34
3.1.3 Dual-band hybrid monopole dielectric resonator antenna	34
3.2 Transparent antennas	39
3.2.1 Transparent antenna from non-ceramized low loss high-k glass	41
3.2.2 Transparent antenna demonstrator on top of a solar cell module	47
3.3 Tilted dielectric resonator antenna made of Alumina	55
4 Dielectric Resonator Antenna (DRA) based Arrays	68
4.1 Fixed beam array based on tilted DRAs	71
4.2 Beam-steering DRA based arrays	77
4.2.1 Liquid Crystal based phased array	84
4.2.2 Barium Strontium Titanate based phased array	94
5 Summary and Outlook	105
Bibliography	108
Awards and Publications	116
Supervised Work	119

Abbreviations and Nomenclature

DRA	Dielectric R esonator A ntenna
LC	Liquid C rystal
BST	Barium S trontium T itanate
GPS	Global P ositioning S ystem
WLAN	Wireless L ocal A rea N etwork
TE	Transverse E lectric
TM	Transverse M agnetic
HE	Hybrid mode with \mathbf{E}_z field dominant
λ_0	Free space wavelength
ϵ_r	Dielectric constant
$\tan\delta$	Dielectric loss tangent
$\mathbf{J}_n(\mathbf{x})$	nth order Bessel function of first kind

*Dedicated to all humans who thrive for knowledge and use it for
peaceful purposes and the person who is most happiest at this
occasion*

Chapter 1

Introduction

The field of antennas have seen a vast expansion. Many different antenna types have been developed according to specific application areas. In the last two decades a new kind of antenna research have gained momentum, known as dielectric resonator antenna (DRA). Although envisioned as early as 1939 [1], the practical feasibility only came along just thirty years ago [2]. As opposed to usual antennas, which almost always use a metal for radiation, a DRA on the contrary, uses no metal at all. It consists only of (ideally) high permittivity and low loss material. Therefore, microwave dielectric material with suitable characteristics namely relative permittivity ϵ_r in range from 10 to 40, loss tangent $\tan\delta$ in the range of 10^{-2} to 10^{-3} and temperature coefficient of resonance frequency τ_f close to 0 $ppm/^\circ C$ are of utmost importance when used for making DRAs.

The progress in telecommunications industry in the last two decades has given rise to a growing demand for low loss dielectric ceramic material. The microwave dielectric materials which are sintered ceramics, have existed now since more than half century. There have been constant improvements that are coming along. The growth is mainly triggered by the necessity of miniaturization of components for the wireless industry [3].

The aim of this work is two fold. First, to investigate a new kind of material known as glass-ceramics for microwave antenna applications. The material although is inferior in terms of loss tangent, but has other advantages such as non-porosity, homogeneity and less batch to batch variation of properties. For investigating these properties of the glass-ceramics, extensive microwave measurements were performed on different batches of glass-ceramic materials prepared at *SCHOTTAG Mainz*. The suitable material batches were identified and DRAs were fabricated with it and tested. Second, to investigate different novel concepts of DRAs such as transparent or directed beam DRAs. Such

antenna concepts are convenient only when DRAs are used as opposed to conventional antennas such as patch or slots.

The thesis arrangement is according to the category of DRA configuration either as single element or array. Chapter 2 explains some background on DRAs and glass-ceramics. It also contains the fundamental investigations performed on the glass-ceramics along with the measurements. A list of promising glass-ceramic materials found during the course of this study are given in the end of the chapter. Chapter 3 discusses the single element antennas. It includes the patch antennas and hybrid dielectric resonator antennas based on glass-ceramics. Followed by the transparent antenna concept, which uses the transparent high-k low loss glass material. The final section contains novel tilted DRA antenna fabricated by laser cutting of Alumina material.

After presenting single elements in Chapter 3, Chapter 4 discusses arrays of DRA radiating elements. It contains a fixed beam array by using the tilted DRAs as well as beam-steering arrays based on Liquid Crystal (LC) and Barium Strontium Titanate (BST) phase shifters. Finally, a summary including an outlook is presented in Chapter 5.

Chapter 2

Fundamentals of Dielectric Resonator Antennas and Glass-Ceramics

This chapter will introduce some of the background information about the dielectric resonator antennas and some basic terminologies of material science in general and glass-ceramics in particular. Some of the material related work done during the course of this work will also be stated here.

2.1 Dielectric resonator antennas

The idea of a dielectric resonator antenna can be dated back to 1939 when Richtmeyer [1] suggested that dielectric material alone without metalization can support resonance phenomenon and hence be used as resonators. The practical demonstration for the DRA, had to wait almost half a century as there were no adequate materials available. In 1983 S.A.Long for the first time demonstrated practically working DRAs. He used perfectly conducting magnetic wall boundary approximations for modeling the cylindrical shaped DRA. In the last three decades many people have investigated different DRAs for many applications. In [4], a very informative summary of applications of DRA has been given. DRAs offer several advantages [5] [6] over other antenna types like

- DRAs offer no ohmic losses as there is no metal used
- DRAs have smaller size because of the use of higher permittivity material
- DRAs usually have larger bandwidth as it is a 3D structure with a volume

- DRAs can be used in special applications where they will perform better over patch antennas due to either the material properties like transparency or shape like tilted (as done in this thesis)

There are a few disadvantages of DRAs as well when compared with other commonly used antenna types, especially the mass produced microstrip patch antennas. The disadvantages include

- Manufacturing of DRAs is more complex since they have to be machined from (mostly) hard ceramics and thus the fabrication costs are higher
- The DRAs are 3D structures prepared separately which then needs to be glued or placed with in the rest of the circuitry. This makes it more complex and prone to fabrication errors.

The radiation mechanism of a DRA is actually the displacement or polarization currents which are associated with the excited mode [7]. When properly excited modes exist in the DRA, the back and fourth polarization currents give rise fields which escapes the DRA boundaries and radiate into the air. The dimensions of the dielectric resonator is proportional to $\lambda_o/\sqrt{\epsilon_r}$, where λ_o is the free-space wavelength at the resonant frequency and ϵ_r is the dielectric constant of the material.

The graphs in Fig. 2.1 represents good information about the bandwidth (left) and radiation efficiencies (right), related to the dielectric material properties of the DRA: ϵ_r and $\tan\delta$ [8].

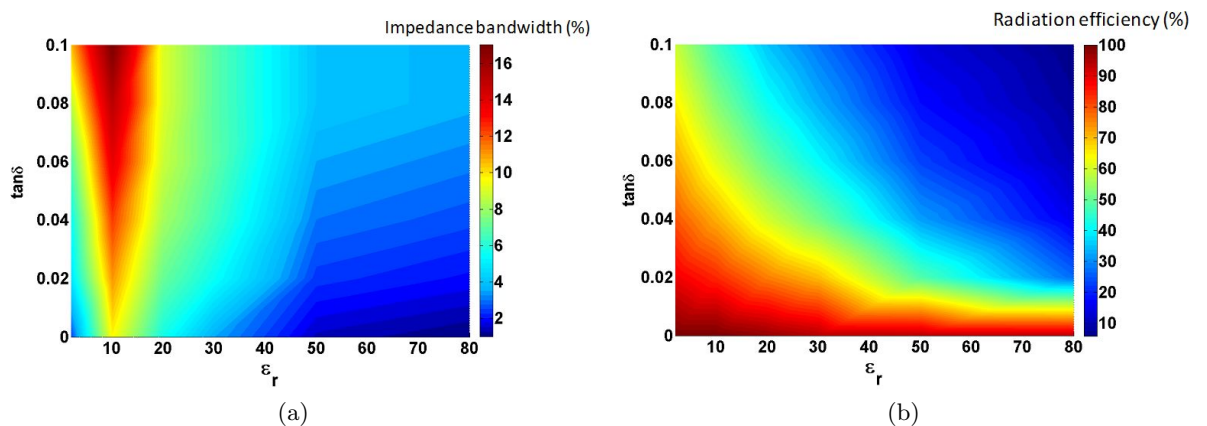


FIGURE 2.1: Relationship of a cylindrical DRA with ϵ_r and $\tan\delta$ with bandwidth (left) and radiation efficiency (right) taken from [8].

Fig. 2.1a shows that no matter what losses are, the bandwidth is maximum at $\epsilon_r = 10$. As for all resonators, if losses increase the impedance bandwidth increase too

and bandwidth decreases when higher permittivity material is used. Therefore, very high permittivity material can only be used in narrow-band applications. Fig. 2.1b for radiation efficiency signifies the well known fact, that the losses of the material incurs more degradation when the permittivity is higher. In other words, when a higher permittivity material i.e. 80 is used, it should be of lower losses. It is due to the fact that the higher permittivity material stores more energy in the DRA, and hence, effects the radiation efficiency more.

As for all resonators, the bandwidth is related to the quality factor of the DRA being used. By definition, of the quality factor is a ratio of the maximum energy stored in dielectric resonator to the energy radiated power from resonator. Further, the radiation Q factor of the antenna can be determined by using the following equation [6]:

$$Q = \frac{2\omega W_e}{P_{rad}} \quad (2.1)$$

where W_e , P_{rad} , ω are stored energy, radiated power and angular frequency respectively. Three kinds of losses have effect on the Q factor, which are:

- dielectric loss ($\tan\delta_d$),
- ohmic loss ($\tan\delta_c$),
- radiation loss ($\tan\delta_\lambda$).

The Q factor is inversely proportional to the sum of all these losses. Thus, Q factor is given by:

$$Q^{-1} = \tan\delta_d + \tan\delta_c + \tan\delta_\lambda. \quad (2.2)$$

Under fixed conditions, ohmic and radiation losses can be ignored. The most dominant loss according to this study is dielectric loss ($\tan\delta_d$). The Q factor is then approximately given by

$$Q^{-1} \approx \tan\delta_d. \quad (2.3)$$

With the known Q-factor, the impedance bandwidth (BW) is related to the Q-factor through the equation given as [6]:

$$BW = \frac{S - 1}{Q\sqrt{S}}, \quad (2.4)$$

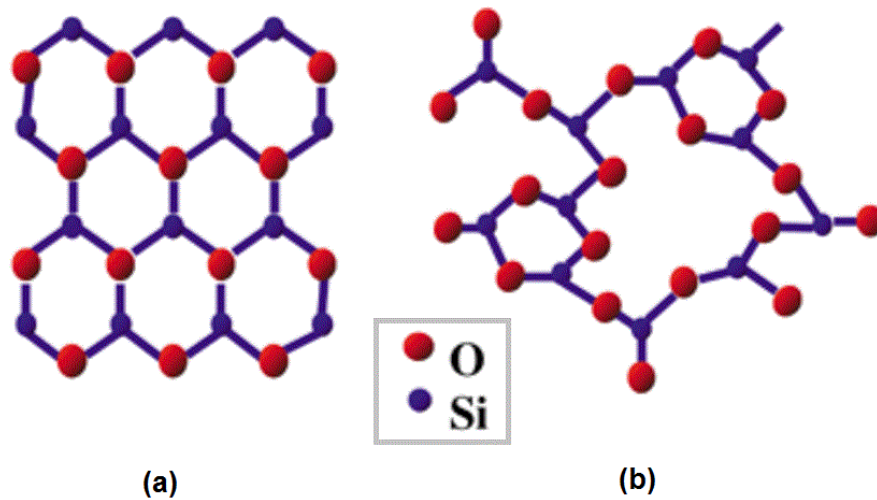


FIGURE 2.2: (a) Ordered or crystalline state (ceramic) (b) unordered or amorphous state (glassy) [11]

where S is the maximum acceptable voltage standing wave ratio (VSWR), which is the ratio of the reflected power back to the source. Equation 2.4 is used to generate graphs, which plot Q-factor as a function of the DRA dimensions, where the DRAs might have different shapes such as cylindrical, rectangular or hemispherical. One uses these graphs, depending on the desired shape and mode, in order to calculate the dimensions of the DRA. A very useful case study of computer aided analysis and design for different shapes and modes of DRAs method is presented by Alexandre Perron and his research group work in 2010 [9].

2.2 Glass, ceramics and glass-ceramics

Glass and ceramics are commonly daily use material. There is a structural difference between glass and ceramics. A glass is fundamentally a disordered structure, as opposed to ceramic, which has an ordered pattern at the atomic level. Fig 2.2 shows an example of a glass and ceramic atomic arrangement structure. While the knowledge of glass and ceramics goes back to thousands of years, glass-ceramics were accidentally developed only recently in the 1950s. By definition, glass-ceramics are polycrystalline materials of fine micro structure that are produced by the controlled crystallization process, which is known as devitrification of a glass [10].

TABLE 2.1: List of currently utilized ceramic materials with zero τ_f [12]

Material Abbreviation	ε_r	$Q \times f_0$ [GHz]
BMT	24	250 000
BZT	29	150 000
BCZN	34	90 000
STLA	39	60 000
CTNA	45	48 000
ZTZN	44	48 000
BNT	80	10 000

Why glass-ceramics?

There are already a number of commercially available microwave dielectric material in the market. Table 2.1 lists some of the ceramics with zero τ_f (no change of resonance frequency with temperature).

Despite the adequate properties of the available microwave ceramics, it has been difficult to overcome all the limitations. Some of the limitations complicate and hinder further cost reduction of the manufacturing process of the material.

One of the limitations is the relatively high porosity ($> 3\%$) [13]. This is of importance for two reasons. One is when metalization is applied to the sintered-ceramics, during which metal salts can enter into pores, thereby deteriorating the dielectric loss of the ceramic material. Secondly, even without any metalization, process absorption of moisture due to the pores would increase the losses. Another limitation is the high compaction during ceramization (10 – 20 %) process. Such high compactions are too much for the dimensional tolerances of the dielectric core in the casting process. Relatively high shrinkage and poor reproducibility of dielectric ceramics leads to additional machining, which introduces more costs.

Finally, sintered ceramics have the problem of a large batch to batch variation in the dielectric properties ($\Delta\varepsilon_r/\varepsilon_r > 1\%$). The main reason of the utilization of such materials is the lack of alternative materials and manufacturing technologies. Unlike conventional ceramics, the glass-ceramics as alternative materials allow overcoming the stated limitations. The advantages of glass-ceramics include [13]:

- The glassy phase allows for a number of hot forming processes known to glass, like casting or precise pressing.
- The melt of well-tuned glass batch gives excellent homogeneity which is characterized by the small variation of the refractive index in typical optical glass. Optical

glasses can for example be reproducibly made with a refractive index variation of 30 cm diameter lens blanks, which is smaller than 10^{-4} .

- The compaction during ceramization of a glass ceramic is with typically $< 1\%$ much smaller than the shrinkage of ceramic during sintering ($> 10\%$) and thus allows for highly accurate geometries.
- Glass-ceramics obtained via a well refined glass phase, which is free of bubbles, are pore-free materials, which can reduce the overall microwave losses. Apart from microwave applications, pore-free structure would have aided advantage in high voltage or electric field applications, where high breakdown voltage is needed.
- Glass-ceramics have relatively less complicated processing than sintered ceramics.

Glass-ceramic have been used extensively in biomedical applications (bio-active or dental), domestic (kitchenware, window glass, floor tiles), optical applications (telescope, infrared mirrors, light filters, glass soldering, wavelength up convertors), electronics (isolators, solid electrolytes, capacitors) and military (bullet and blast proof visors) [14] [15]. Glass-ceramics were first hinted to be used for microwaves (antenna) applications only as recently as 2008 [16]

Preparation of glass-ceramics

Glass-ceramics are mostly produced in two steps: First, a glass is formed by a glass-manufacturing process. The glass is cooled down and is then reheated in a second step. In this heat treatment, the glass partly crystallizes. In most cases, nucleation agents are added to the base composition of the glass-ceramic. These nucleation agents aid and control the crystallization process.

Material formulation main idea

The development of glass-ceramic undertaken in the Deutsche Forschung Gemeinschaft (DFG) project GLACER had a few basic principles of investigation, which are listed below. For detailed overview the reader is referred to [17].

The main idea for developing new bulk-glass ceramics suitable for microwaves was hugely dependent on the base system. The requirements/restrictions for the base systems were

- The melting process of compositions from a targeted system should be carried out at corresponding melting conditions (T_m . $1500 - 1600^\circ C$).

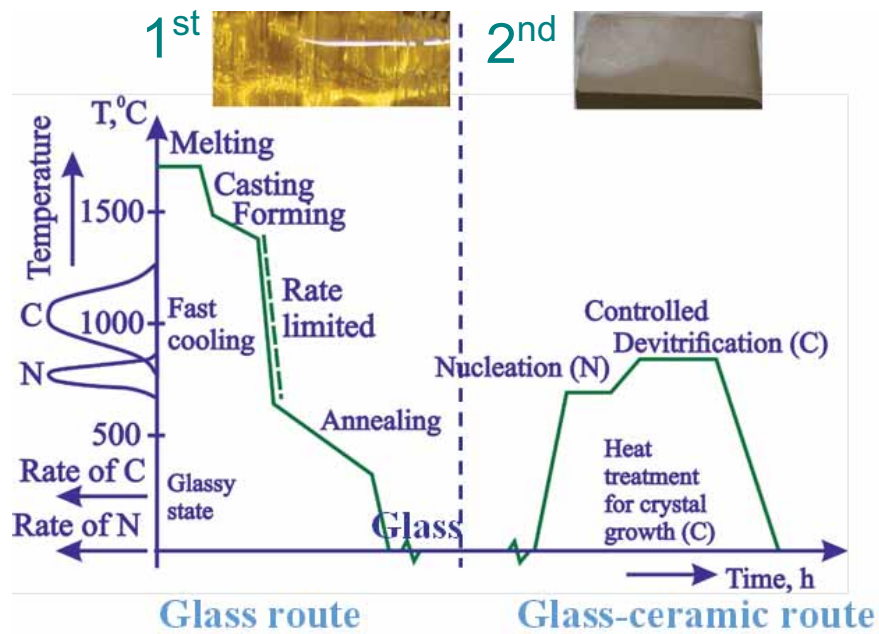


FIGURE 2.3: Glass-ceramic preparation

- The targeted compositions should provide the formation of homogeneous glassy melts at corresponding melting conditions.
- The revealed homogeneous glassy melts should have resistance to crystallization during cooling providing bulk-glassy materials.
- During additional heat treatment the revealed bulk-glasses should provide uniform and fine grain crystallization under formation of pore free ceramic pucks.
- The revealed pore free ceramic puck should contain a maximum amount of targeted phase(s) and the lowest amount of minor phase(s).

2.3 Microwave characterization of bulk-glass ceramics

The first step after obtaining the bulk-glass ceramic material is to characterize it at microwave frequencies. Three of the most important properties associated with any dielectric material for microwave applications are the relative permittivity ϵ_r , dielectric losses $\tan\delta$ and temperature coefficient of resonant frequency τ_f . These three parameters values will determine whether the bulk-glass ceramic material is suitable or unsuitable for a given application.

Hakki-Coleman measurement setup

The characterization of the prepared glass-ceramic was carried out with Hakki-Coleman method [18]. It is a resonance technique for measuring the complex permittivity. The dielectric sample itself supports the resonance. The accuracy of permittivity value measured with this method as given in [19] is 0.2. The main inaccuracy is in the determination of the dimensions of the sample. This can be safely assumed to be in the range of $\pm 0.1\text{mm}$, for which the error margin will still be under 0.5% [20]. The drawback of this method, as well of any resonance method is that it gives the value at a single frequency, as opposed to broadband methods. The value of permittivity does not change a lot for many materials. Therefore, this value can be considered to be constant for at least the microwave regime of frequencies.

The measurement setup is shown in Fig. 2.4. The cylindrical samples is placed between parallel metallic plates. The plates should be large enough, so that the radiation losses are minimized. The plates must be made from highly conductive metals, e.g. copper, to keep the metallic losses low.

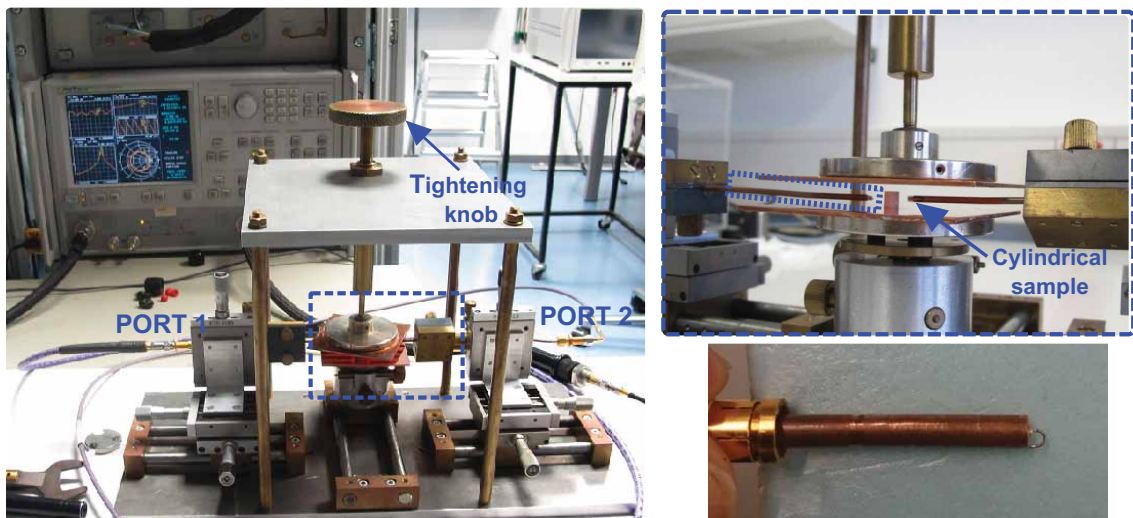


FIGURE 2.4: Experimental structure of the Hakki-Coleman setup.

A typical measurement obtained from the Hakki-Colmann method is shown in Fig. 2.5a. The first four peaks and their corresponding mode numbers are indicated on the graph.

Identification of the TE_{011} mode is aided by the fact that the circular-electric modes have longitudinal current on the parallel plates. Therefore, a slight separation of the plates does not disturb this mode, while all other modes are severely de-tuned [21]. This effect can be seen in Fig. 2.5b, where the small air gap effect on the measurement curve is compared with that of a normal measurement with no air gap.

For measurement of the ϵ_r , the following equation is used [22]

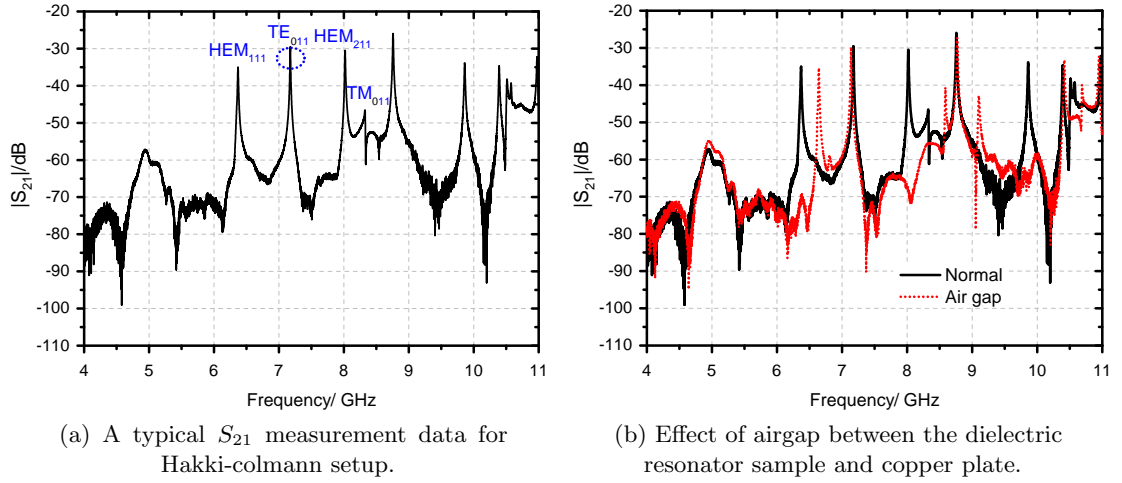


FIGURE 2.5: Hakki-coleman measurement.

$$\varepsilon_r = 1 + \left(\frac{c}{\pi D f_1}\right)^2 (\nu_1^2 + \nu_1'^2) \quad (2.5)$$

$$\nu^2 = \left(\frac{\pi D}{\lambda_0}\right) \left[\left(\frac{\lambda_0}{\lambda_g}\right)^2 - 1\right], \quad (2.6)$$

where $\lambda_0 = \frac{c}{f_0}$, $\lambda_g = 2L$.

λ_g is the guided wavelength and λ_0 is resonant wavelength in air and c is the speed of light in vacuum. The quantity ν_1^2 and $\nu_1'^2$ are related by the transcendental equation

$$\nu \frac{J_0(u)}{J_1(u)} = -\nu \frac{K_0(\nu)}{K_1(\nu)}, \quad (2.7)$$

here $J_0(u)$ and $J_1(u)$ are Bessel functions of first kind and $K_0(\nu)$ and $K_1(\nu)$ are the modified Bessel function of the second kind.

For measurement of the losses of the dielectric sample in the Hakki-Coleman method, it should be noted that this method is not valid for very low loss materials, e.g. for values less than in the order of 10^{-4} . This is because the parallel plates are touching the sample and this effects the accuracy of the measurements. Moreover, the losses due to radiation are neglected in this method. Therefore, a better method would be where instead of two parallel plates a close cavity is used since no radiation occurs. Nevertheless, to measure the loss of the material unloaded Q_u measurement is used in the following equations [23].

$$\tan\delta = \frac{A}{Q_u} - BR_s, \quad (2.8)$$

where R_s is the surface resistivity. In order to measure the quantity Q_u , the coupling from the loops is kept very low. Practically, a value of S_{21} of -30 dB is deemed low enough. The quantities A and B are given by

$$A = 1 + \frac{W}{\varepsilon_r} \quad (2.9)$$

$$B = \left(\frac{l\lambda}{2L}\right)^3 \frac{1+W}{30\pi\varepsilon_r l} \quad (2.10)$$

$$W = \frac{J_1^2(u_1)}{K_1^2(v_1)} \cdot \frac{K_0(v_1)K_2(v_1) - K_1^2(v_1)}{J_1^2(u_1) - J_0(u_1)J_2(u_1)} \quad (2.11)$$

The quantity W is actually the ratio of the energy stored out the sample to the energy stored inside the sample.

In actual practice, a MATLAB program was written which incorporated all the equations, and iteratively calculated the ε_r and $\tan\delta$. The inputs needed were the resonance frequency, the bandwidth of the TE_{011} peak, the height and the diameter of the sample.

Perturbation cavity method for τ_f measurement

The thermal stability of the dielectric resonators is another very important condition that needs to be satisfied when used in practical applications. This is indicated by the quantity τ_f , known as temperature coefficient of resonant frequency. This value must be close to zero, which would mean that the dielectric resonator has no drift in the frequency with the changing temperature. τ_f actually indicates a property of resonator system, while for the dielectric material itself, a more relevant parameter is the temperature coefficient of dielectric constant τ_ϵ . Historically however, τ_f has been used even for describing the material as it is more practical for dielectric resonators [24]. It is measured in part per million per degree Celsius (ppm/ $^\circ C$).

The resonant frequency of the dielectric resonator is related to the physical dimensions and the material properties. Mathematically

$$\tau_f = -\alpha_L - \frac{\tau_\epsilon}{2}, \quad (2.12)$$

where α_L is the linear thermal expansion coefficient of the dielectric material.

The previous section described Hakki-Coleman method which was used for the ϵ_r and $\tan\delta$, which is an open structure and the precise measurement of the temperature of the cylindrical sample is quit difficult. For the glass-ceramics in this work, a cavity resonator method was used which is shown in Fig. 2.6. The cavity was placed on the hot plate, which was heated to pre-defined values with the help of circulating oil. As the cavity temperature increased, the dielectric resonator sample got heated, which produced a shift in the resonance frequency. The frequency peak was measured with vector network analyzer. The value of τ_f was then calculated using the formula

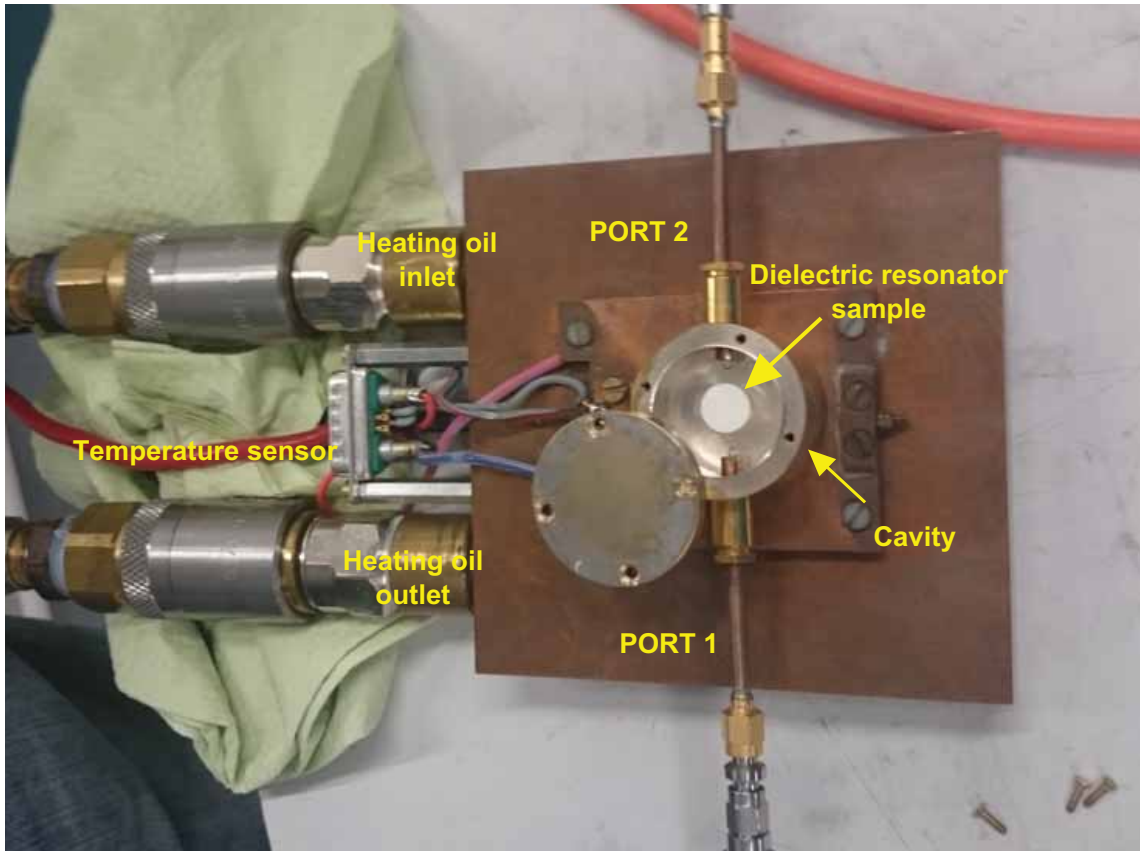


FIGURE 2.6: Experimental setup of the cavity resonator with temperature control structure.

$$\tau_f = \frac{\Delta f}{f \cdot \Delta T} \quad (2.13)$$

A thermal imaging camera was used to read the temperature of the dielectric resonator sample by opening the cavity immediately after reading out the frequency peak. It should be noted that the resonance cavity is also expanding with the temperature. This expansion however is very small and can be neglected. For more accurate measurements cavities with very low thermal expansion, e.g. ceramic cavities with metal films are used.

2.4 Homogeneity test of bulk-glass ceramic

As it was stated that homogeneity of the bulk-glass ceramics is an intrinsic advantage, this was put to test by checking the homogeneity of the ceramized block of size $150 \times 60 \times 20$ mm. The samples for measurements, were chosen to be cut from section such that many areas of the block is covered, e.g. upper side, lower side and front and back as shown in Fig. 2.7. The measurements showed an average value of ϵ_r equal to 33.55, varying between 33.3 to 33.75. The deviation from the mean value is only 0.74%, which shows that the ceramized block has a high homogeneity.

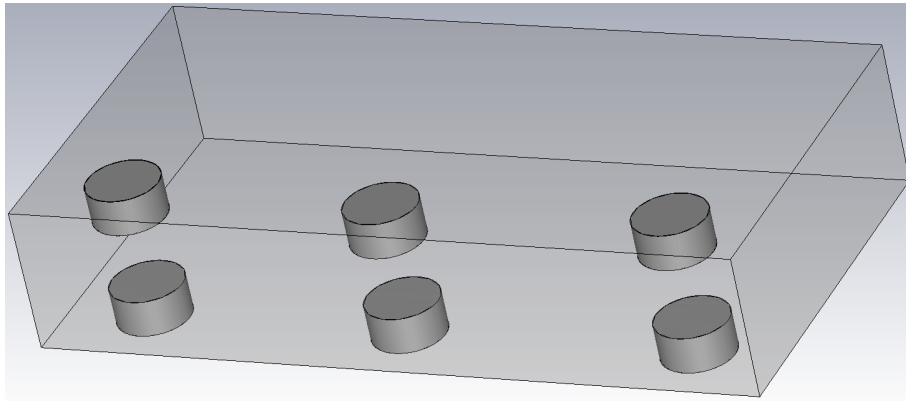


FIGURE 2.7: Location of cylinders cut from the block of glass-ceramic material for homogeneity test.

TABLE 2.2: Homogeneity test for samples cut from different parts of a bulk-glass ceramic block.

Sample	Diameter [mm]	Height [mm]	Frequency [GHz]	Q	Qf [GHz]	ϵ_r	$\tan\delta$
1	9.73	4.95	7.3226	566	4145	33.73	0.0017
2	9.71	4.95	7.329	557	4082	33.72	0.0017
3	9.72	4.94	7.3418	571	4192	33.66	0.0016
4	9.7	4.95	7.3298	535	3921	33.75	0.0018
5	9.91	4.93	7.2978	595	4342	33.6	0.0016
6	9.88	4.94	7.2898	586	4272	33.67	0.0016
7	9.68	4.94	7.3378	568	4168	33.81	0.0017
8	9.68	4.94	7.3418	560	4111	33.77	0.0017
9	9.88	4.93	7.2827	596	4340	33.82	0.0016
10	9.86	4.94	7.2784	595	4330	33.84	0.0016
11	9.71	4.94	7.3638	590	4344	33.48	0.0016
12	9.72	4.93	7.3618	596	4387	33.55	0.0016
13	9.73	4.91	7.3487	592	4350	33.8	0.0016
14	9.69	4.93	7.3375	582	4270	33.86	0.0016
15	9.69	4.94	7.3619	584	4299	33.56	0.0016
16	9.74	4.94	7.3739	590	4350	33.3	0.0016
17	9.74	4.91	7.3500	578	4248	33.76	0.0016
18	9.71	4.93	7.3499	576	4233	33.69	0.0016
19	9.76	4.94	7.3300	577	4229	33.65	0.0016
20	9.75	4.93	7.3307	579	4244	33.75	0.0016
Average						33.55	0.00165
Minimum						33.3	0.0016
Maximum						33.75	0.0018

2.5 Chemical etching of non-ceramized glass

Apart from casting, machining or micro-machining glass or glass-ceramic samples, there is another possible way to manipulate or structure glass structure. Glass is long known to be solvable in concentrated hydrofluoric acid (HF). The wet etching method for patterning glass with concentrated HF solution is not new. It has already been put to use by many researchers. For example, in [25] wet etching was used to obtain glass vias by wet etching for IC packaging applications. In [26] more than $600\mu\text{m}$ of etching was achieved using HF resistant photo-resist mask. In [27] a 1 mm etching of glass has been achieved. In the context of glass-ceramics for antenna or dielectric filters, the wet etching can be used as an alternative way of manufacturing precise dimensions. For higher frequencies, e.g. at 60 GHz, the required dimensions of a rectangular or cylindrical shape would be close to 1 mm. Thus, if etching of glass or glass-ceramic up to 0.5 mm can be achieved, then it will mean that dielectric resonators with one dimension around 1 mm could be produced with wet etching process.

Some tests were performed on the non-ceramized glass compositions. Although the results obtained were not yet such that they could be put to practical use, but the preliminary results shown here could act as a seed for further research into this topic. For the mask layer, a *Cr/Au* of 30/80 nm was first evaporated on the samples. Simple lines with gaps were used. The samples were then immersed in concentrated (50%) HF acid. Some glasses such as pyrex showed not much solvable in the acid. One glass composition with internal sample number *DEH43916* however showed etching of $176\mu\text{m}$ after one hour as shown in Fig. 2.8. This result for the first run is encouraging. The sample surface became quite defective after leaving it for 6 hours in the HF acid.

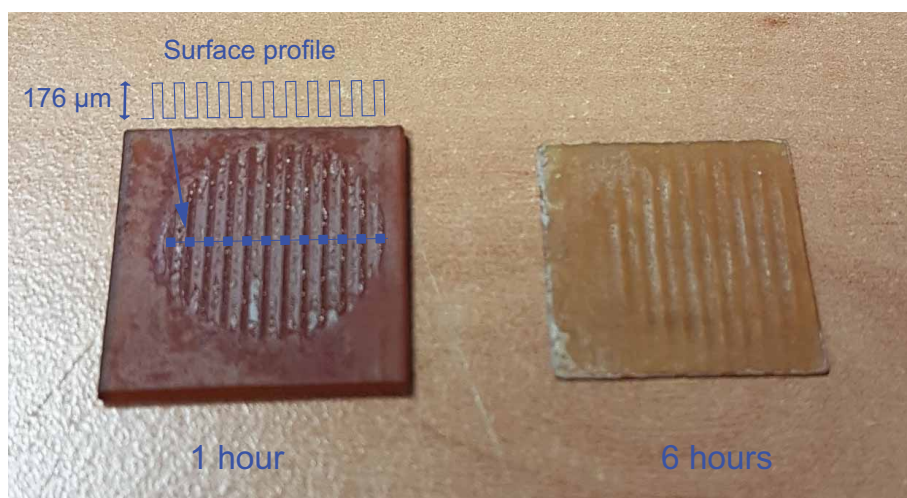


FIGURE 2.8: Wet etching of glass with HF acid.

2.6 Results of promising glass-ceramic materials

After extensive number of melts and their measurements some promising glass-ceramic materials were obtained. The values of ϵ_r from 17 to 36 with Qf values of 1900 to 10,000 were obtained. Many compositions showed $|\tau_f|$ values of < 50 ppm/K which is promising. The most promising materials as measured during this study are listed in table 2.3. The list contains materials measured within the DFG project GLACER along with the materials formulated in [20] which were also measured by the author.

TABLE 2.3: Promising glass-ceramic material obtained during the study.

Sample	ϵ_r	$\tan\delta$	Qf [GHz]	τ_f [ppm/K]	Comments
42014DEH373	21.4	1.1×10^{-3}	9500	-1	
42014DEH354	22.5	1.1×10^{-3}	9590	18	
42014DEH347	30.1	1.3×10^{-3}	6860	169	
42732DEH357	23.0	1.6×10^{-3}	6380	23	
42732DEH352	33.7	1.4×10^{-3}	6140	> 170	
42452-1450DEH325	26.9	5.7×10^{-3}	1630	80	
42452-1600DEH328	21.5	1.1×10^{-3}	9710	16	
Schott GH Glass-1	19.8	4.8×10^{-3}	1832	-36	Transparent
Schott GH GC-1	25.29	3.4×10^{-3}	2349		
Schott GH GC-2	22.08	4.7×10^{-3}	2048		
Schott GH GC-3	25.6	4.3×10^{-3}	1835	40	
Schott GH GC-4	25.8	3.8×10^{-3}	2085		
Schott GH GC-5	27.75	2.1×10^{-3}	3363		
Schott GH GC-6	28.15	3.8×10^{-3}	2064		
Schott GH GC-7	31.5	1.1×10^{-3}	5874	25.2	
Schott GH GC-8	31.4	1.1×10^{-3}	6242	33.9	
Schott GH GC-9	32	1.8×10^{-3}	3824	20.5	
Schott GH GC-10	32.05	1.3×10^{-3}	5085	53.6	
Schott GH GC-11	32.4	1.1×10^{-3}	5895	6.3	
Schott GH GC-12	32.65	6.5×10^{-4}	9579	19.14	
Schott GH GC-13	32.98	7.6×10^{-4}	8377		
Schott GH GC-14	33.1	6.4×10^{-4}	9712		
SCHOTT GHz 33	33.7	1.5×10^{-3}	4736	61	Datasheet attached

Chapter 3

Dielectric Resonator Antenna (DRA) Elements

3.1 Dielectric resonator antennas based on glass-ceramics

The dielectric material listed in the previous chapter was practically put to use in the fabrication of dielectrically loaded antennas (DLA) or dielectric resonator antennas (DRA). These will be explained below.

3.1.1 Glass-ceramic based patch antennas

Patch antennas are probably the most used antenna type due to their ease of fabrication, low profile and moderate gains. A patch antenna is essentially a resonant conductor of a certain length. The length is equal to the $\lambda_g/2$, where subscript 'g' identifies the guided wavelength. The guided wavelength is dependent on the substrate used, and hence, a size reduction is possible when high permittivity substrates are used. This is why dielectric loading of patch antennas has been commonly used for size reduction, e.g. for GPS patch antennas. Glass-ceramic has been used in this work to manufacture such dielectric loaded patch antennas.

The significance of the fact that glass provides a more homogenous material becomes very important for such antennas. Dielectric loading along with reducing the size of antenna, comes with a price in the form of reduction in the bandwidth. As the dielectric permittivity increase, the narrowing bandwidth of a patch antenna becomes a limiting factor. The narrow bandwidth limits the freedom of the deviation of the permittivity of the dielectric from a certain acceptable value.

As discussed for glass-ceramics, the homogeneity and low batch to batch variation of bulk-glass ceramics becomes a very significant advantage especially when used for narrow band antennas (or filters). This section will explain the use of glass-ceramics for the first time for patch antennas. The patch antenna is chosen to be GPS L1 band which is defined with center frequency of 1575 MHz and a bandwidth of 20 MHz. The GPS antennas require circular polarization. Many prototypes were built in house from different glass-ceramic batches. Here the antennas fabricated from the final material with a permittivity of 33.7 are presented.

Patch antenna design

To realize the patch antenna many parameters need to be decided. After going through many commonly available GPS patch antennas. A very common size of $20 \times 20 \times 4$ mm was chosen. Since the ground size influences the whole design too, it was chosen to be 90×90 mm. The most common configuration for a GPS patch is a pin mounted module, hence it was chosen for the feed. Another common practice is to cut the corners for generating the circular polarization. This is the most straight forward and easy method, and hence, was adopted for this work too.

The geometry of the GPS patch antenna is shown in Fig. 3.1. A large copper plate was used as the ground plane. The dimensions of the ground plane affect the resonance frequency because of the fringe fields. Although in practice smaller ground planes are used because of the impracticality of large sizes, but for testing and measurements a ground plane size of 90×90 mm was chosen. A smaller ground plane is also prone to more measurement environment influence, therefore, a larger size will be more stable, i.e. simulations and measurements will better agree. This point should be emphasized here, because more than one patch antennas were fabricated to study the homogeneity of the material. Therefore, a measurement which is more independent of the measurement environment influence is important such that the measurements are more close to the real values.

The feed is a coaxial connector which penetrates the ground plane and dielectric material all the way up to the patch. The hole in the ground plane should correspond to the opening on the connector, so that a good matching is achieved. The position of the feed is also a little offset from the center as would be expected for a patch antenna. The optimum position is determined with CST Microwave Studio 3D simulations.

In order to radiate circular polarization for the patch, with one feed, two degenerate modes with 90° out of phase from each other must be generated. For achieving this, the simplest method is to cut the two corners. This truncation length of the corners

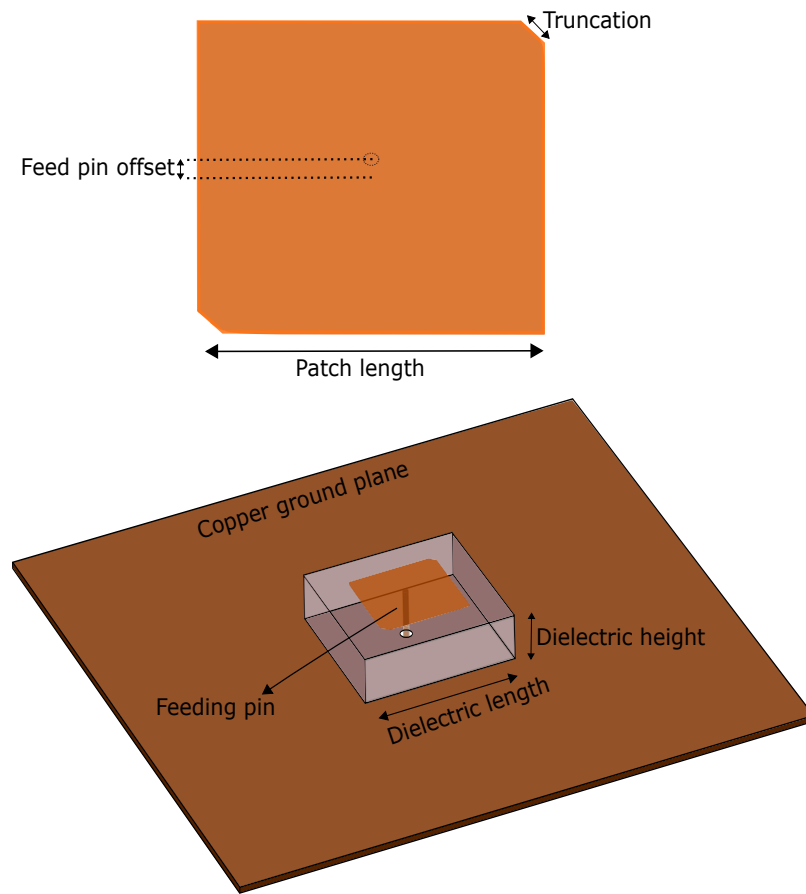


FIGURE 3.1: Dielectric loaded patch antenna design.

is determined by simulations, i.e. by optimizing the axial-ratio of the far field pattern. The axial ratio is actually the ratio of the two polarizations, i.e. vertical and horizontal of the E-field. An axial ratio of less than 3 dB is the accepted criteria for a circular polarization.

Simulations of the patch antenna

Since the dielectric used is relatively high compared to patch antennas made on usual substrate material such as Rexolite or Alumina, more accurate simulations are needed for the proper design of the patch antenna. The sensitivity of change in any dimensions is higher when a high permittivity material is used.

As was discussed in the previous chapter, the glass-ceramic material has a homogeneity which is far better than that which can be achieved with conventional ceramic materials. But never the less, there is some variation in the ϵ_r from ceramized batch to batch or even with the position of the material cut from the ceramized piece. Though it is very

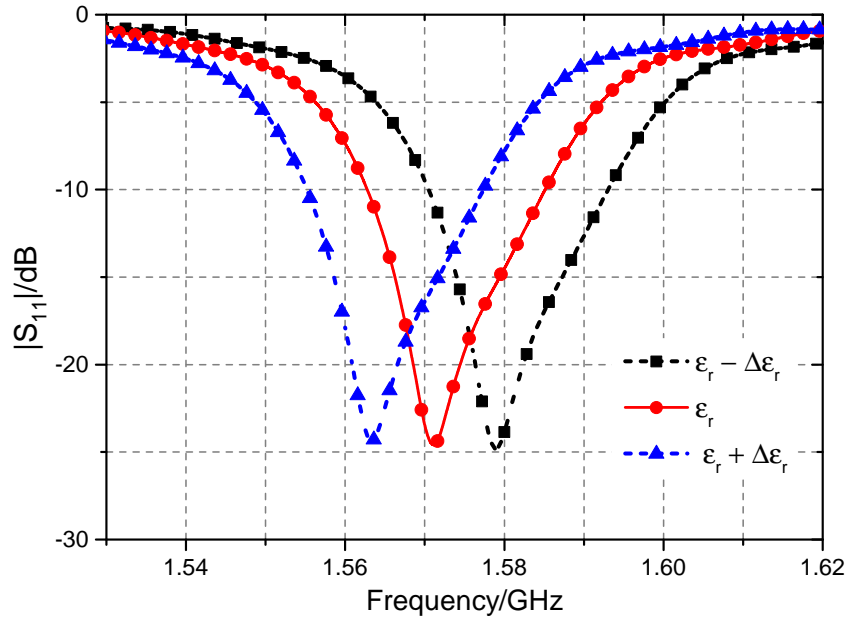


FIGURE 3.2: Shift of center frequency with $\pm 1\%$ variation in the permittivity value around $\epsilon_r = 33.7$.

small and is not expected to exceed 0.5% , but will still be important because of the low bandwidth of operation. Also the measurement error as discussed in chapter 2 is also present, which is expected to be close to $\pm 0.5\%$. To show the effect of the variation in the ϵ_r of the material, a simulation was performed by assuming 1% variation. At 33.7 this is equal to 0.337 . This value was added and subtracted from 33.7 which is assumed to be the true value of the ϵ_r of the material.

The simulations of 1% variation of ϵ_r is shown in Fig. 3.2. The simulations shows a shift of around 7.5 MHz in the center frequency of the antenna. At first, it might not seem significant, but as maximum bandwidth of the GPS band is itself only 20 MHz, this shift of frequency becomes very significant. The shift of the center frequency is not only significant for the matching but also for the polarization performance. This is shown in Fig. 3.3, where the axial ratio of the antenna is plotted at the targeted frequency of 1575 MHz. The axial ratio which for ideal case should be as low as possible or at least under 3 dB, can be as worse as 10 dB with just 1% variation in the value of ϵ_r of the high dielectric material. Therefore, even if the matching is not a problem, maintaining the circular polarization at the desired frequency will be a challenge if the permittivity varies.

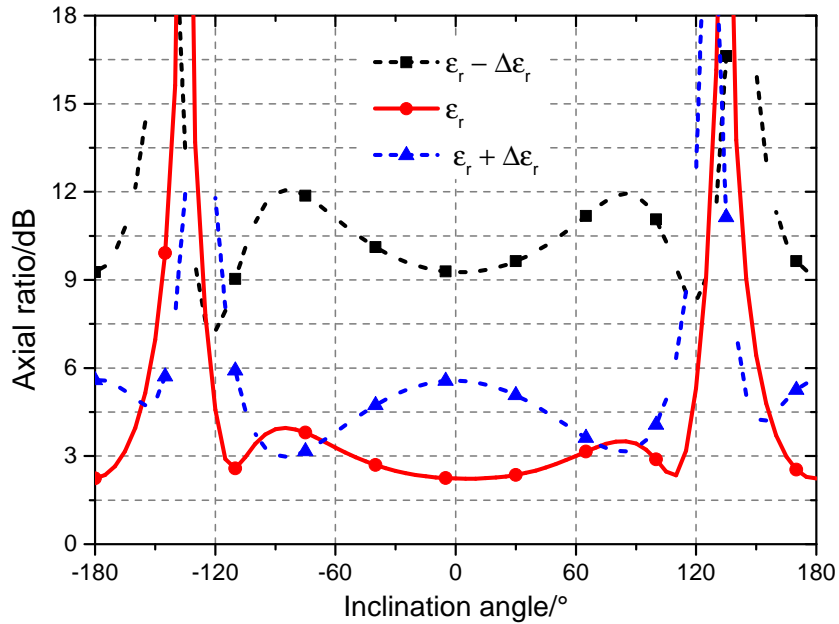


FIGURE 3.3: Variation of the axial ratio of the patch antenna as function of cut plane ϕ (Inclination angle, E-plane) with $\pm 1\%$ variation in the permittivity value.

Post-fabrication adjustment mechanism

As was seen in the previous section, even a little variation in the permittivity, a narrow-band antenna can be completely offset from the desired frequency band. Not only the permittivity of the loaded dielectric substrate but also the ground plan size or any disturbance in the vicinity of the patch will also have the undesired effect of de-tuning the patch resonance. Therefore, it will be beneficial to incorporate a simple post-fabrication tuning mechanism in the patch, to tune the frequency in both, decreasing or increasing direction. This would make sure that no matter if the actual value of the permittivity value is more or less than the assumed (or measured) value, the patch can be tuned to the desired frequency band.

Two simple and intuitive mechanisms are combined to incorporate the post-production retuning capability in the patch antenna. The first is a coupling strip. Such coupling strips have been used to increase the bandwidth of antennas or reduce the physical size (increase the electrical size). The second mechanism is to introduce slots in the patch, which is also effectively increasing the electrical size of the patch.

Fig. 3.4 shows a patch with coupling strips. Two such strips are added to keep the circular polarization of the patch intact. The coupling strips can be thought of as an extension of the patch and hence the electrical size of the patch increase. This results in lowering of the patch resonance frequency. The lowering of the resonance frequency is proportional to the length of the strip and the gap between the coupling strip and patch.

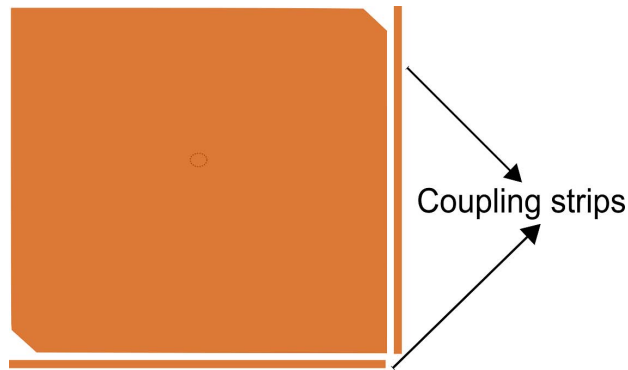


FIGURE 3.4: Patch design with coupling strips.

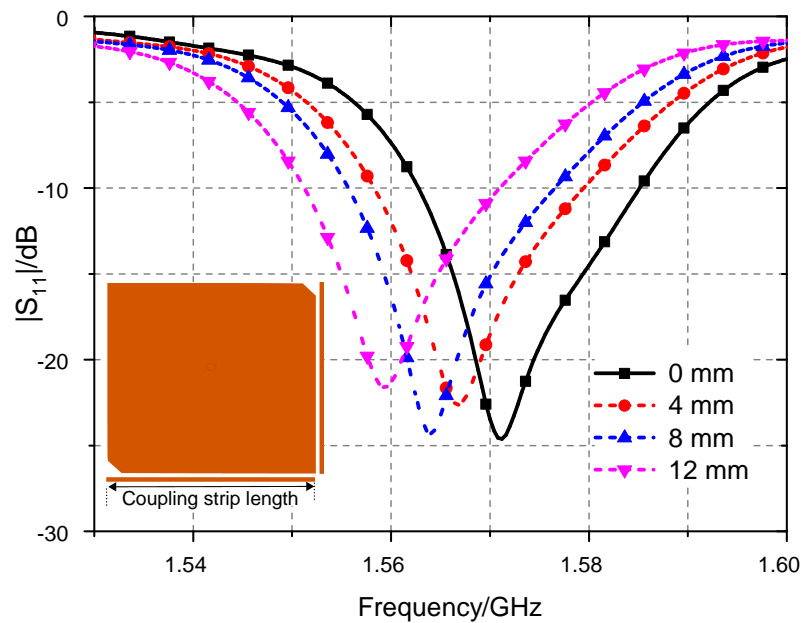


FIGURE 3.5: Variation of the resonance frequency of the patch antenna with variation in the length of the coupling strip.

The simulations of different coupling strip lengths is shown in Fig. 3.5. The gap of the coupling strip also determines the amount of shift of the frequency. The gap when closer, off course, means a more effective strip. Since this strip is intended to be easy to cut according to the post-production result of the measurement, the gap should be kept such that it can be cut without damaging the patch metal. Similarly the width of the patch is another parameter to consider, it was chosen to be 0.2 mm as cutting it away would be easier than if it is wider. It should also be noted that the simulations shown in Fig. 3.5 depicts the effect of only one strip on either side of the patch. The effect of the coupling strip will off course be increased when two such strip are used for each polarization, i.e. on all four sides. Such arrangement will increase the variation of ϵ_r , which the coupling strips will be able to compensate.

Similar to the coupling strips, slots in the patch can also be used to incorporate a post-production tuning mechanism into the patch. A slot in the patch makes the path of the current longer, and hence, the electrical length is increased. Two such slots have been introduced in the patch design shown in Fig. 3.6. The resonance frequency shift with the length of the slot is shown in Fig. 3.7. The currents on the patch with a slot and without a slot is shown in ?? for comparison.

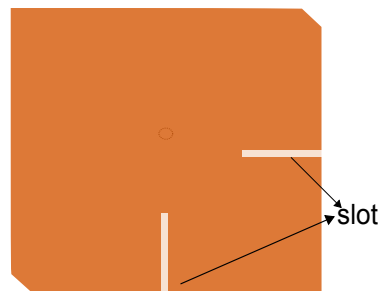


FIGURE 3.6: Patch with two slots.

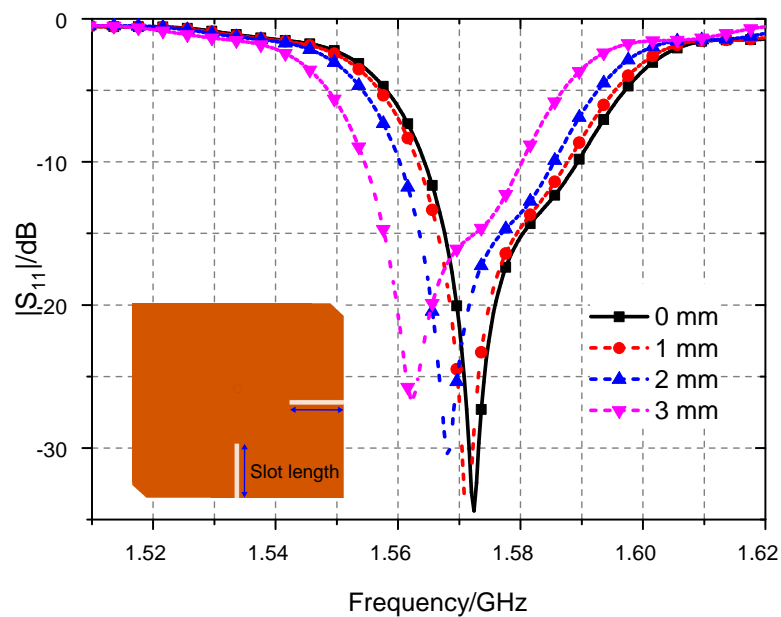


FIGURE 3.7: Variation of the resonance frequency of the patch antenna with variation in the length of the slots.

Since the introduction of the slot into the patch has lowered the resonance frequency of the patch, the frequency will again move to higher end if the slot is shorted. As shown in Fig. 3.8 a shorting strip can be used to provide a shorter path to the currents on the patch, thus reducing the electrical length of patch again, i.e. by passing the effect of the slot. The position where the shorting strip is applied, effectively dictates the length of the slot. Hence, a tuning can be achieved by shorting the slot at different positions.

The effect of applying the shorting strip at different positions is shown in Fig. 3.9. When the strip is applied at the edge of the patch it effectively gets rid of the slot i.e. the

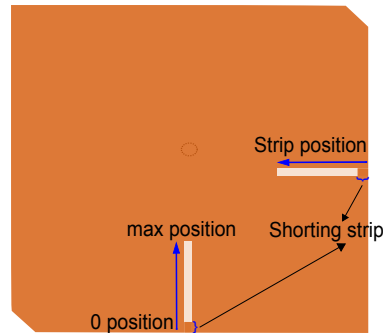


FIGURE 3.8: Shorting strip applied to the slot, effectively diminishing the slot.

length of the slot is 0. The graph shows the movement of the resonance of the patch with different strip positions.

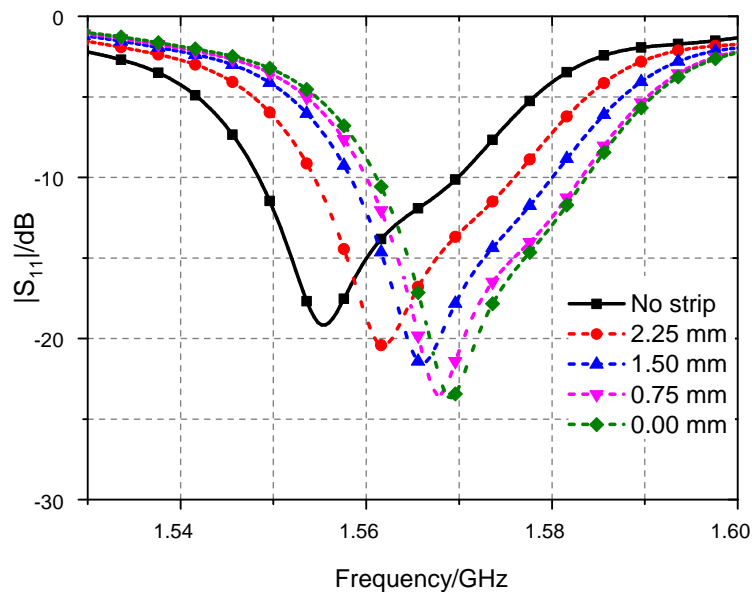


FIGURE 3.9: Variation of the resonance frequency of the patch antenna with position of the shorting strip from the edge of the patch.

After observing how the resonance frequency is affected by coupling strips, slot and the shorting strip in the slot, a mechanism can now be devised where a patch can be fabricated and some post-fabrication tuning both in increasing or decreasing frequency can be achieved. This is summarized in the following step by step:

- The patch is designed including slots of proper length for the intended frequency. The length is chosen according to the variation expected in the real value of the ϵ_r of the substrate.
- The slot is then shorted at the edge of the patch. Thus, effectively removing the slot effect. This will make the patch electrically smaller, and hence, shift the frequency of operation upwards.

- The coupling strips are added. Thus, the frequency can again be lowered, i.e. to be again centered at the intended frequency.

In order, to see how the addition of slot, shorting strips and coupling strips has added a post-tuning functionality to the patch, we consider three cases for the permittivity of the dielectric substrate material of the patch:

- ϵ_r is less than the assumed value: In such a case, the measured matching frequency will be higher than the intended frequency. To lower the resonance frequency, the shorting strip can be applied at appropriate place.
- ϵ_r is greater than the assumed value: In such a case, the measured matching frequency will be lower than the intended frequency. To increase the resonance frequency, a small appropriate portion of the coupling strip can be cut.
- ϵ_r is exactly equal to the assumed value:
 - if the shorting strip is already applied, nothing needs to be done.
 - if the shorting strip was not included in the fabrication, it should be applied post production.

Fabrication of the patch antenna

The glass-ceramic based patch antenna were fabricated in house. The fabrication steps are shown in Fig. 3.10. The square shaped ceramic material is machined first, and a hole is drilled according to the offset distance from the center, which is determined in the simulations. The samples were then put up in the evaporation chamber for processing a chrome/gold layer. A layer of 20/60 Chrome/Gold was evaporated on to the samples. The sample is spin-coated with photo resist. Photo resist 4500 was used with 2000 revolution per minute, which provides a thickness of $4\mu m$. This was deemed enough, since the skin depth at the center frequency 1575 MHz is $1.898\mu m$ for gold. Although as a rule of thumb 5 skin depths are used for minimum losses, but the more height of the metal also meant in accuracy in the dimensions and height profile, therefore, $4\mu m$ was kept. Due to the hole in the sample, the vacuum used for holding the sample on the photo resist spinner is not easy to implement.

After photo resist coating, the photolithographic process is applied. The mask is aligned with respect to the hole of the sample. Then, the photo resist etching step is applied, after which the electroplating is done. Finally, the sample is cleaned of the photo resist

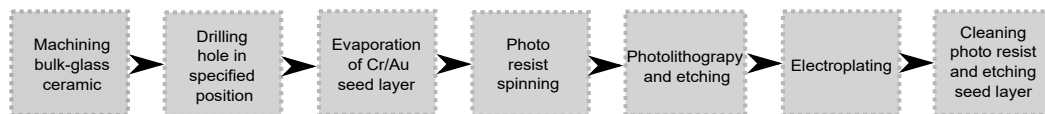


FIGURE 3.10: Processing steps for the bulk-glass ceramic based patch antenna.

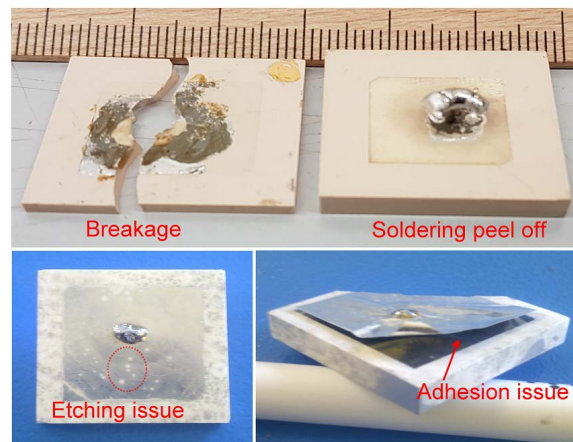


FIGURE 3.11: Issues with fabrication of the patches with bulk-glass ceramic substrates.

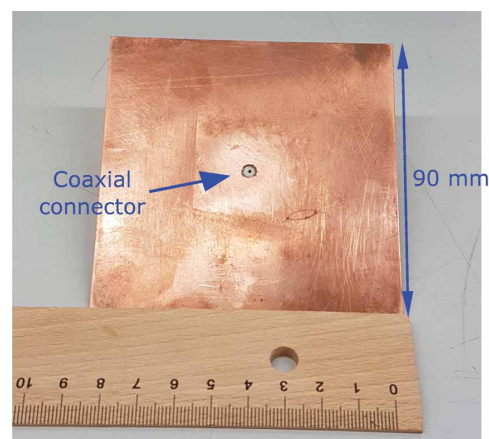


FIGURE 3.12: Copper plate with coaxial connector for testing the patch antennas.

and the seed layer is etch away. Some of the problems that occurred during processing are shown in the Fig. 3.11.

Samples were broken in the photo resist spinning process as they got thrown away because of vacuum ineffectiveness due to the hole. The adhesion of the metal, e.g. silver proved to be problematic. It peeled off easily. This then poses a question of whether the high smoothness of the glass-ceramics is really needed or not. If the highly smooth surface will have less adhesion, then it must be made a little rough for the metalization to stick. Commercially, silver metalization with some form of glue is used through screen printing process, therefore, it has to be seen whether the smoothness of the glass-ceramics is a problem for the process in terms of adhesion of metalization.

In the early and not very stable glass-ceramic compositions sometimes had a non-homogenized appearance, and the surface looked different because of various unwanted phases in the crystallization. This made it sometimes difficult to get a clean etch of the photo resist. Therefore, the metal quality in the end was compromised. Soldering of the pin through the hole to the upper patch metal was yet another step that sometimes created problems. Since the metal was very thin and also the adhesion was not great, the soldering point would some time peel off the metal with it due to the high temperature of soldering process.

The antennas were tested in a fixture. It was a square metal plate with a hole of 4 mm in the center. The dimensions of the plate were 90 mm^2 with a thickness of 0.5 mm. The plate should be as smooth as possible, specially around the hole as the patch antenna would be placed there. Any gap or height difference would mean deviation in the resonance frequency. A 50Ω coaxial female connector is soldered in the center.

Patch antennas with dielectric height of 4 mm

The first set of prototypes were fabricated on a $25 \times 25 \times 4$ mm bulk-glass ceramic substrate. The permittivity as measured with the Hakki-Coleman setup was found to be 33.7 with $\tan\delta$ of 0.001 at around 7 GHz. Three antennas were successfully fabricated. One of the fabricated prototype is shown in Fig. 3.13. The pin which is soldered to the patch through the hole is extended towards the back side. This is connected into the coaxial connector in the middle of the fixture.

The reflection loss measurements of all the three patch antennas fabricated is shown in Fig. 3.14 along with the simulation. All the three antennas show their resonance at slightly higher frequency than the expected, i.e. the permittivity value supposed was a little higher than the actually value. The resonance is centered on average around 1.590 GHz instead of 1.575 GHz. The difference is 15 MHz. After simulating the change in permittivity the value was found to be 0.4 less, i.e. 33.3 instead of 33.7. It should also be noted that the matching is also influenced by the imperfect fabrication, e.g. flatness of the ground plane. The soldering point of the pin to the patch and the imperfection in the geometry of the dielectric would also influence the resonance frequency to some extent. Therefore, keeping all these in mind, the three antennas show very good performance of having closeness in their measurement of the reflection loss data.

The measured resonance frequency for the three fabricated prototypes are given in table 3.1. The deviation from the center target frequency of 1575 MHz is written in the next column of the Table 3.1 along with the actually produced dimensions of the glass-ceramic after machining. As can be seen, the dimensions are very accurate but still not perfect.

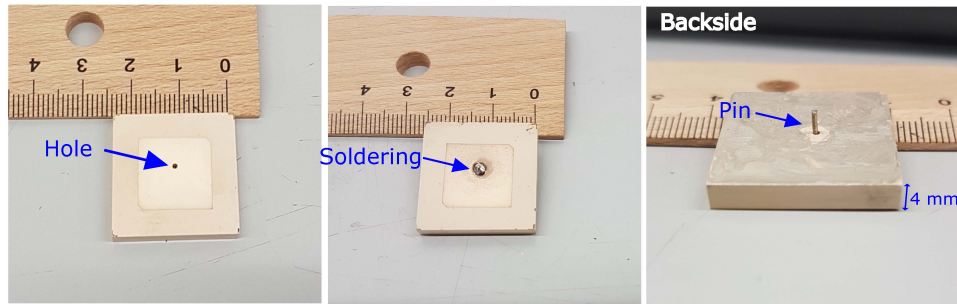


FIGURE 3.13: Fabricated patch antenna with 4 mm thick glass-ceramic dielectric.

TABLE 3.1: Resonance frequency of the 3 prototypes with 4 mm substrate

	Freq [MHz]	Deviation [MHz]	Measured Dimensions [mm]
Patch 1	1590	15	25.07 × 25.09 × 3.97
Patch 2	1582	7	25.07 × 25.04 × 3.97
Patch 3	1600	25	25.06 × 25.08 × 3.96

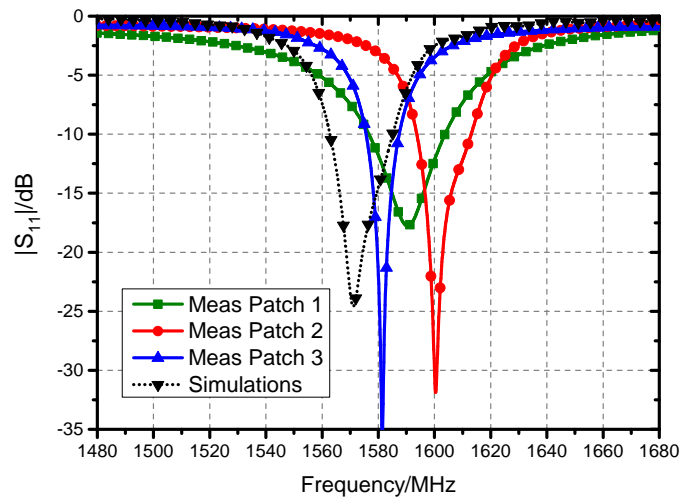


FIGURE 3.14: Reflection loss measurements for the three fabricated patch antennas with 4 mm thick glass-ceramic dielectric.

The height of the substrate which has the most influence on the resonance frequency is seem to be some what smaller. On average, it was 0.03 mm smaller than the actually value of 4 mm. The measured resonance frequency deviation from the target frequency is still in a range which can be categorized as very good for the first proof of concept results of the material. With another iteration of the fabrication the frequency of operation can be made to correspond exactly to the target frequency.

The antennas were then measured in the anechoic chamber. As the patch antenna were circularly polarized, it is necessary to define two planes for the far-field measurements. They are usually designated as right-hand circular polarization (RHCP) or left-hand

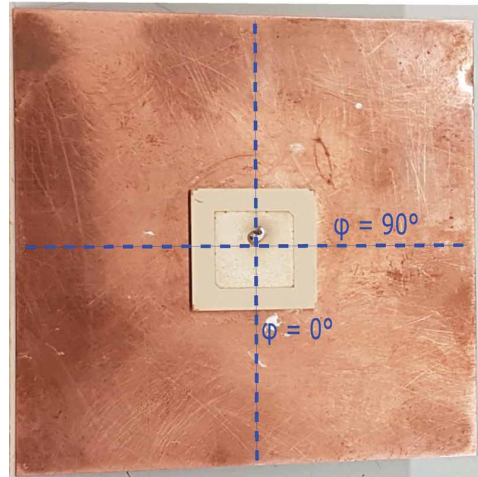


FIGURE 3.15: Two axis defined for the fabricated patch antennas for the far-field measurements.

circular polarization (LHCP). But due to the absence of circularly polarized antennas for the transmitter, the measurements were performed with linearly polarized standard gain horn antenna. Since, a power meter was used (and not a vector network analyzer), there was no measurement for the phase of the signal. Therefore, the sense of polarization could not be determined. Nevertheless, the two planes defined for the far-field measurements are the $\varphi = 0^\circ$ and $\varphi = 90^\circ$ as shown in Fig. 3.15.

The far-field radiation patterns for the three fabricated patch antennas are shown in Fig. 3.16, 3.17, 3.18. All the antennas showed cross-polarization levels of at least less than 8 dB. Practically for circular polarization the cross polarization, levels are below 3 dB. To explain the inadequate cross-polar measurements, it should be noted that there was some mismatch in the reflection loss measurements, i.e there was a mismatch between simulations and measurements in terms of frequency. As would be expected for such a narrow band antenna, a little discrepancy will result in worse behavior in the polarization levels. This is what is seen for all the three antenna prototypes.

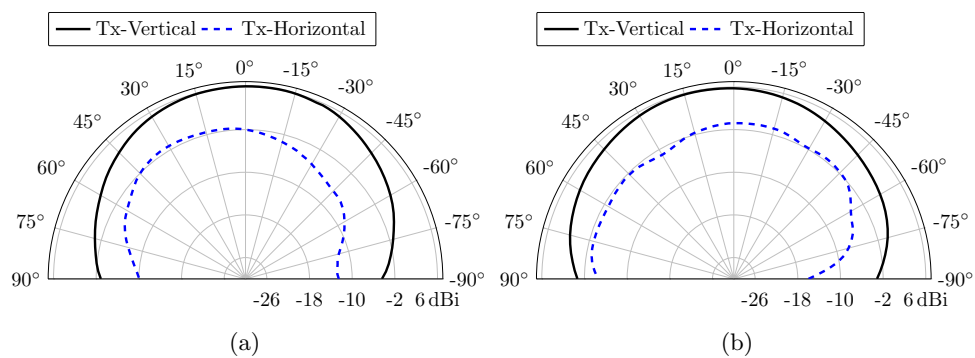


FIGURE 3.16: Far-field measurements in two planes of the fabricated prototype 1 at 1590 MHz (a) $\varphi = 90^\circ$ (b) $\varphi = 0^\circ$.

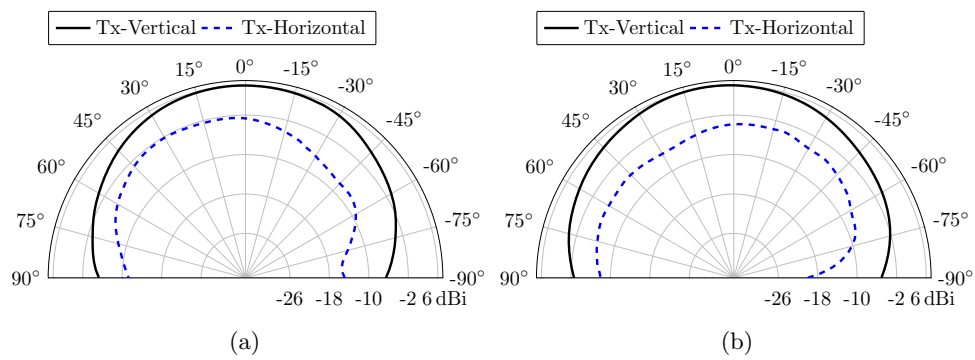


FIGURE 3.17: Far-field measurements in two planes of the fabricated prototype 2 at 1582 MHz (a) $\varphi = 90^\circ$ (b) $\varphi = 0^\circ$.

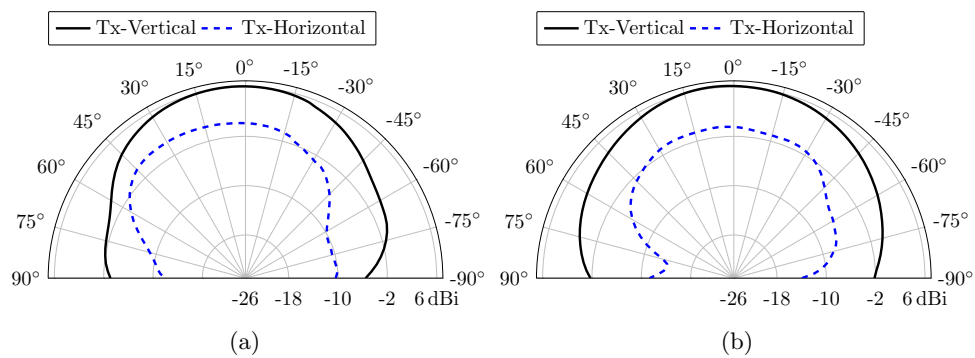


FIGURE 3.18: Far-field measurements in two planes of the fabricated prototype 3 at 1600 MHz (a) $\varphi = 90^\circ$ (b) $\varphi = 0^\circ$.

Patch antenna with dielectric height of 2 mm

Another set of patch antennas with a dielectric of $25 \times 25 \times 4$ mm were fabricated. A thinner dielectric because of the lower profile makes it a common choice in the market. There were 2 antennas which were successfully fabricated. A sample of the antenna is shown in Fig. 3.19.

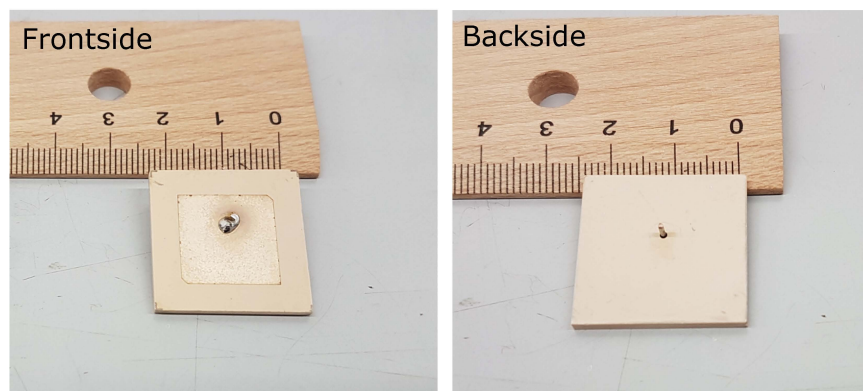


FIGURE 3.19: Fabricated patch antenna with 2 mm thick glass-ceramic dielectric.

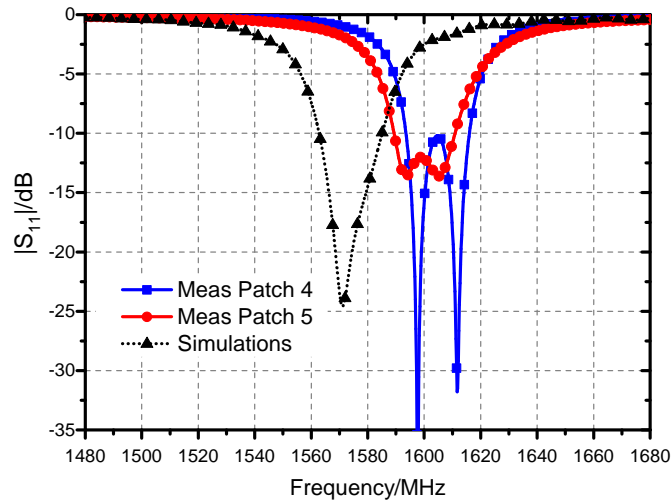


FIGURE 3.20: Reflection loss measurements for the two fabricated patch antennas with 2 mm thick glass-ceramic dielectric.

TABLE 3.2: Resonance frequency of the two prototypes with 2 mm substrate

	Freq [MHz]	Deviation [MHz]	Measured Dimensions [mm]
Patch 4	1605	30	25.10 × 25.08 × 1.96
Patch 5	1596	21	25.05 × 25.04 × 1.94

The reflection loss measurements of the two patch antennas fabricated is shown in Fig. 3.20 along with the simulation. Similar to the 4 mm antenna prototypes, the resonance were seen to be at a higher frequency. As opposed to the 4 mm case, two resonances can be seen. The resonance frequency behavior and the final substrate dimensions of the two antennas are given in Table 3.2. The substrate height was again found to be smaller than the intended value of 2 mm. Thus, the resonance frequency shift towards higher frequency is understandable. The two antennas also showed less deviation from each other.

The far-field pattern measurement for the two prototypes is shown in Fig. 3.22 and 3.22. The circular polarization performance was found to be much better than in the case of 4 mm thickness. This is expected as the reflection loss measurements showed two peaks, corresponding to the two orthogonal modes of the patch antenna. For both antennas, the cross polarization level was found to be almost 3 dB.

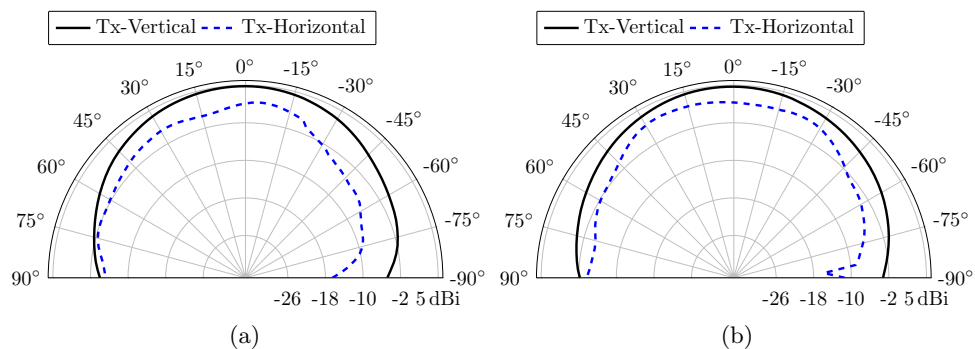


FIGURE 3.21: Far-field measurements in two planes of the fabricated 2 mm prototype 4 at 1605 MHz (a) $\varphi = 90^\circ$ (b) $\varphi = 0^\circ$.

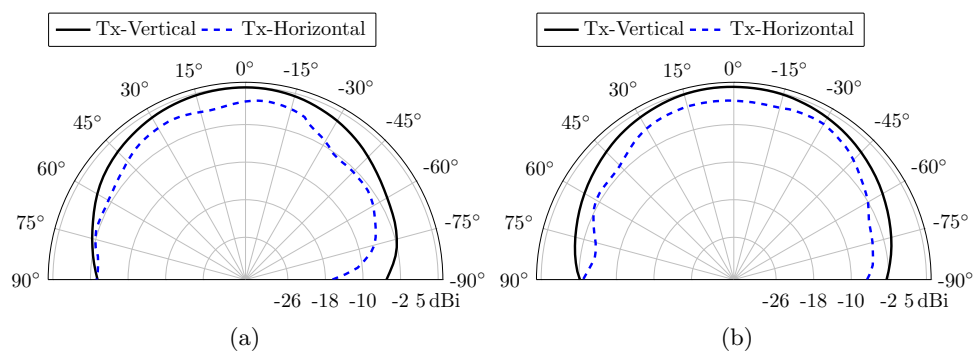


FIGURE 3.22: Far-field measurements in two planes of the fabricated 2 mm prototype 5 at 1596 MHz (a) $\varphi = 90^\circ$ (b) $\varphi = 0^\circ$.

3.1.2 Dielectric resonator antenna modes

Before discussing the DRA designs, it will be helpful to discuss briefly the different modes of DRA and its nomenclature. The two basic shapes i.e. rectangular and cylindrical DRAs will be discussed here.

A DRA can be thought of as a metallic cavity resonator, with the difference that instead of metallic walls the DRA has dielectric-air interface acting as discontinuity. This discontinuity makes DRA a resonant cavity which supports different field distributions or modes which satisfy the Maxwell's equations.

For a cylindrical DRA, the modes are grouped into three categories i.e. Transverse electric (TE), Transverse magnetic (TM) and Hybrid (HEM), where transverse means that the E or H are transverse to the direction of propagation of the wave (usually taken in the z axis). The mode indices are denoted by adding them as subscripts i.e. $TE_{mnp+\delta}$, $TM_{mnp+\delta}$ and $HEM_{mnp+\delta}$. The index m indicates number of full-period variation of the field in the azimuth direction, index n indicates the number of full-period variation in the radial direction. The last index $p + \delta$ indicates field variation in the height of the cylinder, which is usually the broadside direction of the cylindrical DRA. The height of the cylindrical DRA used is usually not an integer multiple of half-period of field variation, thus a term δ is used, indicating a fraction of the half-period field variation.

For rectangular DRA, only TE or TM modes exists. Practically TE modes have been used in the DRA applications. Mode indices are denoted for appropriately describing the mode e.g. $TE_{mnp+\delta}^z$ would indicate that the propagation direction of the wave is taken in the z -direction with m indicating the full-period variation of fields in the x -direction, n indicating the full-period variation of the field in the y -direction and p indicating the full-period variation in the z -direction (usually the broadside). The interested reader is referred to [5, 6, 8] for more details and some visuals of fields of different modal configurations.

3.1.3 Dual-band hybrid monopole dielectric resonator antenna

A DRA can be combined with other radiator to produce hybrid radiation patterns, i.e. to enhance bandwidth or cover multiple bands. One such antenna configuration was developed in which a printed folded monopole and cylindrical DRA made from glass-ceramic were combined to cover frequency bands for WLAN at 2.45 GHz and 5 GHz Hiperlan.

The proposed antenna design structure is shown in Fig. 3.23. It has a folded monopole at the end of the substrate. In the vicinity of the folded monopole a circular DRA is

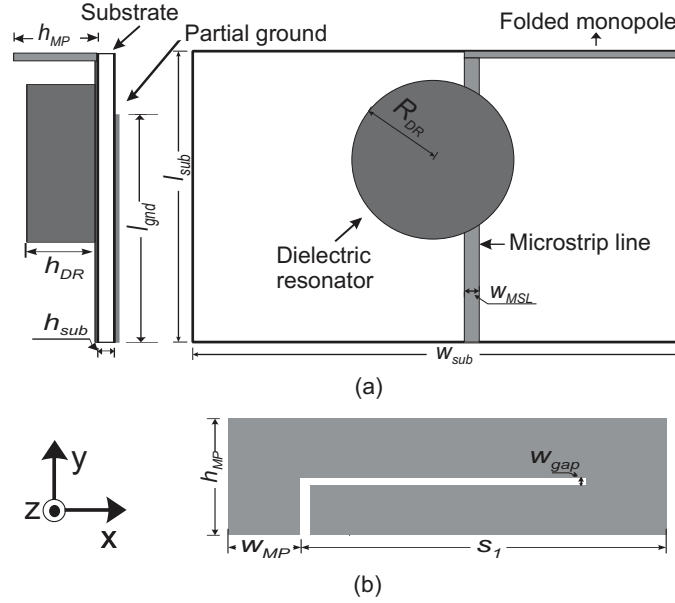


FIGURE 3.23: (a) Side view and top view of the structure of proposed hybrid DRA.(b) Expanded view of the folded monopole.

placed. The structure has a partial ground plane. The whole structure is printed on *Rogers 4003C* substrate which has a $\epsilon_r = 3.66$ and height of $W_{sub} = 0.81$ mm. The feed consists of a microstrip line which extends beyond the partial ground.

Working principal and simulations

CST Microwave Studio was used to design and simulate the dual-band antenna. The most important set of parameters that influence the antenna are the dimensions and permittivity of the DRA, for the upper band and the length of the folded monopole for the lower band. DRA position with respect to the MSL effects the bandwidth and matching for the second upper band only. The lower band is not influenced much by the DRA.

Theoretically, a monopole is essentially $\lambda_g/4$ long section of resonator. Here λ_g indicates the guided wave length. The resonance length required for 2.45 GHz, the $\lambda_0/4$ in a vacuum is approximately 30.7 mm. This will be shortened due to the fact that in this design the monopole is made from a microstrip line which is printed on a substrate with a permittivity of 3.55. The reduction is approximately equal to $\lambda_0/\sqrt{\epsilon_{eff}}$, where ϵ_{eff} refers to the effective dielectric constant of the substrate. As mentioned in [28], this theoretical value is much less than the simulated dimension size, which is usually close to $\lambda_g \simeq 0.75 \times \lambda_0$. Further complications arise due to the fact that in this case the monopole is folded and also in placed in the vicinity of high dielectric material.

Therefore, full 3D simulations are needed to optimize the length of the monopole for resonating at the designated frequency.

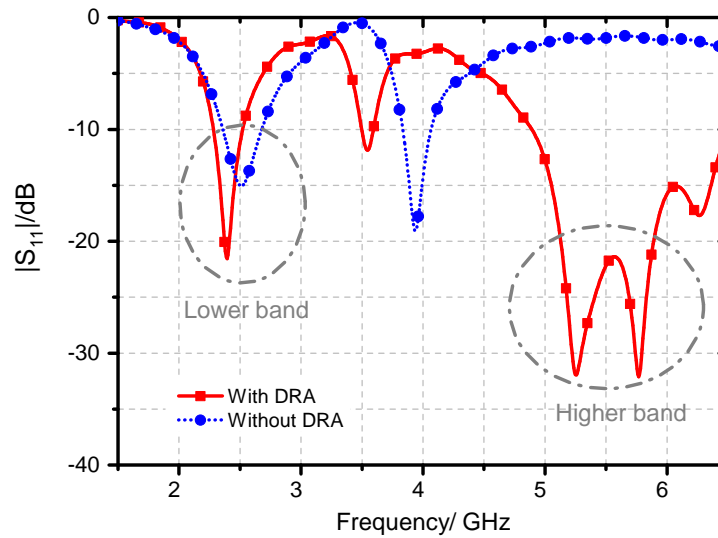


FIGURE 3.24: Simulations showing the influence of the DRA in the design.

For covering the 5 GHz WLAN band, a cylindrical DRA (CDRA) was used. A CDRA is known to excite the HE_{11} mode when placed asymmetrically on a microstrip line [29]. The resonance frequencies for a cylindrical DRA can be calculated as given in [30]. It is in Table 3.3. For the dimensions used in this work, the resultant HE_{11} and EH_{11} resonances were calculated to occur at 5.82 GHz and 5.7 GHz. These formulations are actually carried out with specific boundary conditions enforced on the resonator. However, in this case, there was a partial ground plane used, and therefore, deviation from the theoretically calculated resonances is expected. The microstrip line plays also a role in changing the boundary conditions of the cylindrical DRA and hence, resonance frequency would deviate or de-tune from the calculated values. The EH_{11} , observed from the field distributions and far field patterns, is located at 5.2 GHz. These two modes combined, cover the bandwidth of interest completely.

TABLE 3.3: The eigenmodes of the circular DRA.

Mode Type	TE_{01}	HE_{11}	EH_{11}	TM_{01}
f_o (GHz)	3.9855	5.82	5.70	6.54

The implementation of the DRA introduces new resonances at the higher band, while leaving the lower band resonance frequency almost unaffected. The effect of the DRA can be seen in the Fig. 3.24. The independence of the two bands is of importance in multi-band antenna as it makes it easier to design the two bands when they are independent of each other. Another resonance band can also be seen in between the upper and lower bands, this was not studied further but with careful design it can also

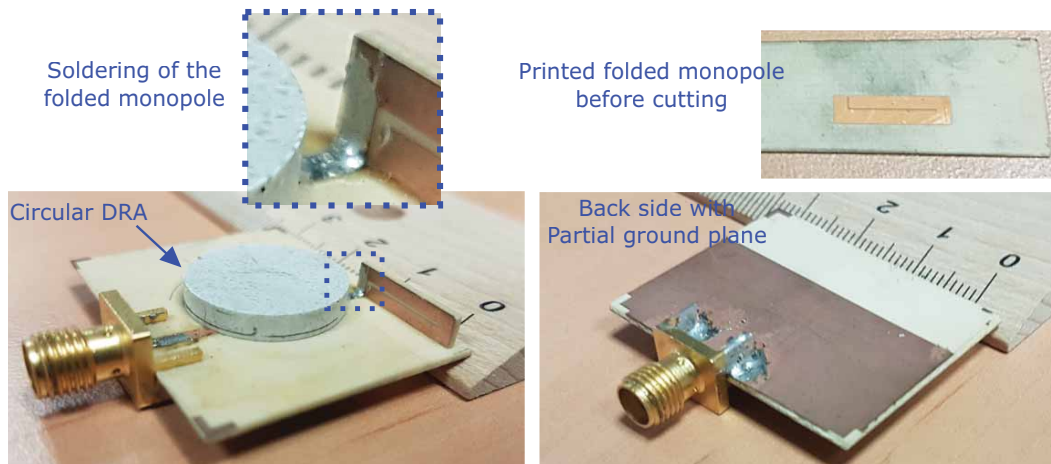


FIGURE 3.25: The constructed prototype of the proposed antenna. The soldering junction and printed monopole on a substrate before cutting is also shown.

be used to cover the additional WLAN 3.65 GHz band which is defined as the IEEE 802.11y (3.65 – 3.7 GHz).

Fabrication of the antenna

The fabricated antenna is shown in the Fig. 3.25, along with the printed monopole before dicing it from the substrate. The folded monopole was constructed along with the photolithography process of the substrate. It was printed on the same substrate and later cut out of the substrate with dicing machine. It was then glued to the microstrip line at the end of the substrate. The DRA was manufactured from glass-ceramic material. The material was measured to have permittivity of 22.5 and loss tangent of 0.005 at approximately 7 GHz. The circular DRA was cut in exact dimensions by machining from a piece of the glass-ceramic.

Measurement results

The reflection loss measurements and simulation results are shown in Fig. 3.26. They corresponded well with each other. The return loss for the lower band at 2.45 GHz was close to 12 dB. This could be attributed to the meeting point of the folded monopole and MSL. Soldering was used to connect the two, which due to imperfection disturbed the matching to some extent. The antenna still provided -10 dB impedance bandwidth of 2.6% at 2.45 GHz. The upper band showed also a good match between simulation and measurement. Two resonant frequencies were measured at 5.1 GHz and 5.8 GHz. The -10 dB impedance bandwidth for the upper band was 23%. The maximum return

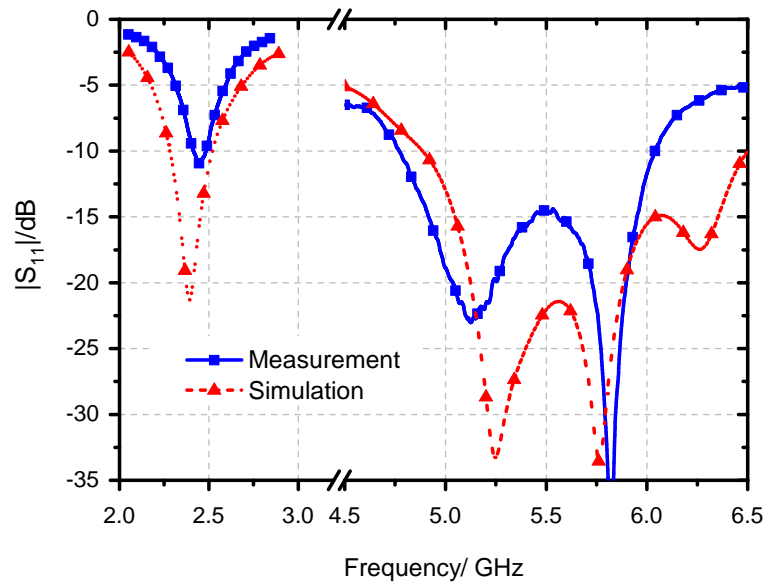
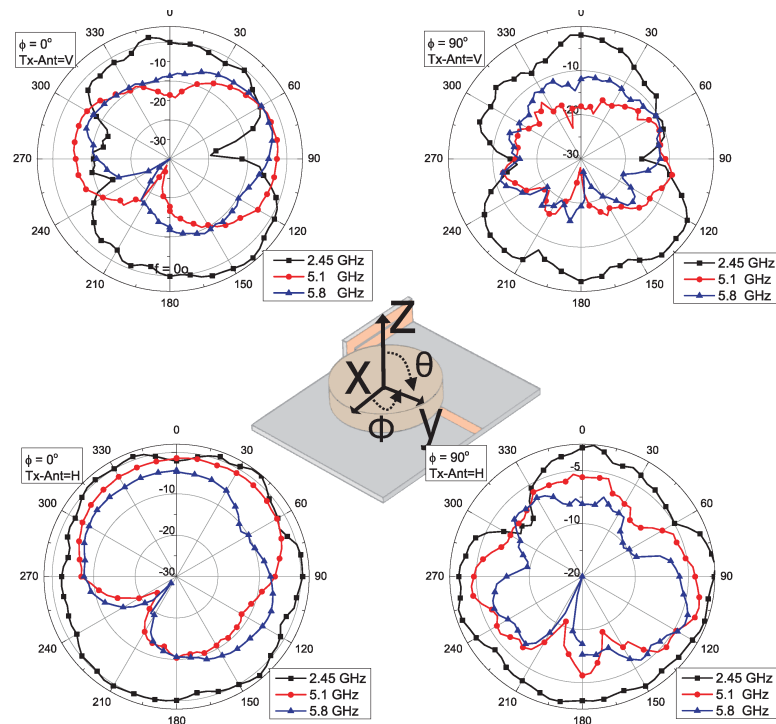


FIGURE 3.26: The simulated and measured reflection loss.

FIGURE 3.27: Measured radiation pattern of the proposed antenna with rotation of DUT in the θ plane.

loss in the whole 5 GHz WLAN band was below 15 dB. The simulated total efficiency is above 80% for all the operating bands.

The radiation patterns for the fabricated antenna were measured in an anechoic chamber. The results are shown in Fig. 3.27. The four sub-figures show, the patterns for three different frequencies at $\phi = 0^\circ$ and $\phi = 90^\circ$ plan, each with the transmitter antenna

in vertical and horizontal polarization. The patterns were all normalized with reference to the maximum value for the vertical and horizontal transmitter antenna. The attenuation in the upper band is higher as expected due to the high free space propagation loss. Theoretically, a difference of almost 8 dB should exist between the lower resonance frequency and the highest resonance frequency, which is what is observed in the measurements. The pattern for the monopole at 2.45 GHz can easily be identified by the typical bidirectional shape, with high radiation in the broadside direction and null in the end-fire direction. But since it is electrically small antenna, the pattern will not be very prominent with the typical pattern shape. The patterns are normalized for the maximum received power in each band. Both the 5.2 GHz and 5.8 GHz are quite omnidirectional with a minima around $\theta = 240^\circ$. The E-field orientation (E-plane) in the far field, in simulations was noted to be at an angle of almost $\theta = 40^\circ$ and straight. Therefore, it would be necessary to tilt the antenna at this angle to get the E-plane and H-plane. Since the antenna was measured without any tilt the transmitter antenna polarization had little effect. This is the reason, why we see little change in the case when the transmitter antenna is vertically oriented (Tx-Ant=V) and horizontally oriented (Tx-Ant=H).

3.2 Transparent antennas

Optically transparent antennas have been attracting increasing research interest in recent years. Due to their transparency to the visible light, such antennas can be preferably implemented on top of various clear surface like windows, screens and glasses for security, aesthetics and vehicles applications [31]. But perhaps the most sort after use of such antennas is their suitability for integration with solar cells [32]. This concept is very useful for applications in small satellites and power harvesting wireless devices like sensors. Antennas integrated on a solar cell has not been a new concept, many researchers have combined simple antennas with solar cells [33–36]. There are mainly two approaches taken to handle the problem of an antenna integration on or with a solar cell. The first method is to use ordinary metal e.g. copper but in such a way that it blocks minimum solar energy from reaching the solar cell. In the second method, transparent antennas are made out of a transparent conducting film. Both these approaches will be briefly described in the following section.

In the first approach, researchers have used common metal that is used for non transparent antennas but in such a way not to block the sunlight. A mesh of conductors is used instead of full conductor sheets to make the radiating element, e.g. a patch [37]. In this way, one can achieve the desired antenna characteristics as a normal antenna would have

but at the expense of efficiency. Since a lot of the metal is removed from the radiator, the currents are confined to the thin or less metal parts and as a result, more conductor losses occur. Also the metal although removed but still some of it is left, will block some of the sun energy. The mesh is generally formed by metallic strip fabricated directly on top of target surface. The patterning of the mesh is through typical printed circuit board technologies such as milling or etching. One should note, that such antennas are especially suitable for cases where patch radiating element are used. Recent research [38] has identified that such mesh can be transparent up to 80% with reasonable radiation efficiency of 50%. In SOLANT project the researcher have incorporated slot antenna in the ground of the solar cell for integration [39], but this requires custom manufacturing of the solar cells.

The second method for transparent antennas is that of using a conducting transparent film as a conductor. Such transparent conductive films allow reasonable trade-offs between transmission of electric currents and affordable optical transparency [31]. Previous researchers have used different films including silver coated polyester film (AgHT), indium tin oxide (ITO) and fluorine-doped tin oxide (FTO) [40]. Besides the moderate optical transparency of e.g. less than 80 % with ITO, such antennas have another major limitation, i.e. the conduction loss through the thin film due to the skin effect. On one hand, the transparency is effected when thick films are used but on the other hand, thin films will introduce more conductor losses. Thus antennas built with transparent conductive films suffer from drastically reduced total efficiency which becomes severe as the operating frequency is increased. The other main issue with using, e.g. ITO film, is that it contains indium which is a rare earth metal, and hence, expensive. Also in general, a film must be deposited under special vacuum conditions which makes it difficult to manufacture. The conductivity of transparent films is quite low ($5 \times 10^5 S/m$) [41], which make it in order of 10^2 less conductive than copper, and hence, reported gains are quite low. A study on ITO film in [40] reported the highest efficiency value of only 40 % at maximum frequency of 7 GHz. In conclusion, apart from being unsuitable for mass production, the ITO based transparent antennas are not very efficient.

In this work, the antennas use none of the above mentioned methods. The antenna is a dielectric resonator antennas (DRA). The material of the DRA (in the first demonstrators) is a transparent glass which is actually the precursor of the glass-ceramic. But instead of ceramization of the glass, it is used in the un-ceramized form. The second antenna demonstrator was made from *LASF35* clear glass [42] from SCHOTT AG Mainz.

3.2.1 Transparent antenna from non-ceramized low loss high-k glass

The bulk-glass ceramics are actually ceramized from a bulk-glass sample. Such a bulk-glass before ceramization is shown in Fig. 3.28 (left). It has a yellowish appearance. The sample has a glossy texture, which do not seem fully transparent. The transparency improves once it is polished. Such polished rectangular cut pieces can be seen Fig. 3.28 (right). The transparent glass was measured by the Hakki-Coleman method and was found to have a relative permittivity value of 17.5 and $\tan\delta$ of 0.007. These values seems suitable for implementation in a DRA antenna.

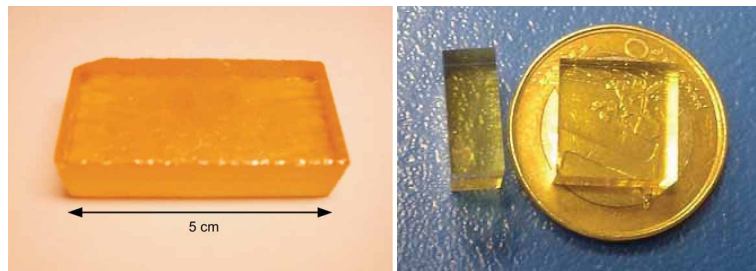


FIGURE 3.28: Bulk-glass slab (left) and polished cut rectangular pieces (right).

Simple antenna configuration

To test the values measured first, the simplest possible DRA is fabricated: a rectangular DRA placed on a simple microstrip line non-symmetrically to excite the $TE_{\delta 11}$ mode. The fabricated DRA is shown in Fig. 3.29a. The fabricated antenna used *Rogers 4003C* with thickness of 0.81 mm. Such configuration produces a broadside radiation pattern antenna. The DRA's precise location is determined from the simulation and is marked with small markers on the substrate. The transparent bulk-glass slab was precisely machined to make the $12 \times 12 \times 5$ mm DRA. It was then polished for clear transparency. The polished DRA is then glued onto the substrate in the marked position.

The reflection loss measurements and simulations are shown in the Fig. 3.29b for the fabricated antenna. The measurements shows almost a perfect agreement with the simulations. This was a validation of the full process steps from characterization of the material to simulations, and then, finally characterizing the fabricated antenna. The -10 dB bandwidth achieved for this simple DRA was about 9%. This is better than a simple patch configuration. Another prototype was then simulated and fabricated with an increased bandwidth, which is explained in the next section to follow.

The antenna measurements of the two principal planes in the anechoic chamber are shown in Fig. 3.30. The gain was measured to be 5.6 dBi. The cross polarization levels

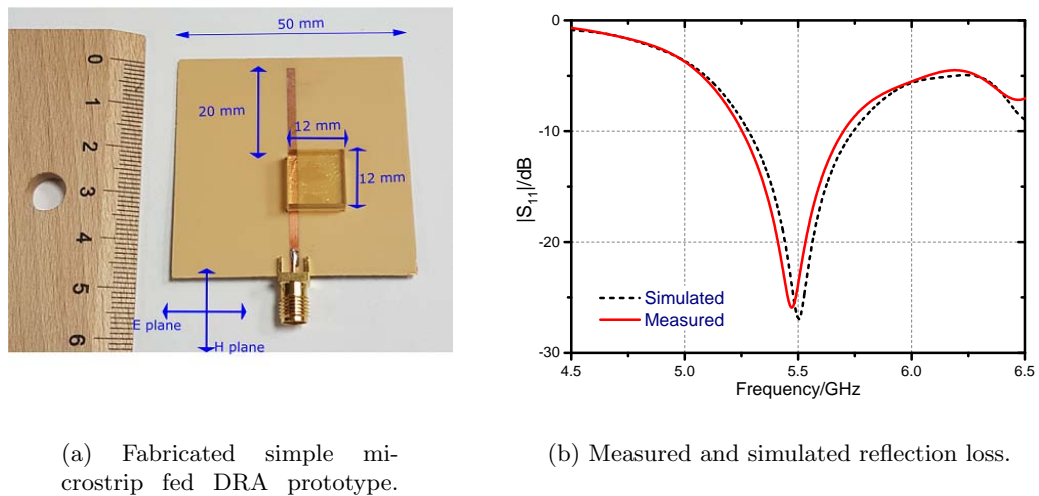


FIGURE 3.29: Fabricated prototype with measured reflection loss.

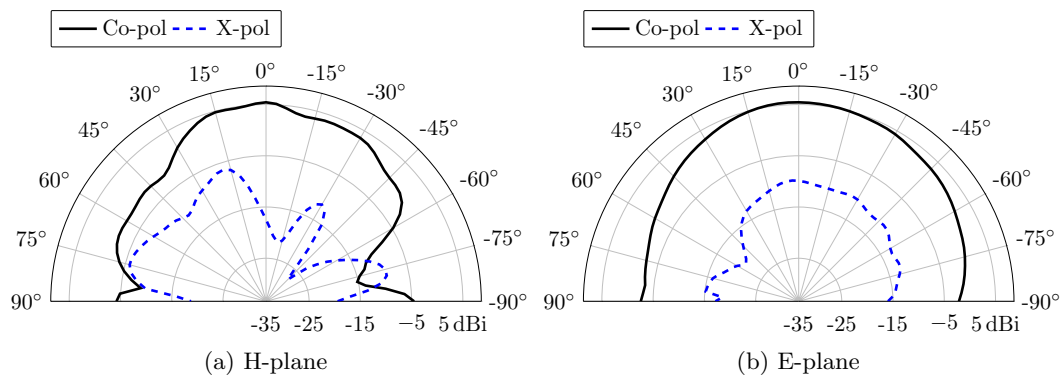


FIGURE 3.30: Antenna patterns measured in the two principal planes of the fabricated prototype at 5.5 GHz.

in both planes were almost 14 dB. Thus, a linear polarization behavior is measured as expected.

Wideband antenna configuration

For increasing the bandwidth of the previous design, the microstrip feed line was modified. The modified structure of the feed-line with the same DRA is shown in Fig. 3.31. The DRA size and material was kept the same as previous antenna.

The 50Ω microstrip line is now modified such that it has an additional strip at a distance $d_l = 5.1$ mm from the end of the line. This strip is perpendicular to the microstrip line feed itself. This additional strip disturbs the fields in the DRA and produces another resonance. The influence of the d_l and s_l is shown in Fig. 3.32. The simulations

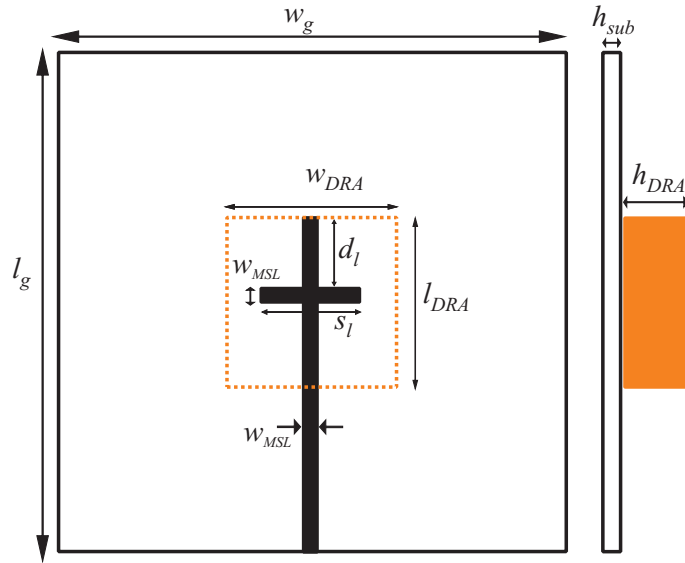


FIGURE 3.31: Geometry of the proposed wideband antenna configuration design.

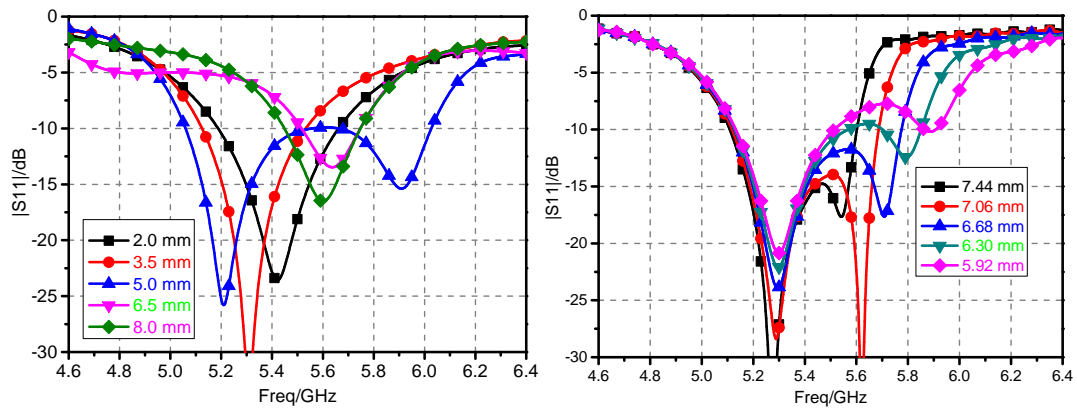
(a) Simulation results, showing the variation of the resonances, depending on the distance d_l of the added strip.(b) Simulation results, showing the variation of the higher resonance, depending on the length s_l of the added strip.

FIGURE 3.32: Effect of the length and position of the strip.

show that the addition of the strip to the feed line introduces another resonance in the reflection loss measurements. The length of the strip s_l directly controls the second resonance. As the length is reduced from the value of 7.44 mm to 5.92 mm, the resonance moves from 5.55 GHz to 5.9 GHz. The matching bandwidth is thus controlled by the optimized length of this strip. Another significant conclusion from the same graph is that while the second resonance varies with the length of the strip, the first resonance remains constant. Hence, the added strip length s_l controls the second resonance independent of the first one. Similarly, the position d_l of the strip has a great influence on the matching. The reflection loss graph of the DRA shows that only for a certain optimized distance there are two resonance peaks. Therefore, it must also be optimized for the required matching.

TABLE 3.4: Parameters of the fabricated wideband transparent antenna.

$W_g L_g$	W_{DRA}	L_{DRA}	H_{DRA}	d_l	s_l	W_{MSL}
60 mm	12 mm	12 mm	5.1 mm	6.4 mm	5.1 mm	1.8 mm

When the fields at the two resonances are observed it is noticed that the first resonance is from the fundamental $TE_{\delta 11}$, while the second resonance mode is from the $TE_{\delta 21}$ mode. This second resonance is purely introduced due to the strip implemented in the feed line. The second mode although cannot be regarded purely $TE_{\delta 21}$ as the field in the y-axis are not completely filling the y-dimension length of the resonator as shown in Fig. 3.33. But it can be approximated as TE_{121} . This mode is also not purely due to the dielectric resonator, but a combination of the added strip and dielectric resonator. The electric fields in the two modes are shown in Fig. 3.33. The lower resonance fields are covered in the whole dielectric resonator, the fields of the second resonance at 5.8 GHz shows to be produced by the added strip. The second resonance fields originated from the end of the resonator and ends on the added strip. Such configuration will not be possible without the presence of the strip.

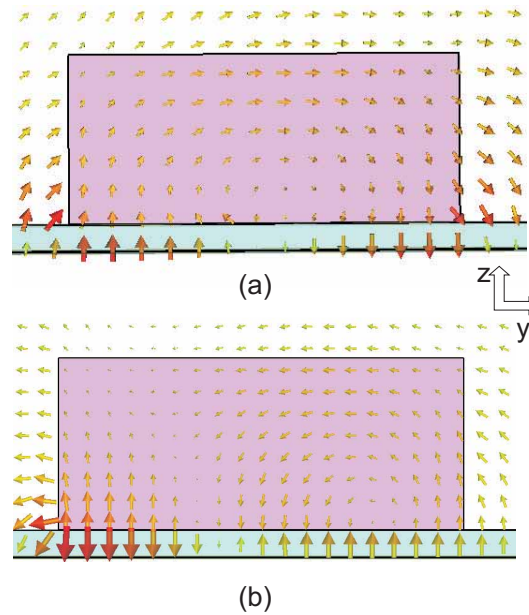


FIGURE 3.33: Electric field configuration in the resonator (a) 5.2 GHz (b) 5.8 GHz.

The simulated total efficiency at 5.2 GHz and 5.8 GHz were computed to be 94% and 82%, respectively. As was discussed, the second resonance involved the strip, and hence, some metallic losses incurs, which reduced the efficiency.

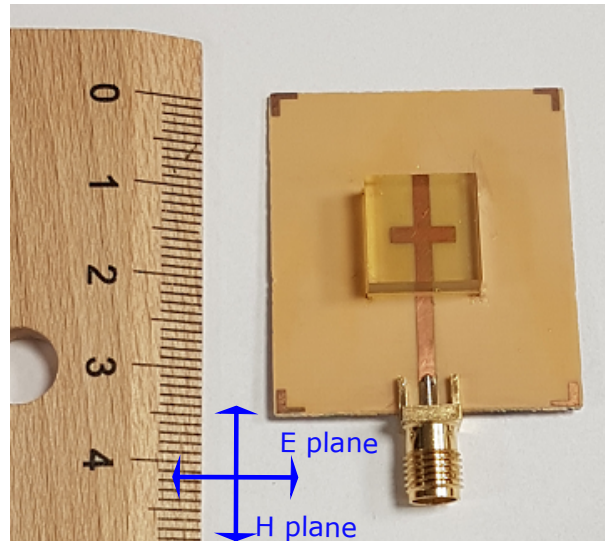


FIGURE 3.34: Fabricated prototype.

Measurement results

CST Microwave Studio was used to optimize the values of d_l and s_l to get the two resonance resonances around 5.2 GHz and 5.8 GHz. The optimized design parameters are shown in Table 3.4. The fabricated antenna is shown in Fig. 3.34. The resonators are glued to the substrate at the appropriate positions, using four small markers. The microstrip line structure with the added strip is etched on the substrate via standard photolithography and etching process. A small ground was used to fabricate the prototype. In this way more designs were manufactured with different strip lengths and distances to compensate for any inaccuracies in the simulations and fabrication. This also validated the strip length and distance influence with measurements.

The return loss was measured with a vector network analyzer, shown in Fig. 3.35 along with the simulated values. Both curves show a good fit to each other. The measurements can be seen to be shifted towards higher frequencies, due to the application of the glue and some machining inaccuracies of the DRA. The thin glue layer lifts the DRA up and due to the low permittivity of the glue mimics an air gap between the DRA and substrate. This shifts the resonance frequencies upwards.

The first resonance is measured at 5.3 GHz. The second resonance occurring at 6 GHz. The -10 dB bandwidth measured is around 18% ranging from 5.2 GHz to 6.2 GHz. This value is equal to double for that of the simple microstrip line DRA of the previous section.

The fabricated prototype was measured in the anechoic chamber, the far-field radiation pattern are shown in Fig. 3.36 and Fig. 3.37. The measurements show the far-field pattern at 5.3 GHz and 5.9 GHz. The antenna has a broadside pattern. The far-field shows

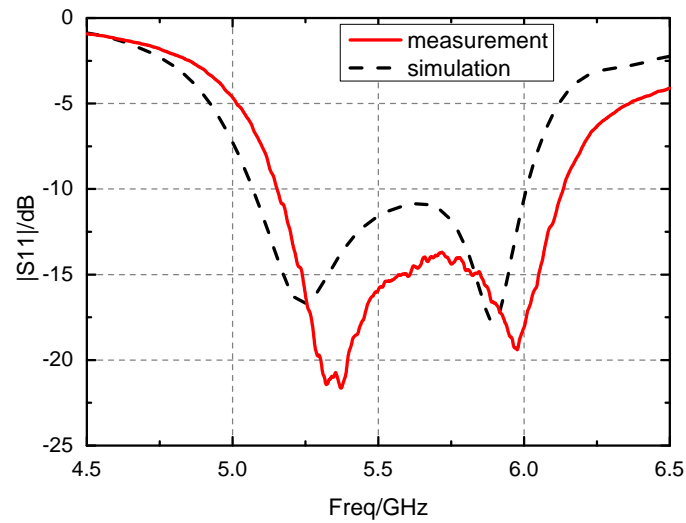


FIGURE 3.35: Simulated and measured return loss.

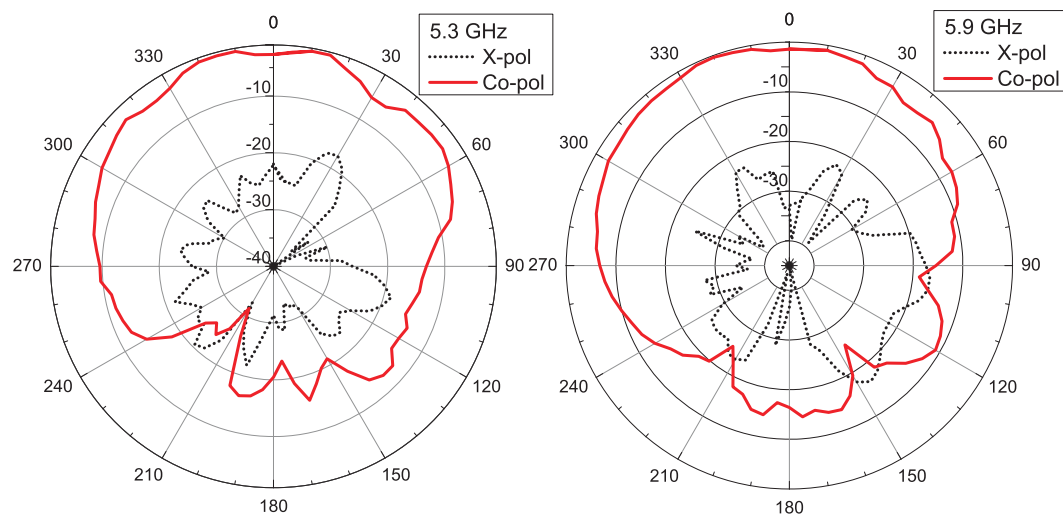


FIGURE 3.36: Measured H-Plane radiation pattern at the two resonances.

almost 20 dB difference in the received power in co-polarization and cross-polarization levels. Thus the antenna has linear polarization.

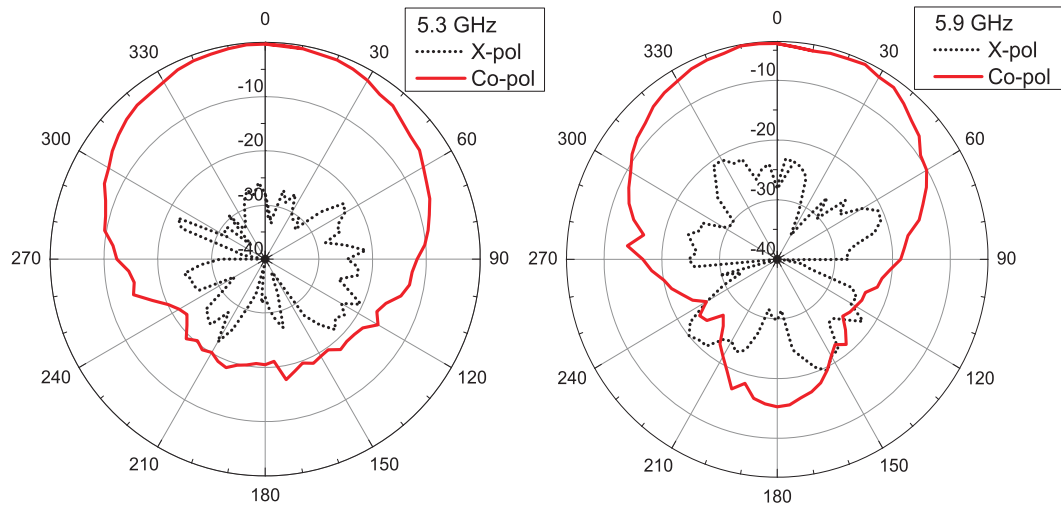


FIGURE 3.37: Measured E-Plane radiation pattern at the two resonances.

3.2.2 Transparent antenna demonstrator on top of a solar cell module

The antenna presented in the previous section was a natural idea seed to be used on a solar panel. The significance of solar cells has seen a tremendous increase in the last years, since the idea of renewable and clean energy has become focus of many governments. Many stand-alone terrestrial communication systems are powered usually with the help of solar cells [43–45]. Another very significant use of solar cells is in the satellite systems. The solar cells are the primary source of power for the satellite. The problem with satellites is that it has a limited surface space [46] in which both, antennas and solar cells must be fitted. Therefore, integration of antennas with the solar cells would prove advantageous with many potential applications. This section presents transparent glass based DRA placed on top of an off-the-shelf solar panel.

Solar cell construction

The first step in simulations of an antenna with a solar cell is to model the solar cell. The model is required in order to simulate in a electromagnetic solver software. Although the exact structure of the solar cell used in this prototype was not available, a general structure of the solar cell structure was used as a model which was derived from online search and from literature [36]. The model consists of a top glass or plastic coating, which is just a protective layering. The protective layer thickness differs for solar modules from different manufacturer, a value of less 1 mm seemed a reasonable one, which also was observed by examining the solar cell physically. Since this is usually a cheap plastic or glass, the permittivity value was estimated to be 4. A cathode lattice which is essentially a grid of thin metal lines are present under the protective coating. This layer collects the

electrons which are set free by the sun light striking the solar panel. The lines obstruct sunlight, and hence, usually are made as thin as possible but enough thick to collect the current. These lines can be modeled easily for the electromagnetic solver by observing the particular solar cell. The model of the solar cell used in the simulations is shown in layered form in Fig. 3.38.

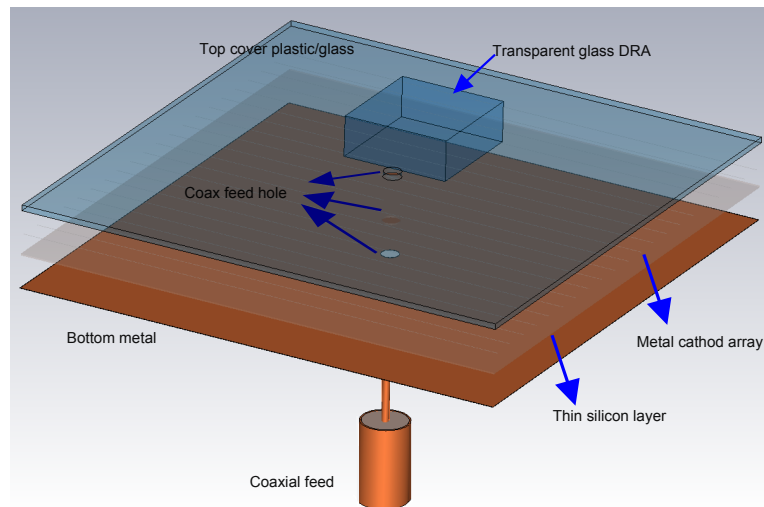


FIGURE 3.38: Layout of transparent DRA on a solar panel with coaxial feedline.

At the heart of a solar cell there is essentially a silicon layer forming a pn junction. A simple pn junction is shown depicted in Fig. 3.39. Such a junction is achieved by doping a silicon wafer with p and n type material. The reader is referred to [47] for more details. The solar cells now usually consists of a 200 μm . The accurate parameters for this layers are unknown, so they are modeled by a bulk silicon material with a permittivity of 12.9 and $\tan\delta$ of 0.1. These values will not have much influence on the performance during simulations, since the layer is very thin as was confirmed by the simulations, which will be shown later. The modeling also ignored some features which usually are a part of the standard process. For example thin layers of special anti reflective coatings are also applied, but the thicknesses are in nanometer range. Also the silicon surface is grooved for better anti-reflection performance. But for the electromagnetic simulations these can be easily ignored, especially when the wavelength of operation is many orders of magnitude than the small structures.

Transparent DRA on a solar cell

This design used a solar cell available commonly in the electronic store [48]. It is a 57 x 65 mm. In order to use the coaxial line for the electromagnetic coupling a hole with a diameter of 1.5 mm was made in the center of the solar cell shown in Fig. 3.38. This inner conductor pin of the coaxial line penetrated the solar cell through this hole to

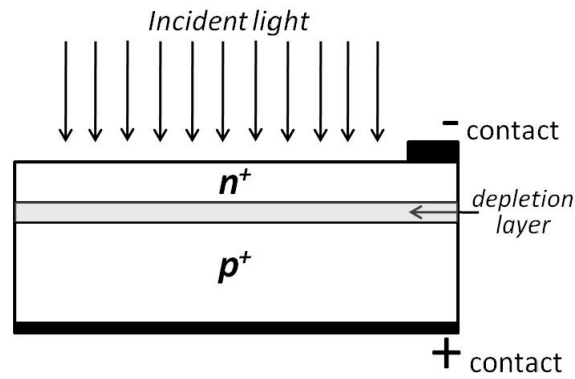
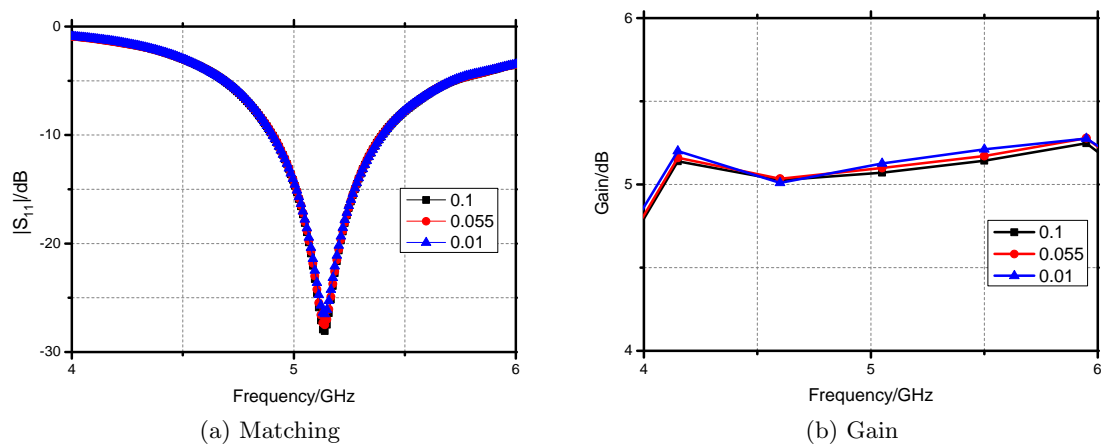


FIGURE 3.39: Generic p/n junction structure and photovoltaic cell [47].

FIGURE 3.40: Simulations to assess the influence of $\tan\delta$ in thin silicon layer.

reach the DRA on top. The hole indeed removes some material and would lead to very minimal degradation in the performance of the solar cell. The area destroyed by making this hole is very less and hence can be ignored. The area destroyed is in fact only 0.16 % of the total solar module area for this particular solar cell module. The center coaxial pin extended from the coaxial cable to almost the height of the DRA. This effectively couples the electromagnetic energy into the DRA in the well known $TE_{\delta 11}$ mode. The DRA is placed on the top of the solar cell touching the feed pin. The distance or gap between the pin and DRA effects the degree of coupling.

The backside of the solar cell module show two connection points labeled + and -. The back plane of the solar cell which is usually Aluminum or Copper is connected to the + terminal. Hence, the copper plate, which is the RF ground in this case, should be shorted with this terminal. Some insulation tape was applied to the - terminal to isolate it from the copper plate. Influence of shortening of one or the other terminal with the RF ground will be shown later in the measurements.

The DRA used in the section before was yellowish in color. The DRA used above the

TABLE 3.5: LASF35 glass microwave characterization in Hakki-Coleman setup at 6 GHz

	ϵ_r	$\tan\delta$
LASF35	20	0.006

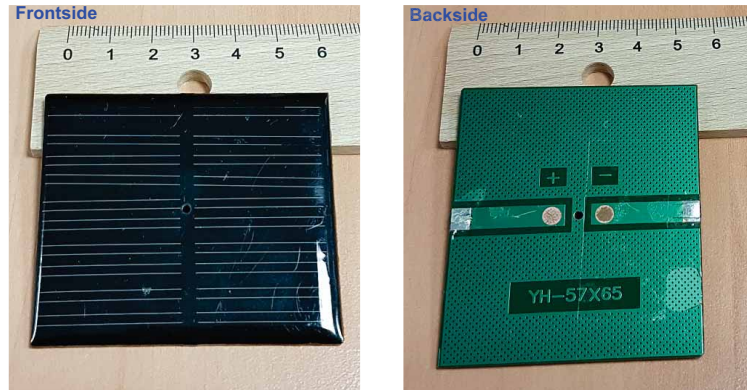


FIGURE 3.41: Solar cell module with a hole.

solar cell was manufactured from LASF35 optical glass [42]. This glass is a clear white transparent, and hence, have more transparency than the yellow one. The glass was first characterized and the values are shown in Table 3.5. The characterization also showed that the permittivity was also more as compared to the 17.5 for the previously used yellow one. This would enable smaller antenna size. This is also for the first time that a commercially available transparent LASF35 glass is used for DRA construction.

The simulations were performed for 5.2 GHz. The height of the pin is the most important parameter for the coupling to the DRA. Usually the pin is kept longer than needed and then, cut piece wise from the top while the structure is connected to a vector network analyzer. The cutting could be stopped when adequate coupling is seen by observing the reflection loss.

In spite of the fact, the silicon layer being the most important ingredient for the solar cell, but it plays less role in the overall antenna structure. This is because it is very thin(200 μm). Simulations showed that changing the loss of this layer had very negligible effect on the matching and gain of the antenna, shown in Fig. 3.40. The $\tan\delta$ of the material was changed from 0.1 to 0.01, where the gain and matching remained nearly constant.

The size of the dielectric resonator used is the same as was used in the previous section. The theoretical resonance should occur around 4.7 GHz. But these calculations are based on the geometry in which the DRA is placed above an infinite ground plane. But in the case when the solar cell is placed between the DRA and the ground plate, the resonance should move to the high end of the spectrum. This is logical, since the

effective permittivity is decreased by the low permittivity material that is placed in the path from the DRA to the ground. In addition, the limited size of the ground plane will deviate the calculated resonance frequency to some extent.

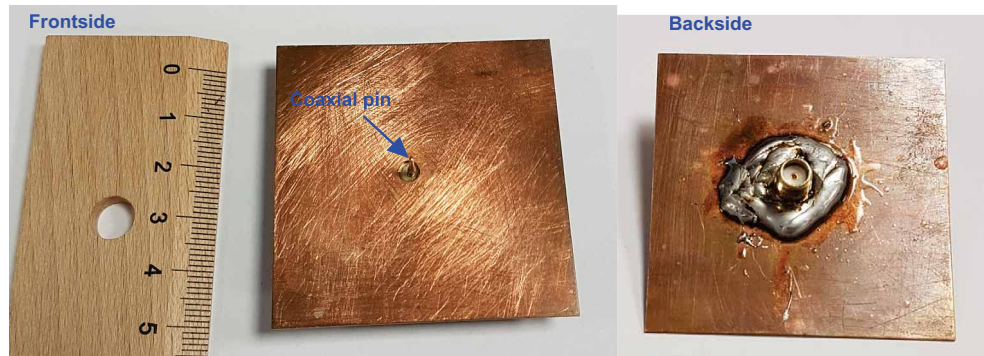


FIGURE 3.42: Copper plate fixture with coaxial connector for the Solar cell module.

A copper plate measuring 55×55 with a hole in the center was used as the ground plane for the input coaxial connector. A coaxial connector was soldered at the back side such that the connector aligned with the hole in the copper plate. The front and back side of the copper plate with soldered coaxial connector is shown in Fig. 3.42. The center conductor of the coaxial connector has a hole conductor. A metal pin is inserted in this hole, this will make the coupling pin for the transparent DRA.

The transparent DRA was glued to the solar cell module such that the E-field of the DRA is in parallel to the conductor lines. The finished prototype is shown in the Fig. 3.43. The reflection loss measurements were performed with a vector network analyzer after the gluing of the DRA. The results of the measurement are shown in Fig. 3.44. The resonance of interest is reasonably well placed as in the simulations. The measurements overall show better matching and wider bandwidth, which is attributed to the higher losses present than accounted for in the simulations, using the ideal model.

The S_{11} shows curves for the cases when the copper plate is shorted with either the + or – terminal at the back of the solar cell module. The S_{11} in the case the back plane is shorted shows a better matching, which is expected as this is what was modeled in the simulations. In the case when the anode line of the solar cell module are shorted with the copper plate the matching degrades to some extent.

The overall result showed a shift towards higher frequency. To investigate further this shift, the model was changed to include another layer of FR-4 material between the silicon and ground plane (or back plane of the solar cell). FR-4 is probably the most common substrate material used in the electronic circuits due to its low cost. This layer was not included in the simulations of the ideal model of the solar cell used for

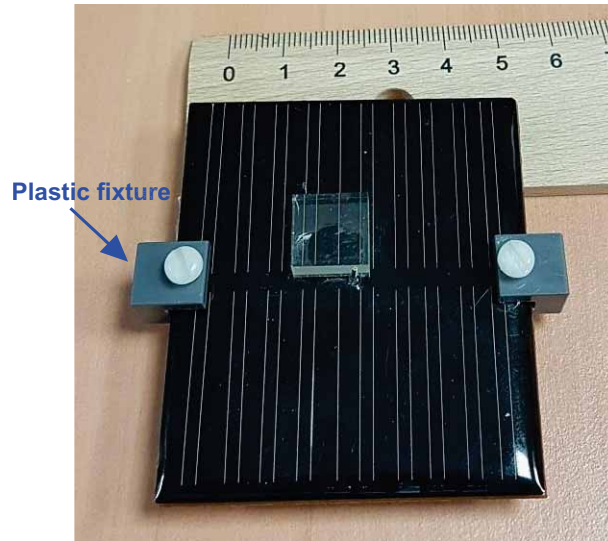


FIGURE 3.43: Solar cell module with transparent DRA glued with the plastic fixtures for attaching the copper plate.

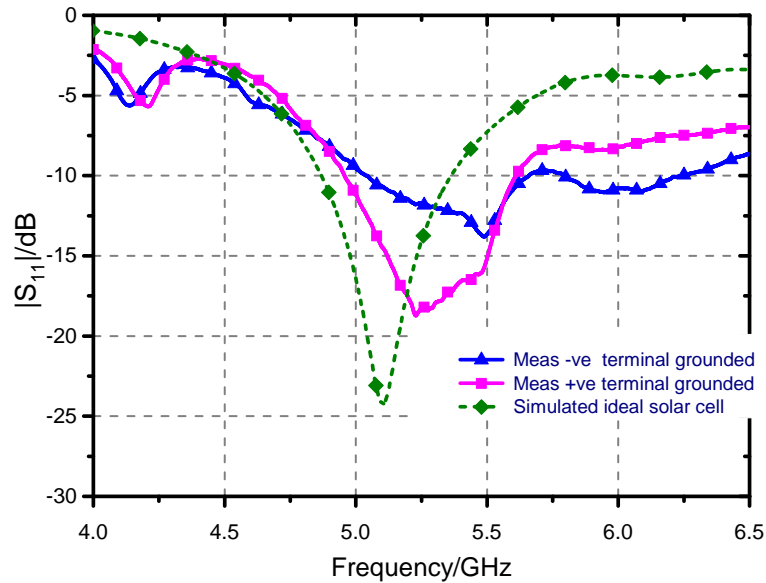


FIGURE 3.44: Reflection loss measurements of the transparent DRA on a solar cell module with two conditions as compared to the simulations of the ideal solar cell.

simulations. The height of the FR-4 layer was roughly measured and approximated to be 1.2 mm. The simulation results after this added FR-4 layer are shown in Fig. 3.45

The transparent solar DRA was then measured in an anechoic chamber for the far-field pattern performance. The two principal planes of the fabricated prototype are shown in Fig. 3.46. The solar cell size (and copper plate size) was quite small, i.e. only $1\lambda \times 1.1\lambda$, therefore some widening of the beam in the upper hemisphere should be expected. Nevertheless, the measurements showed a gain of 4 dBi. This gain is a very good value for such a simple design. The cross-polarization level was measured to be 12 dB. It should be noted that the gain can be improved further along with the

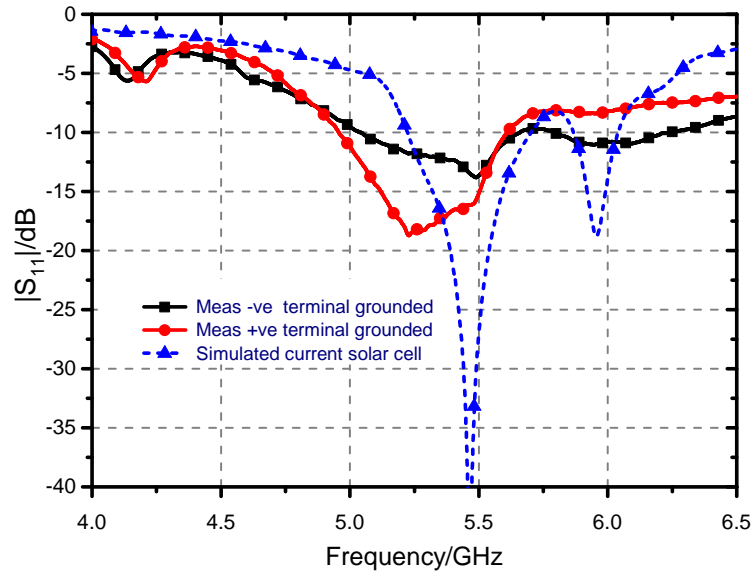


FIGURE 3.45: Reflection loss measurements of the transparent DRA on a solar cell module with two conditions as compared to the simulations of the currently used solar cell including FR-4 layer.

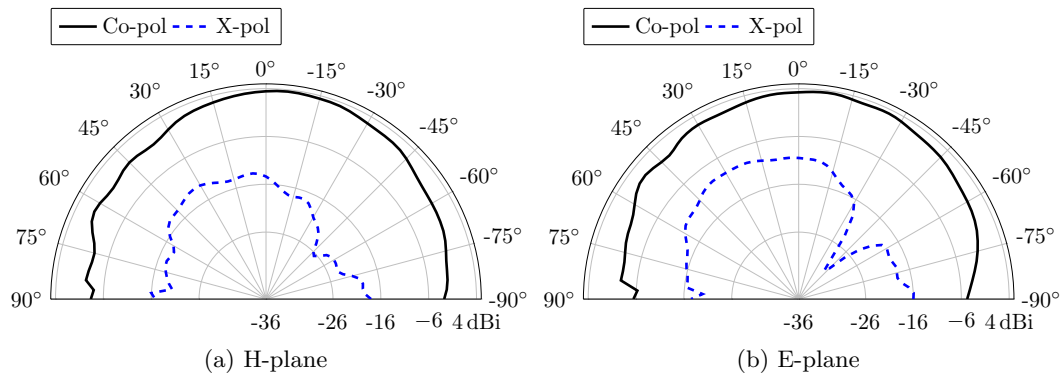


FIGURE 3.46: Antenna Patterns measured in the two principal planes of the fabricated solar transparent DRA prototype at 5.2 GHz.

bandwidth when stacked DRAs are used. Since the material used is transparent stacking does not shadow the solar cell.

As compared to the techniques of mesh antennas or transparent film antennas for solar antenna, this antenna used a transparent DRA. The other techniques loose gain due to the fact that both meshing and transparent films increase the conduction losses. The DRA on the contrary is a highly efficient radiator. Therefore, any decrease in the gain value is due to the solar cell itself. To compare the loss, the solar transparent DRA antenna was fabricated but this time without the solar cell, e.g. only with a copper plate. The fabricated transparent DRA on the copper plate is shown in Fig. 3.47 along with the reflection loss measurements. The reflection loss measurements are very close

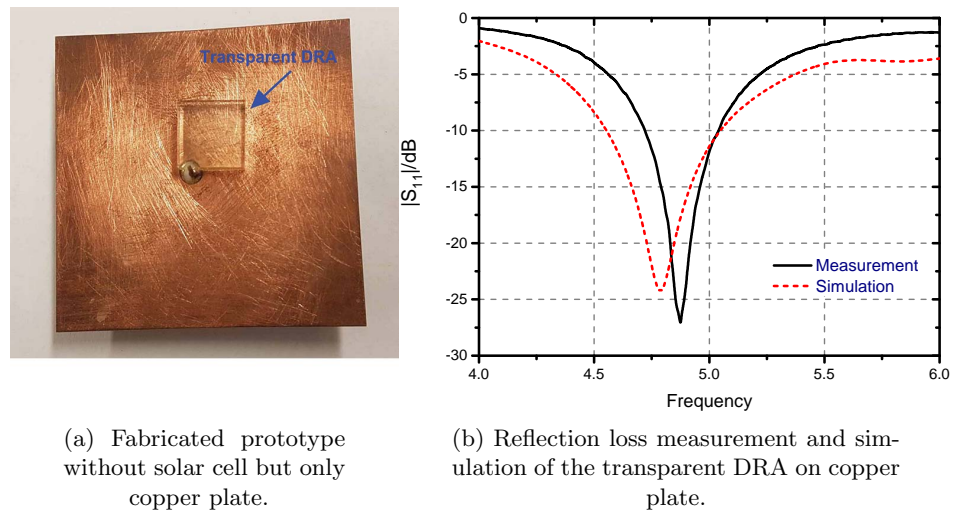


FIGURE 3.47: Transparent DRA on Copper plate for comparison with solar cell module.

to the simulations. Some of the mismatch is occurring due to the deviation in the copper plate flatness and size of the DRA antenna.

The transparent antenna on the copper antenna was then measured in the anechoic chamber. The antenna patterns measured in the two principal planes are shown in Fig. 3.48. The far-field radiation resembles that of the solar cell module. The difference, however, is that the gain is 5.7 dBi. This value is 1.7 dB more than when the solar cell module was used. Therefore, it can be concluded that the solar cell module causes some losses of about 1.7 dB. The cross polarization level is also better in the case of the copper plate. The cross polarization level is measured to be almost 15 dB. This is understandable as the solar cell module has a complex structure, and hence, the polarization purity of the far-field is disturbed.

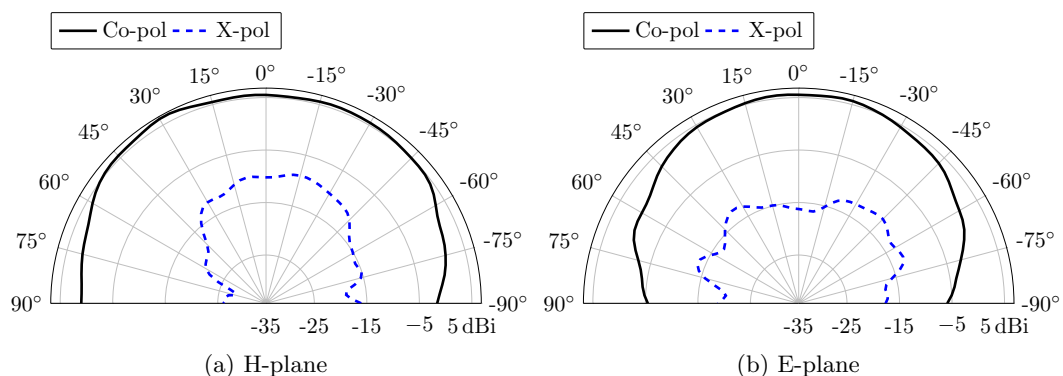


FIGURE 3.48: Antenna pattern measured in the two principal planes of the transparent DRA on the copper plate at 4.8 GHz.

The transparent DRA has proved to be an easy solution for solar-cell integrated antennas. A moderate gain antenna was demonstrated on an off-the-shelf solar cell module. In

research, where the solar cell manufacturing can be also done in the lab, more possibilities and better solar-cell integrated antennas can be developed based on the transparent DRA, especially towards an array configuration.

3.3 Tilted dielectric resonator antenna made of Alumina

Antennas usually radiate in the direction normal to the ground plane except when end-fire antennas are used, e.g. vivaldi antennas which are well known antennas with radiation in the plane containing the substrate [49, 50]. However not every time, a radiation in the normal to the ground plane (which also is usually the substrate plane) is required or beneficial. Some situations might demand a radiation in any other direction than an end-fire or broadside. For example in MIMO when pattern diversity is used, it could be beneficial to have far field patterns in directions other than the usual broadside for individual or array antennas.

To realize such an antenna element the first choice which seems natural, would be to have a simple patch antenna and then tilting it to the desired angle to have the broadside pointing to the angle of tilt needed. This tilting of the patch antenna will also involve the tilting of the substrate (ground plan) of the whole structure. Such a design will not prove to be of any practical use as the arrays usually consists of a lot of radiating elements and any non-planar geometry realization would be a cumbersome and non-economical task.

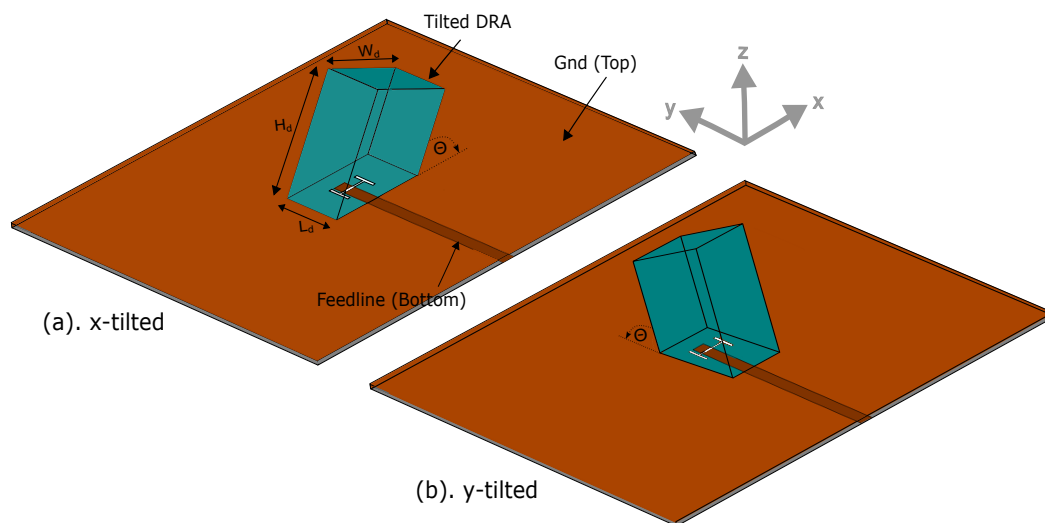


FIGURE 3.49: Tilted dielectric resonator antennas (a) DRA tilted in x direction (b) DRA tilted in y direction.

A tilted beam antenna can be realized by using a tilted dielectric resonator antenna. This concept has been used for the first time to the best of the author's knowledge. Such

an antenna does not require the ground or substrate to be tilted as the tilt is primarily achieved by the tilted DRA itself. The structure of the tilted DRA antenna is shown in Fig. 3.49. A 50Ω microstrip line is present on the bottom side of the substrate. The ground plane is present on the top side of the substrate. An H-shaped slot is also etched in the ground plane. The tilted DRA is placed above the slot on the ground plane. The position of the tilted DRA although is close to being symmetrically placed, it however should be determined from 3D electromagnetic simulations such that best matching is achieved. The construction of the tilted DRA is what also makes this antenna concept novel. The DRA instead of a usual shape is cut in such a way that after placement it makes a tilt angle Θ with that of the substrate plane.

The construction of any DRA is usually done with machining the dielectric material. Construction of complex shapes might not be easy. At first, the tilted DRA seems to be such a complex shape that needs complicated machining steps but in fact it is not. To construct tilted DRA, a usual rectangular shaped DRA is first used and then modified as is shown in Fig. 3.50. An rectangular DRA is a regular shape which is used in practice quite a lot and can be easily machined. At first a rectangular DRA is machined. Then a section of the rectangular DRA is cut by starting from one side at the bottom and meeting the opposite face at some height. This height determines the amount of tilt. Once removed the DRA is placed on the substrate with the face from the cut area which results in a DRA which is tilted.

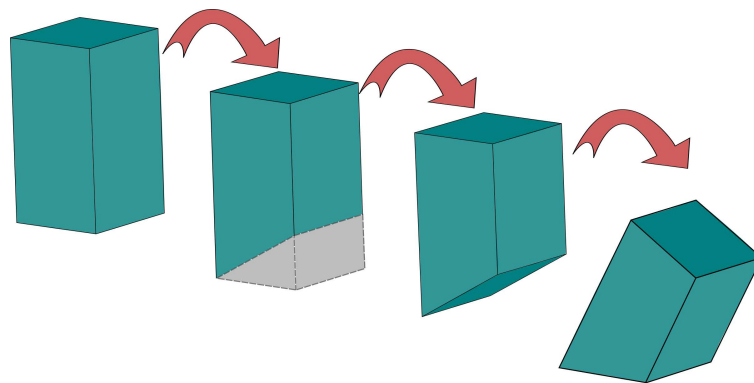


FIGURE 3.50: Making of the tilted DRA from a rectangular DRA.

Fig. 3.49 shows two orientations of the tilted DRA on the substrate. The difference is in the direction of the tilt. The tilted DRA can be tilted in any of the four directions, i.e. forward/backwards ($\pm y$ -direction) and left/right ($\pm x$ -direction) as maybe required. In fact with proper simulations a tilted DRA with a tilt in any direction can be designed.

The DRA height H_d refers to the longer of the two sides of the tilted DRA. This height is actual equal to the initial height of the rectangular DRA before it is cut into a tilted shape. The width and length of the DRA is W_d and L_d respectively. It should be noted

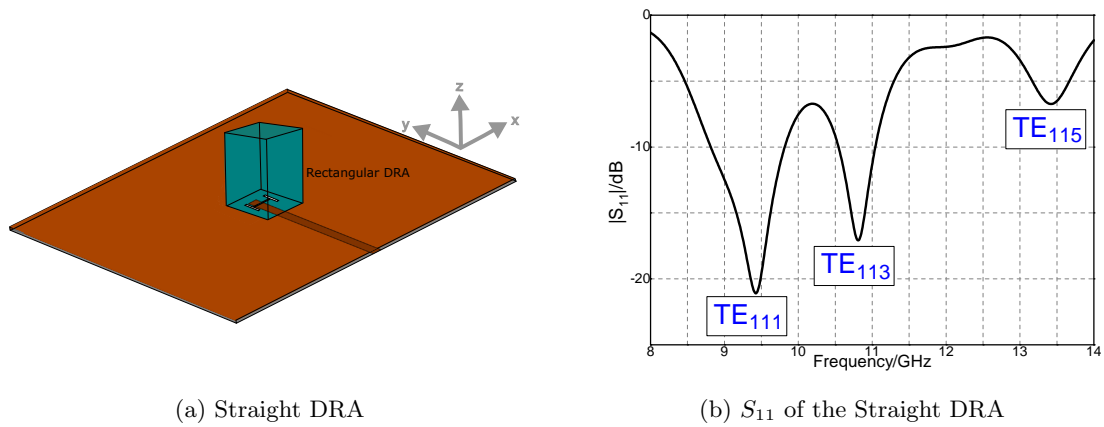


FIGURE 3.51: Reflection loss simulations of the Straight DRA

that this is the area which the tilted DRA physically touches on the substrate. But the actual projected footprint of the tilted DRA on the substrate is in fact more than this area, because of the tilt, which is not the case when a simple straight rectangular DRA is used. The beam tilt is primarily determined by the tilt angle provided that a proper height profile of the DRA is present. This will be discussed in detail with simulation results.

Working principle and simulations of tilted DRA

There are many different parameters that are of importance when designing the tilted DRA. These will be examined in this section. The design frequency is kept to be in the X-band. This choice of frequency is adequate as it is low enough not to present challenges in the fabrication and high enough for practical usage of single DRA antenna element and arrays of such radiating elements.

To start with, a simple rectangular DRA (with no tilt) is simulated, as shown in Fig. 3.51a. The length and width are chosen to be 6 mm and 6.6 mm, while the height is equal to 12 mm. The H-shaped slot length is 2.4 mm with a width of 0.25 mm. The arms of the H-shape have a length of 2 mm. The reflection loss is shown in Fig. 3.51b as obtained from the simulations by adjusting the extending length of the microstrip line to 1.4 mm, which is controlling the matching.

The first three resonances as seen here are of concern, and are shown in Table. 3.6. The first resonance at 9.5 GHz is the fundamental TE_{111} mode (which is usually used when designing rectangular DRA), followed by the higher order modes.

The H-field at these three resonance modes are shown in Fig. 3.52 at their corresponding frequencies in the rectangular DRA. The TE_{111} mode has a half cycle of minima-maxima

TABLE 3.6: Resonating Modes of the straight rectangular DRA ($\epsilon_r = 10$)

Mode	TE_{111}	TE_{113}	TE_{115}
Frequencny [GHz]	9.5	10.8	13.5

pair in the length of the DRA as expected. TE_{113} on the other hand shows 3 such half cycles in the height axis of the rectangular DRA, while 5 cycles of minima-maxima are present for the TE_{115} mode.

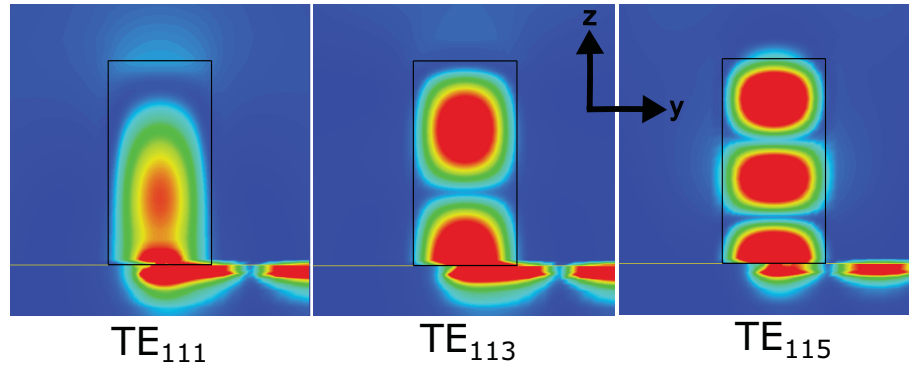


FIGURE 3.52: H-field intensity of three resonance modes of the straight RDRA.

In order to get the tilted DRA from the rectangular DRA, a section has been cut from it as was discussed earlier. The tilted DRA is then optimized in simulations for the targeted frequency. The S_{11} simulation result for a tilted DRA is shown in Fig. 3.53 along with that of rectangular DRA for comparison. This tilted DRA is similar to the rectangular DRA used earlier on one side e.g. $H_d = 12$ mm. The length and width are kept similar to the rectangular DRA as 6 mm and 6.6 mm respectively.

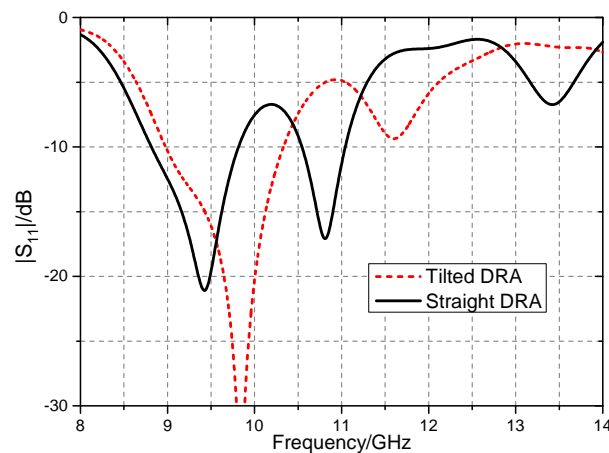


FIGURE 3.53: Input matching of the tilted and straight DRA.

The tilted DRA has the TE_{111} and TE_{113} modes present at 9.8 GHz and 11.6 GHz, respectively. This is shifted towards the upper frequencies when compared with the rectangular DRA. This shift of frequency is understandable, since some portion has

been cut away from the rectangular DRA and less volume will result in higher frequency resonances. Apart from the difference in the S_{11} , the major difference now lies in the direction of the far-field pattern of the DRA.

Fig. 3.54 shows the far-field pattern of the TDRA at 10 GHz. The tilt in the case of the tilted DRA structure is clearly visible. The beam direction will off course be in the broadside for the rectangular DRA.

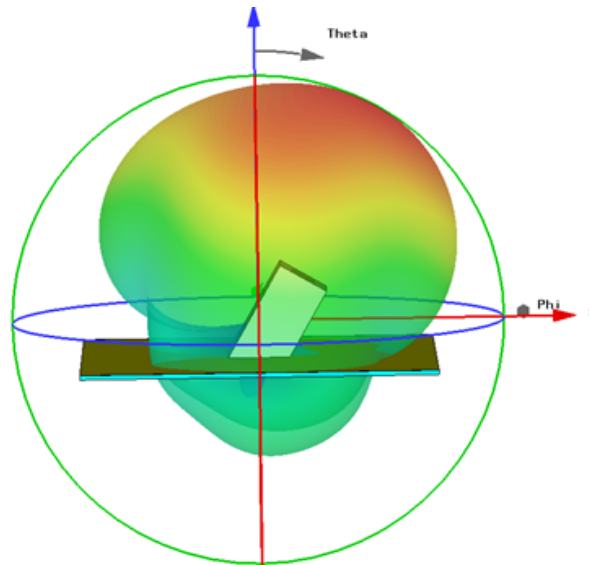


FIGURE 3.54: Far field pattern of the tilted DRA at 10 GHz.

The gain for the tilted DRA as compared to the rectangular DRA is a little less. This is understandable as the tilted DRA volume is less than that of the straight DRA. Hence, a reduction in the gain of the antenna is expected due to the fact that usually more radiating volume means more gain.

The fundamental rule of decreasing size with an increase in the permittivity of the DRA is also valid for this tilted DRA design. The size of the DRA will become an important design decision in the array scenario. The matching bandwidth is decreased dramatically when a higher permittivity value is used.

To see how the tilted far-field is produced, a look at the E-field is helpful. The E-field at 10 GHz is shown in Fig. 3.55 for different phases. The microwave field is clearly traversing the DRA along the tilt. This results in the far-field being tilted as well. The length of the tilted DRA as the field see is important for the tilt. When a smaller DRA is used the field radiates in the broadside direction. Therefore, a minimum critical height of the DRA is required to get the tilted far field. This phenomenon is shown in Fig. 3.56.

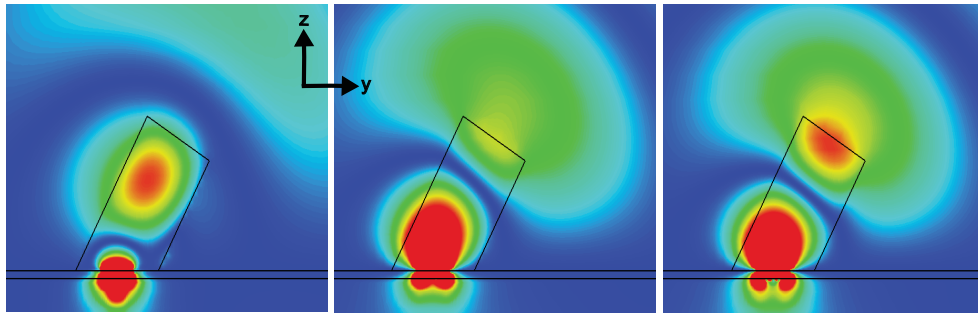


FIGURE 3.55: E-field intensity in the tilted DRA at 10 GHz with 60 degree phase steps.

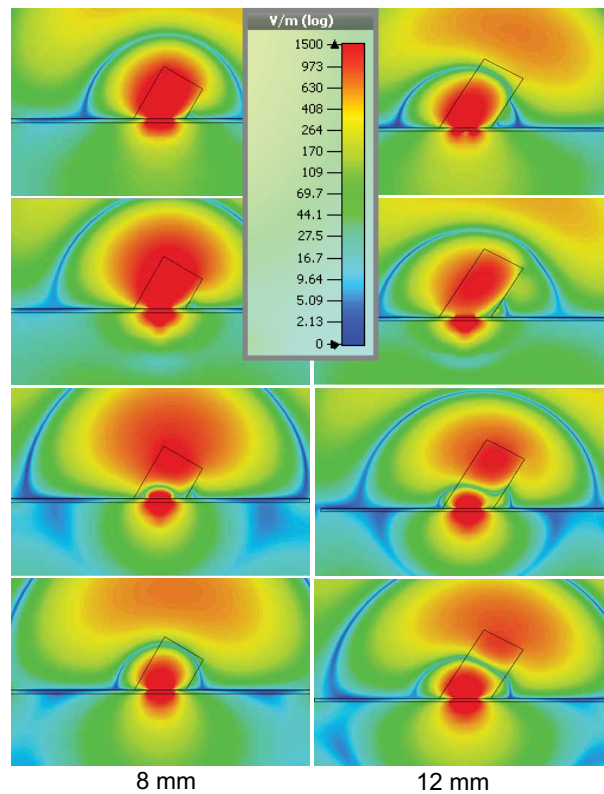


FIGURE 3.56: E-field intensity (with phase step of 30 degrees) in the tilted DRA of height 8 mm (left) and 12 mm (right) at 9.5 GHz.

A certain optimization is required when the tilted DRA dimensions are changed or the tilt angle requirements are different. The table in 3.7 shows the affect of the DRA height on the tilt angle. This tilted DRA can be thought of as a quasi dielectric rod antenna, which still has the resonance characteristic like a normal DRA but also guides the wave along its body (in the direction of the tilt).

Fabrication of the tilted DRA

The permittivity of the DRA was kept to be 9.4. This value is low enough to have a tilted DRA with a band width which is practically useful. This choice of the permittivity value

TABLE 3.7: Far-field pattern direction and TDRA height/angle relation.

DRA Tilt	Freq (GHz)	DRA Height (mm)			
		12	15	18	21
30°	9.5	13°	27°	23°	11°
	10	28°	33°	13°	35°
60°	9.5	3°	16°	26°	32°
	10	18°	27°	34°	68°

is also of practical benefit during the fabrication. Making the tilted DRA from a bulk ceramic material is a machining task which for a sample or prototype demonstration would be quite high. A more practical method was used. The Alumina substrate was laser cut in order to get the tilted DRA with the desired dimensions. Alumina is a low loss substrate which is easily available and widely used at microwave frequencies. The cutting of the Alumina substrate is shown in Fig. 3.57.

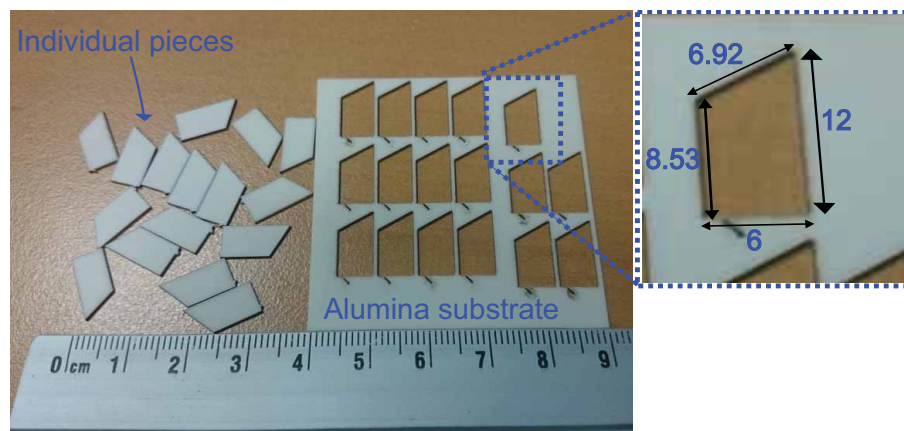


FIGURE 3.57: Alumina substrate of thickness 0.63 mm cut with laser.

The small individual pieces with the appropriate dimensions, for a tilt of 30° were glued together by hand. A commonly available seconds-glue was used. The assembled tilted DRA is shown in Fig. 3.58. The alumina ceramic is a white or off-white in color. The black marks seen on the assembled tilted DRA is due to the burning from the laser cut. The burnt edges were rubbed with a sand paper to clean as much as possible. Fig. 3.58 also shows the fabrication imperfections. The individual pieces shifted a little. The affect of such imperfection will be signified in the measurement discussions. The laser cutting method used in this fabrication can be generally used. This method is specially a low cost solution for DRA fabrication at higher frequencies, e.g. above 60 GHz. At

higher frequency one of the dimension of the DRA would be as small as 2 mm. Such thick substrates are usually available and laser cutting for such substrates are possible. This was confirmed by contacts to some companies e.g. [51]. The price per DRA, even for quantities as low as 100 was found to be in the sub-euro (cents) range.

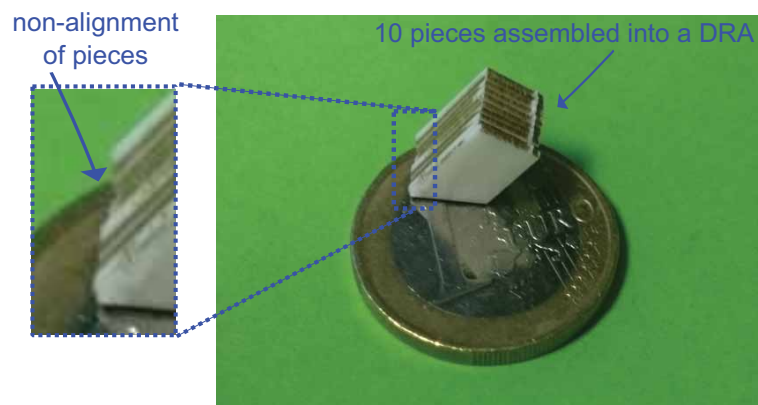


FIGURE 3.58: Assembled tilted DRA from laser cut pieces.

Measurements

The tilted DRA was fabricated on a 40×40 mm substrate with an SMA connector as shown in the Fig. 3.59. The tilted DRA is glued on the top of the substrate. The accurate position was aided by the placement markers around the H-shaped slot. The glue used is the same as was used in the gluing of the pieces to make the tilted DRA. Note the angle between the substrate plane and the tilt which is 30° .

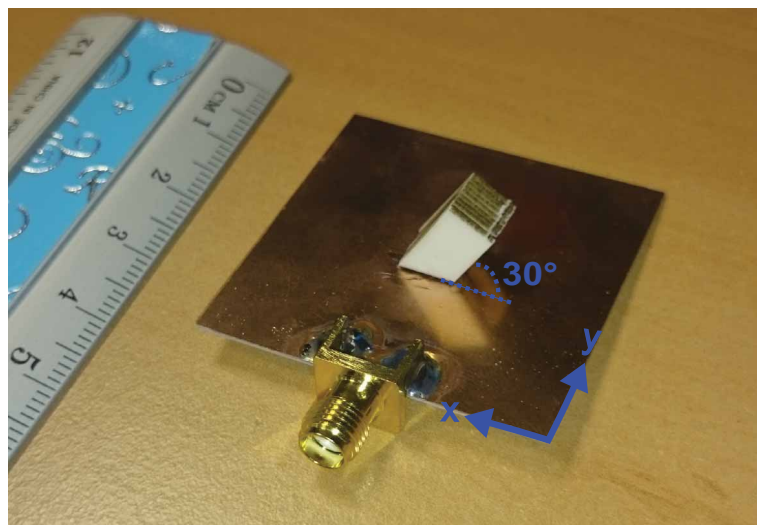


FIGURE 3.59: Fabricated prototype of the tilted DRA.

As was mentioned that the tilt of the tilted DRA can be in either of the four sides. The tilted DRA matching was measured in four tilt configurations which is shown in Fig.

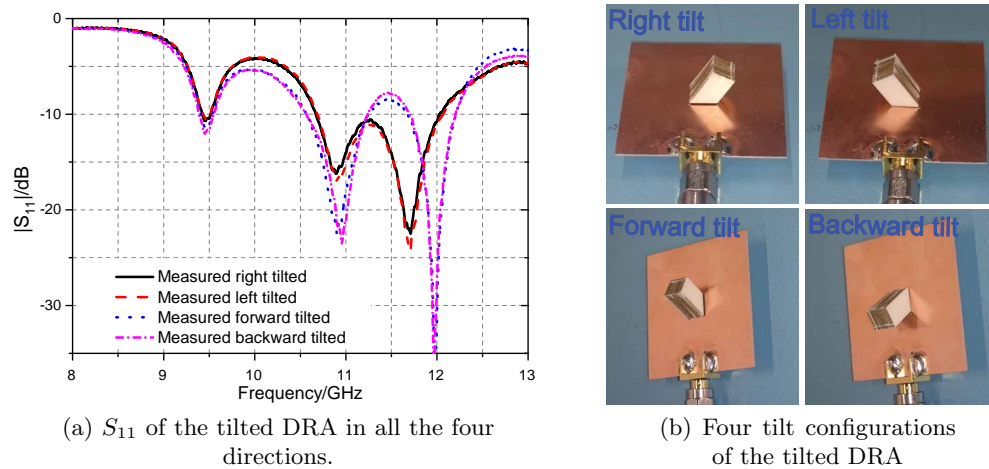


FIGURE 3.60: Measured reflection loss of the tilted DRA in four tilt configurations

3.60. The measurement show that the pairs of the two side way tilts and two back-forth tilts are almost exactly the same. This is because of the symmetry of the structure of slot and microstrip line. The two pairs however, are a little bit different from each other. The forward and backward tilted configuration has a more wider last resonance as compared to the sideways tilt configuration.

The fabricated antenna was measure with a vector network analyzer. The reflection loss data is presented in Fig. 3.61. The S_{11} measure and initially simulated S_{11} has a rather big difference. The shift is almost equal to 1 GHz. This can be explained by the several factors which were involved, that made the fabricated tilted DRA actually different than the ideal simulated design. The burning of the edges by the laser will have an unknown effect. The placement of the tilted DRA on the slot can be shifted in any direction. The most significant of the differences however, appear to be the individual laser cut pieces comprising the tilted DRA. A total of 10 such peaces were used to make the whole tilted DRA structure. All the 10 pieces however, could not be held together perfectly in alignment. This non alignment was both in the X and Z direction (Fig. 3.58).

To check the effect of the non-alignment on the matching of the tilted DRA a re-simulation was performed. This time the non-alignment was incorporated into the design. It was observed that the non-alignment in the X-direction had almost negligible effects. The Z-direction misalignment however, had a great impact on the matching. As some pieces were actually a little above the substrate surface, a value of 0.1 mm of 5 of the random pieces gave a matching almost exactly according to the measurements. A high field exist close the surface of the slot, and hence a change in the material above it even slightly, will effect the matching. This can be avoided when the TDRA will be manufactured more carefully or by fabrication from one bulk material by machine cutting.

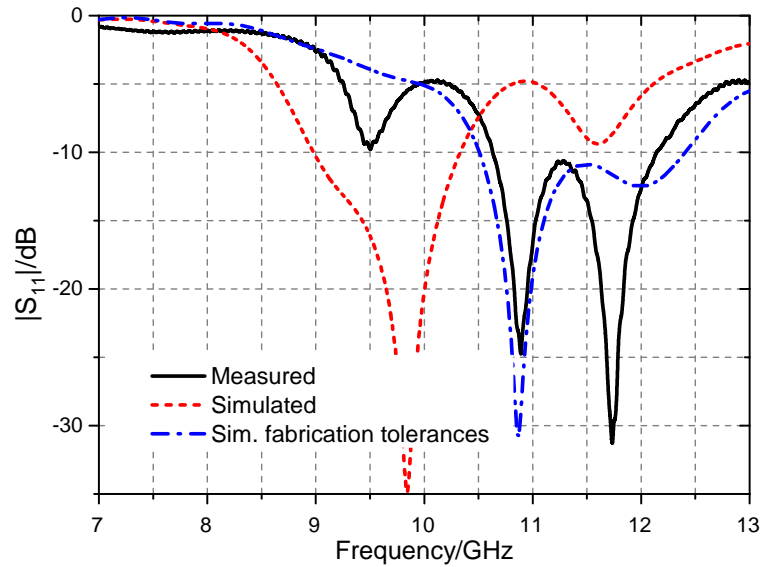


FIGURE 3.61: S_{11} of the fabricated prototype of the tilted DRA. Measured, initial simulation and re-simulated with fabrication tolerances.

TABLE 3.8: Parameters of the 2nd fabricated tilted DRA

L_d	W_d	H_d	L_s	W_s	H_s	Θ
6.35 mm	6.5 mm	12 mm	2.0 mm	0.2 mm	2 mm	30°

This result is shown here as it demonstrates the sensitivity of the tilted DRA for manufacturing tolerances when making it from several pieces. In order to match the measurements with simulations the tilted DRA was again simulated, this time for covering the lower Ku satellite band. The manufacturing was done by using a thicker alumina substrate of 1.27 mm instead of 0.635 mm. Using thicker substrate to cut the individual pieces results in less number of pieces required for making a tilted DRA. This reduces the chances of misalignment during gluing process. The parameters for the second prototype are given in Table 3.8

After fabricating it again, the return loss was found to fit the simulations very well as shown in Fig. 3.62

Far-field measurements

The fabricated antenna was measured in anechoic chamber, the two principal planes of the far-field pattern at 11.2 GHz shown in Fig. 3.63. The measurements agree very well to the simulation data. The H-plane tilt is evident from Fig. 3.64a. Thus it proves the tilted DRA concept for far-field tilting. The value of maximum tilt from measured data is almost 33° . The gain was measured to be 7.1 dBi. The cross polarization levels

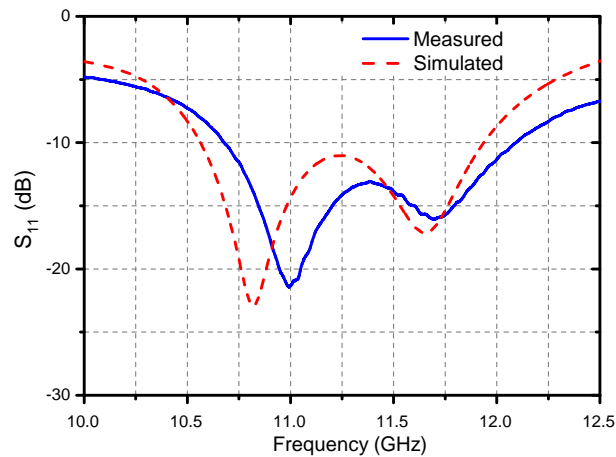


FIGURE 3.62: S_{11} of the second fabricated prototype of the tilted DRA.

were measured to be at least 17 dB which shows the linear operation of the TDRA, as expected.

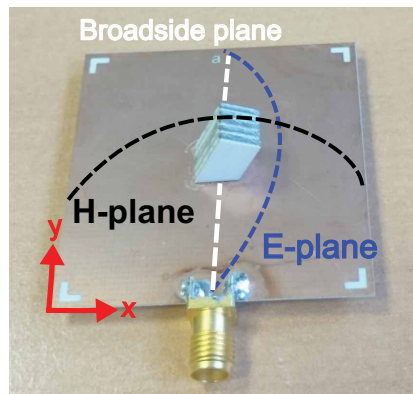


FIGURE 3.63: The principal plane orientation for the tilted DRA.

The measurement of the E-plane as shown in Fig. 3.64b needs to be explained as it is different from the usual measurement for broadside antennas. Due to the tilt in the E-plane of tilted DRA, the measurement of the E-plane requires the alignment of the antenna structure such that the maxima points toward the transmitter. After alignment of the maxima turntable is rotated to measure the E-plane cut. There is discontinuity in the E-plane at around 80° direction. This is due to the measurement setup itself. The metallic fixture which consisted of a coaxial probe came directly between the transmitter and tilted DRA and thus producing some ambiguity in the measurement. The simulated radiation efficiency was above 94% in the whole intended band of operation.

The beam direction as measured from the far-field pattern along with gain is shown in Fig. 3.65. The two quantities vary little over the frequency in the intended band. The tilt of the far-field remains over 27° in the range of 10.6 GHz to 11.8 GHz. The maximum

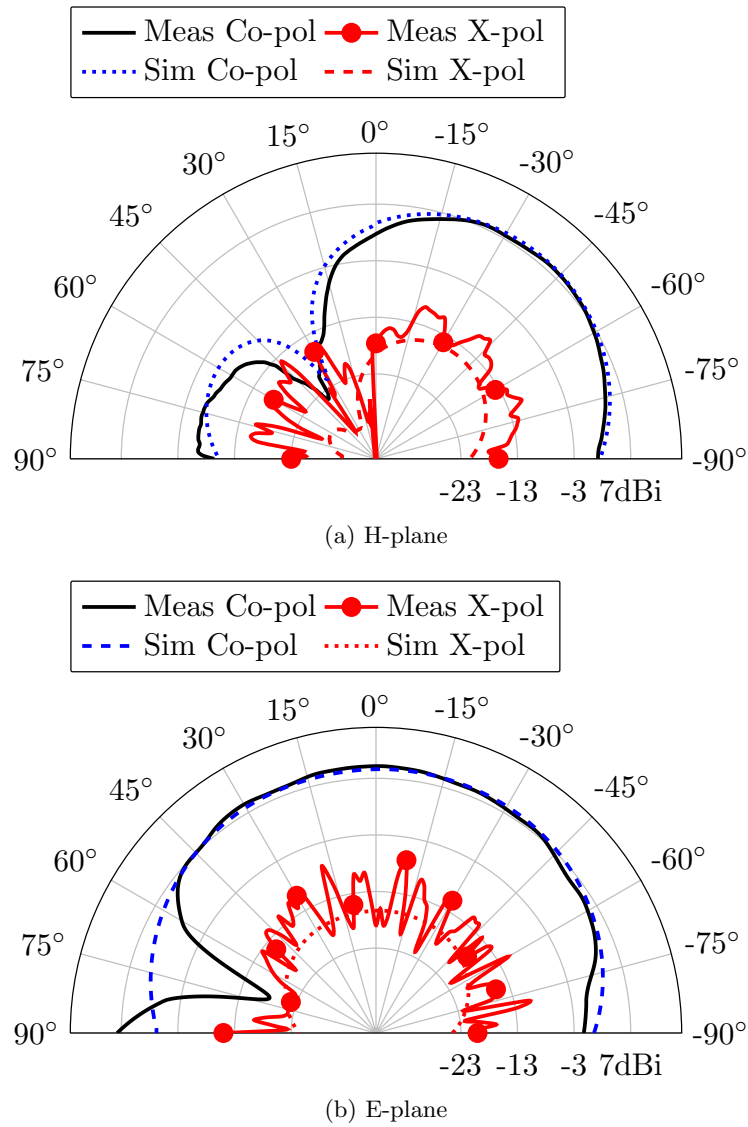


FIGURE 3.64: Measured far field gain pattern of the fabricated tilted DRA

tilt is measured to be 33° at 11.2 GHz. Similarly, the gain also varies very little. The measured gain values remains in the range of almost 6 - 7.5 dBi.

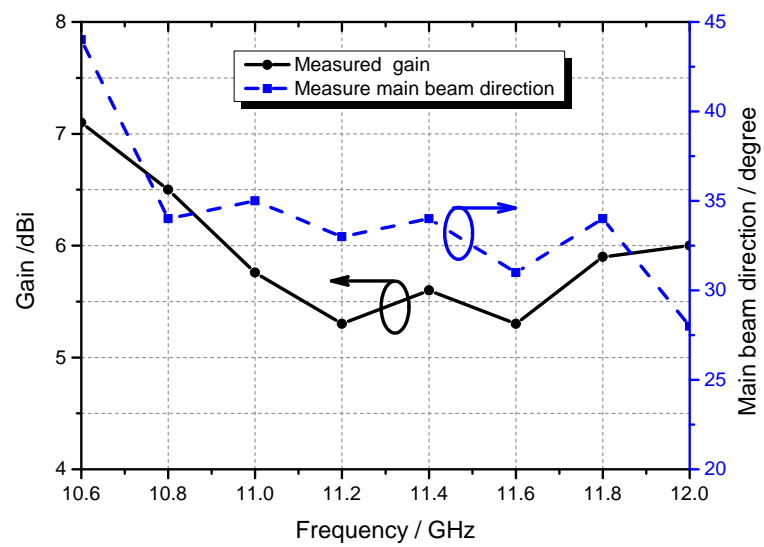


FIGURE 3.65: The measured gain and main beam direction versus frequency.

Chapter 4

Dielectric Resonator Antenna (DRA) based Arrays

An array antenna consists of multiple radiating elements. The grouping of several antenna elements have basically two important advantages: higher directivity and electronic beam-steering capabilities by using phase shifters. The higher directivity is required for communications over long distances or to resolve spatially small areas as higher directivity means smaller beamwidths. The scanning ability of the array comes from the fact that constructive interference of the radiations from the different elements results in enhancing the beam of the array in one particular direction.

A typical corporate feed linear array with 8 elements is shown in Fig. 4.1. The radiating elements have a spacing of d , the main beam direction is θ , and the progressive phase shift between each radiating element is indicated by $\Delta\alpha$

For any array antenna it can be shown that the final far-field pattern is actually

$$E_t(\theta, \phi) = E_e(\theta, \phi) \cdot E_{AF}(\theta, \phi) \quad (4.1)$$

This essentially means that the far-field of an array is actually a multiplication of the element pattern of its radiating elements with another term called Array Factor (AF). The generalized form of the AF for the given array of N element can be written as

$$\sum_{n=1}^N A_n e^{j(n-1)(kdcos\theta + \Delta\alpha)} = \sum_{n=1}^N A_n e^{j(n)\psi} \quad (4.2)$$

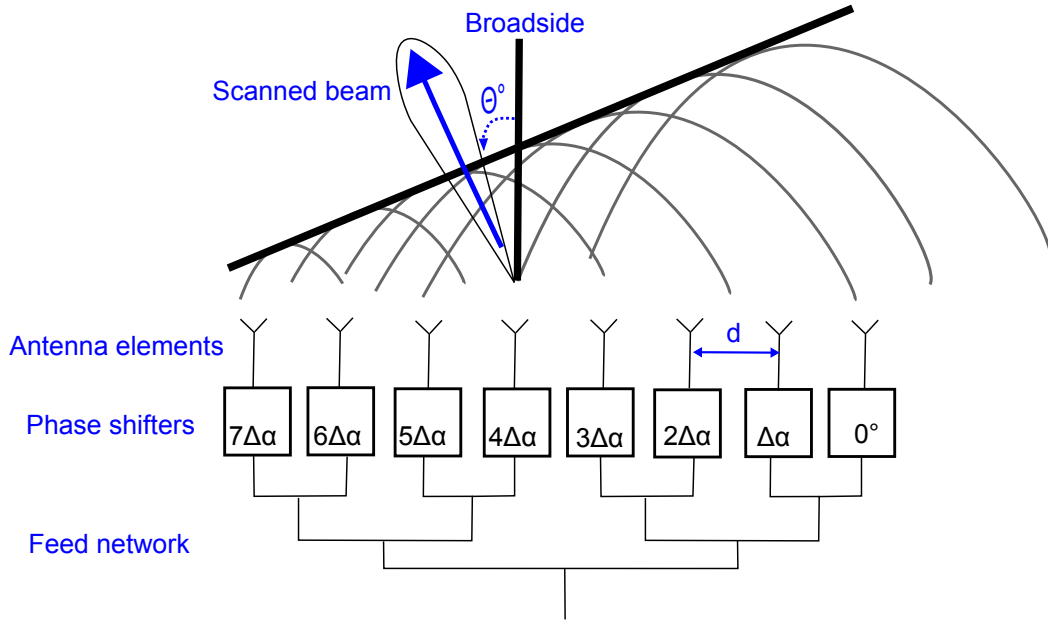


FIGURE 4.1: A linear phased array antenna with 8 elements

The term $\psi = (kdcos\theta + \Delta\alpha)$ is known as the difference in phase between the adjacent elements, with one element chosen as the reference. From equation 4.4 the maximum of the radiation occurs when

$$\psi = (k \cdot d \cos\theta + \Delta\alpha) = 0 \quad (4.3)$$

$$\theta_o = \cos^{-1}\left[-\frac{\alpha}{k \cdot d}\right] \quad (4.4)$$

This implies that the main beam direction is actually dependent on the phase shift between the elements, which is the main principle of the phased array antennas. By controlling $\Delta\alpha$, the beam can be steered to the desired direction. Practically the beam would be required to be scanned in the top hemi-sphere of the plane the antenna lies in.

In the following section a brief discussion of a tilted beam pattern antenna element in connection with array theory will be discussed. The realization of such an antenna element in the form of TDRA was already discussed in the previous chapter.

Array composed of tilted beam elements

To demonstrate the case of tilted beam vs simple broadside, two different element patterns will be used. The two different patterns are shown in Fig. 4.2. The patterns

(dotted line) are in fact simple sin-functions, approximating the far-field pattern of a simple antenna e.g. patch antenna. It is a well known fact that a simple patch antenna has a 3 dB beam width of 70° , which has been taken into consideration for generating the pattern. It was found that a simple sin-function when raised to the power 3, was close enough to model the 70° 3 dB beam width condition. The pattern on the left shows the broadside pattern while on the right are the pattern with a maxima occurring away from the broadside i.e. tilted. The negative values in the element power pattern can be ignored for this simple simulations. The maxima of the tilted pattern (right) for this case is at -30° . This tilt could be at any angle between the broadside and end-fire ($\pm 90^\circ$).

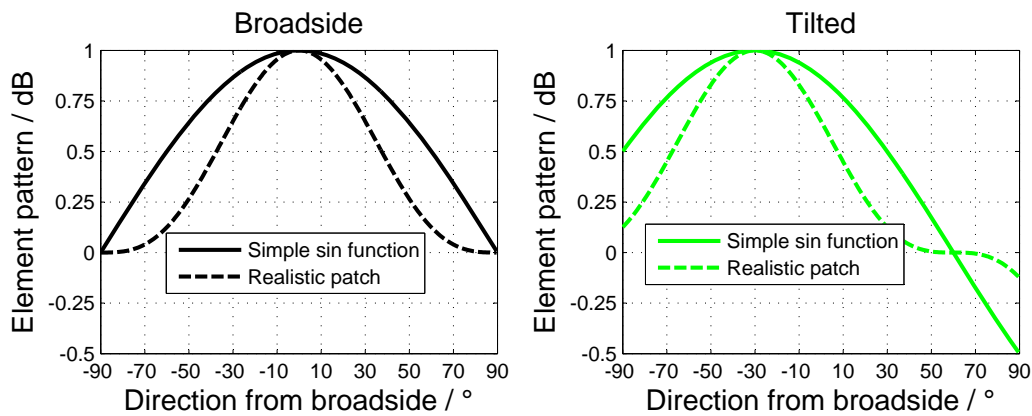


FIGURE 4.2: Normalized element far-field pattern for theoretical sin-functions (solid line) and more realistic function, approximating a patch antenna pattern with 70° 3 - dB beam width (dotted). Left for a simple broadside radiating element and right for tilted radiating element with maxima off-broadside.

The gain plots obtained for an array of eight elements arranged in linear order is shown in Fig. 4.3. The graph on the left shows when the array is scanned in the direction of the element pattern tilt. It can be seen that the tilted elements perform better than the broadside elements. The maxima occurs at the maxima of the tilt of the elements pattern, i.e. -30° . It is actually varying just 2 dB from broadside to -60° . The two curves intersect at -15° , which is exactly the middle of the two maxima of the element patterns i.e. 0° and -30° . The tilted pattern element array thus is able to give a more uniform gain curve with the scanning. The graph on the right shows the scanning in the opposite direction of the element pattern tilt. In this case the tilted elements are always lower in strength than the array with broadside elements, as expected. Therefore, for tilted arrays the gain in the opposite half-elevation plane would be considerably less. The last jump in the graph is just the grating lobe which appears at the higher scanning angle. Hence, such arrays can be used for improvement of gain when the coverage is towards the direction of the tilt of element pattern.

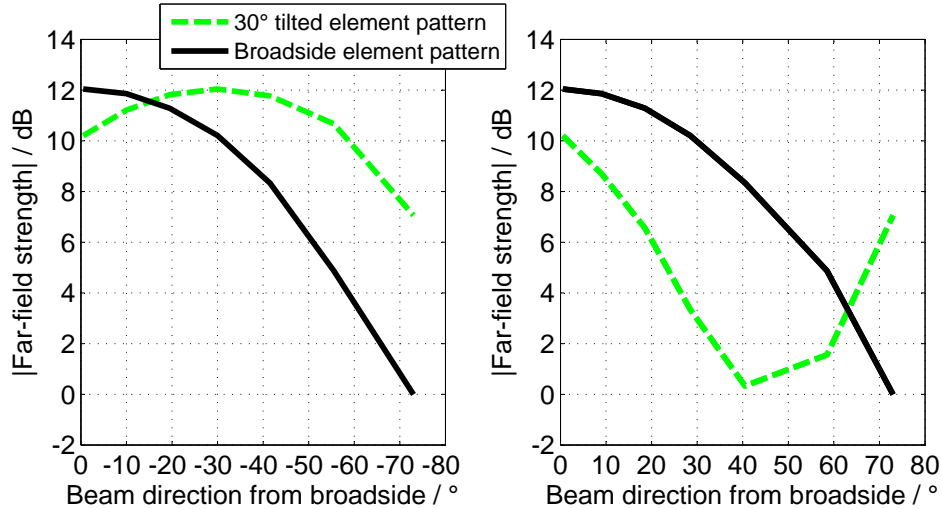


FIGURE 4.3: Far-field strength with beam scanning angle of radiating elements with broadside and tilted pattern. The scanning in the same half-elevation plane as the tilt of the element pattern (left). The scanning in the other half-elevation plane as the tilt of the element pattern (right).

4.1 Fixed beam array based on tilted DRAs

Fixed-beam arrays are needed, when high gain is required, far larger than that of a single antenna element. For scanning phased arrays, the element gain needed are moderate or even low (with wide beamwidth) so that gain reduction off-broadside direction is less severe. The fixed beam arrays on the other hand may benefit from elements with high gain, and thus, achieve the gain with lesser elements [52]. The tilted DRA element presented in the former section can be tailored to fit any fixed beam array. The main benefit using the tilted DRA as the radiating elements for fixed-beam array is that the gain can be improved in the desired off-broadside direction.

For a proof-of-concept, a fixed beam array demonstrator has been designed based on eight 30°-tilted elements described in the previous chapter, however, with a set of three different feeding network, using different delay lines for different phases at the DRAs to provide a progressive phase shift of 0°, 90° and 180° between the radiating elements. These different phase progression along the array shifts the main beam in space in three different directions of 0°, about 30° and above 60°. The design of the array is shown in Fig. 4.4. It consists of a 1×8 corporate feeding network. The ground plane contains the H-shaped slot. The distance between the antenna elements was kept at 14 mm, which is equal to 0.51λ at 11 GHz.

Then, three sets of PCBs with different feeding networks are fabricated, where same eight tilted DRAs are glued on top, in turn one after the other, so that to avoid differences from the radiating elements. This setup is thus simulating a beam steering array. However,

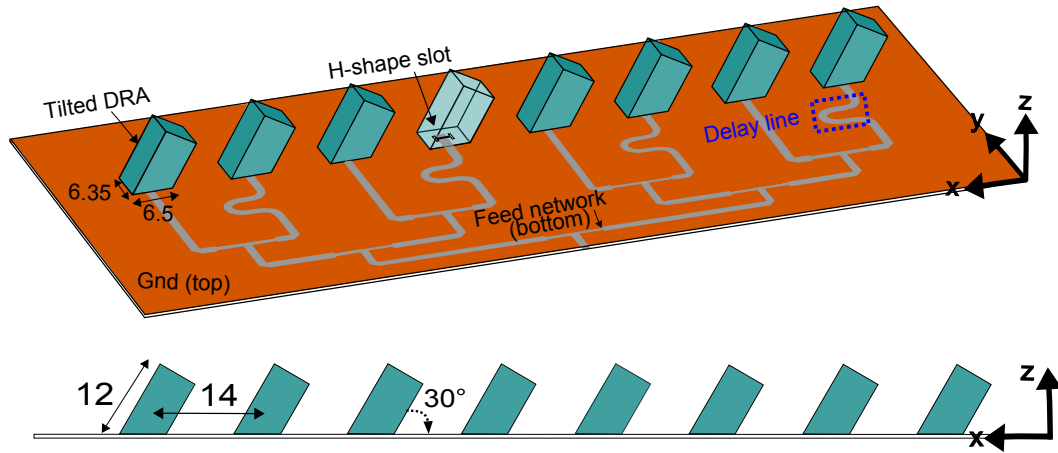


FIGURE 4.4: The 1×8 fixed tilted beam array using, tilted DRA as radiating elements.

the dissimilarity in the gluing and positioning of the tilted DRAs could still create some differences (apart from the feed network) among the three sets of arrays. The top side of one of the array is shown in Fig. 4.5.

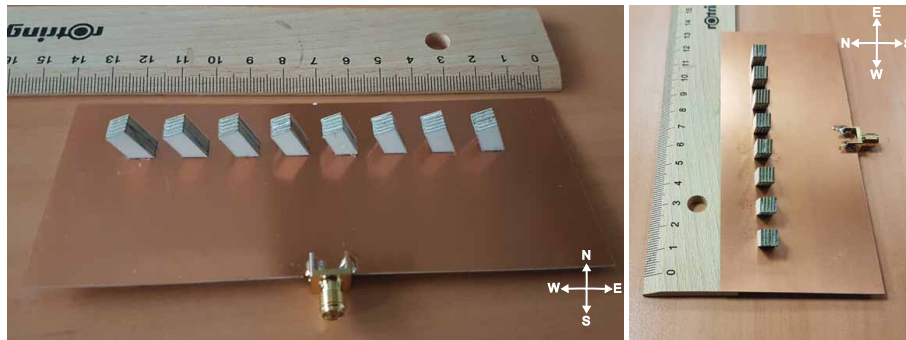


FIGURE 4.5: The fabricated 1×8 fixed beam array consisting of tilted DRA made of alumina as radiating elements.

The bottom side of the arrays containing the corporate feed network is shown in Fig. 4.6. The feed network has 8 transmission lines. For the case of the broadside beam, the feeding network is simple without any delay line. Subfigure (3) shows the feeding network for approximate beam direction of 30° . This feeding network has the longest delay lines, since 6 of the 8 lines contain delay lines (longer lines). This is important to note, as it is a comparison, and hence, feeding network losses must be compensated when measuring the gain. This will be discussed again when the gain of the arrays is compared. Subfigure (2) shows a feeding network for a main beam shift to be at least 60° . An elevation angle of about 60° is usually the maximum scanning angle necessary to be covered in most applications.

The reflection loss measured for the three fixed arrays is shown in Fig. 4.7. It can be seen that the S_{11} for the case of a main beam direction of 30° is the best. This is due to the fact that the main beam is steered exactly towards the direction, where

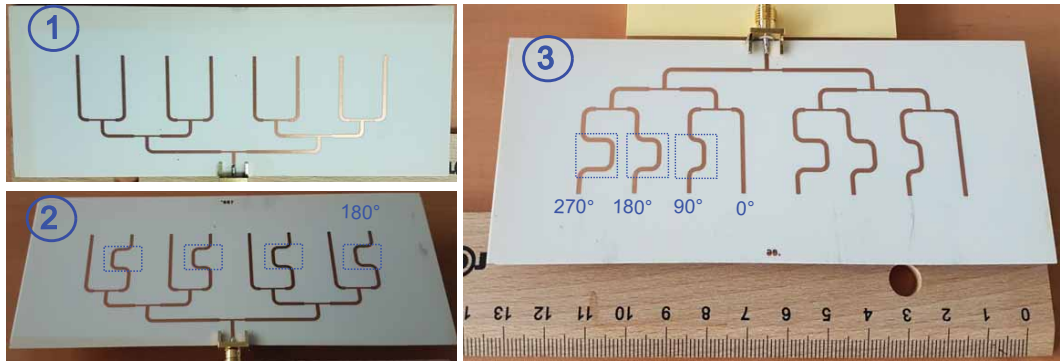


FIGURE 4.6: ① : Feed network for broadside with no delay line (progressive phase shift) ② : Feed network with delay line of 180° for 60° main beam ③ : Feed network with delay line giving 90° delay for 30° main beam.

all the individual tilted antenna elements are radiating. Hence, the radiation is best and good matching can be achieved. It is similar to the matching results, at broadside, when broadside elements are used and as the beam steers away from the broadside the matching becomes worse. In this case, instead of broadside, the good matching performances is provided in the direction of radiation of the tilted DRAs, which is close to 30° . The ripples in all the three graphs is because of the array effect.

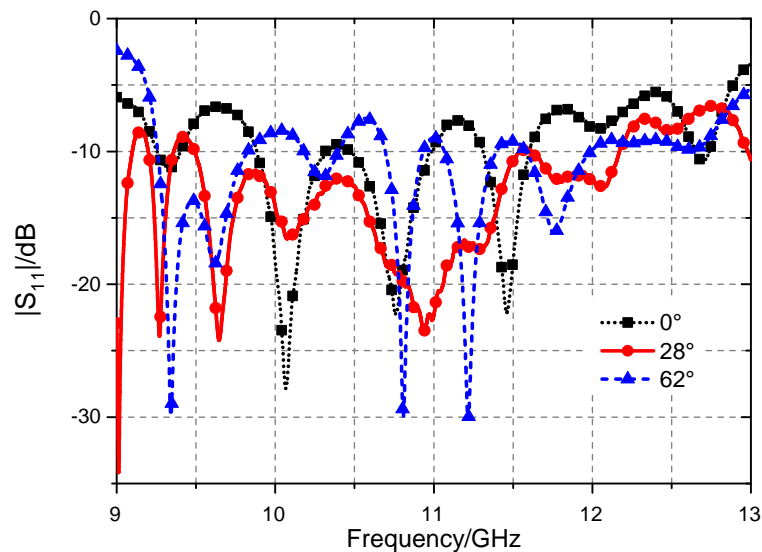


FIGURE 4.7: Reflection loss measurements of the fabricated fixed beam array, consisting of tilted DRA as radiating elements.

Next, the far-field of the three fabricated arrays is measured in an anechoic chamber. The co- and cross-polarization, E and H planes of the broadside array, 30° beam array and 60° beam array are shown in Fig. 4.8 , 4.9 and 4.10 respectively, at 11 GHz. The beam directions of the three arrays indeed shows the beams at 0° , 30° and 65° direction as expected.

The cross-polarization levels of the three arrays in the main beam direction is almost 20 dB. Thus the arrays are linearly polarized. The E-plane measurements of the arrays is performed by first, rotating the arrays 90° (as done for any broadside antenna) followed by tilting arrays further such that the maxima of the array points towards the transmitter. Therefore, the E-plane is always depicted such that the maxima is at the 0° direction. The little dip as seen in the E-plane measurement close to the -70° direction is due to measurement setup fixture. There was a test fixture with a coaxial cable, which interfered with radiation from the transmitter in that direction.

The H-plane of the 65° scanned beam shows a comparable gain. But there appears a grating lobe in the opposite direction as well. The grating lobe is still 7 dB less than the main beam. The grating lobe appearance is governed by the simple equation

$$\frac{d}{\lambda} \leq \frac{1}{1 + \sin\theta_{max}}, \quad (4.5)$$

where λ is the wavelength, d is the spacing between the radiating elements and θ is the steered main beam direction. In the case of the fabricated array d is 14 mm, which is 0.51λ at 11 GHz. Thus theoretically, the grating lobe should not appear until the beam is steered over 70°. It should be noted that equation 4.5 is valid only when all the radiating elements are considered as independent radiation sources causing no mutual coupling. But this is not the case in practical implementations. Therefore, the grating lobe appears sooner than expected as in theory.

The most important parameter to compare the three arrays is the gain, which can be easily seen from the tilted beam performances in the H-planes of the three arrays according to Fig. 4.11. The beams as expected to become wider when scanned away from the broadside direction. The gain levels, however, remain more or less constant. Such a performance will not be possible with planar array, e.g consisting of patch antenna elements. To achieve such result, a conformal (e.g semi-circular shaped) arrays must be used. But in this case, the substrate was planar and still a more uniform gain was achieved within the 0° to 65° scanning range.

The gain of all three array configurations are plotted in the frequency range of 10.6 to 11.4 GHz in Fig. 4.12. The gain of the broadside and 30° configuration are measured to be more close to each other, while the gain of the 65° scanned beam is on average a bit better. The reasons for this could be the fabrication differences. The 65° configuration was measured first, which means the tilted DRA elements were then removed and glued to the other two arrays. Some of the glue remained on the tilted DRA elements. And hence, it is expected to introduce some losses. The substrates for the three arrays were

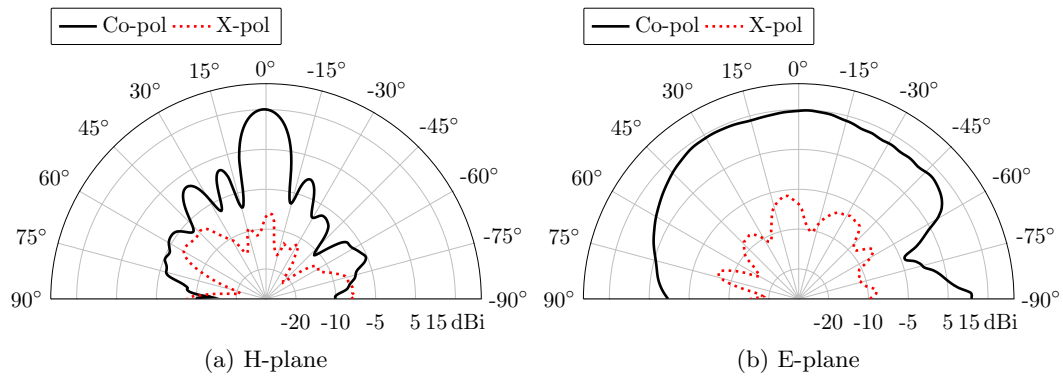


FIGURE 4.8: Antenna pattern measured in the two principal planes of the fabricated 1×8 array prototype with main beam direction at 0° .

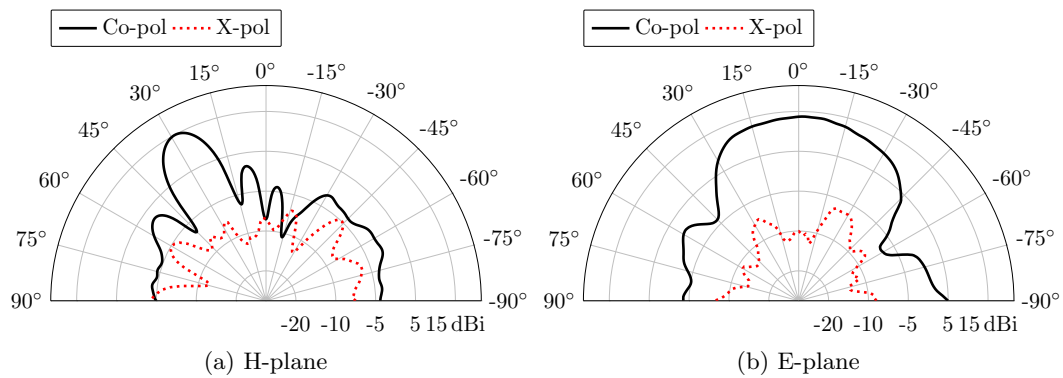


FIGURE 4.9: Antenna pattern measured in the two principal planes of the fabricated 1×8 array prototype with main beam direction at 30° .

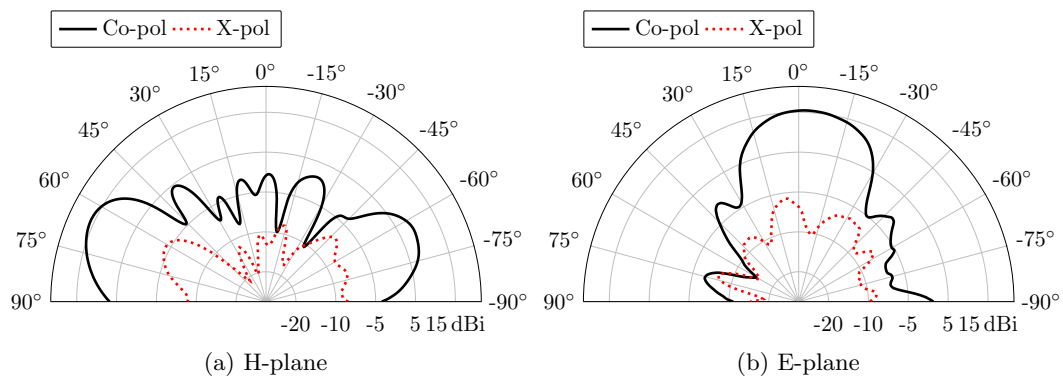


FIGURE 4.10: Antenna pattern measured in the two principal planes of the fabricated 1×8 array prototype with main beam direction at 65° .

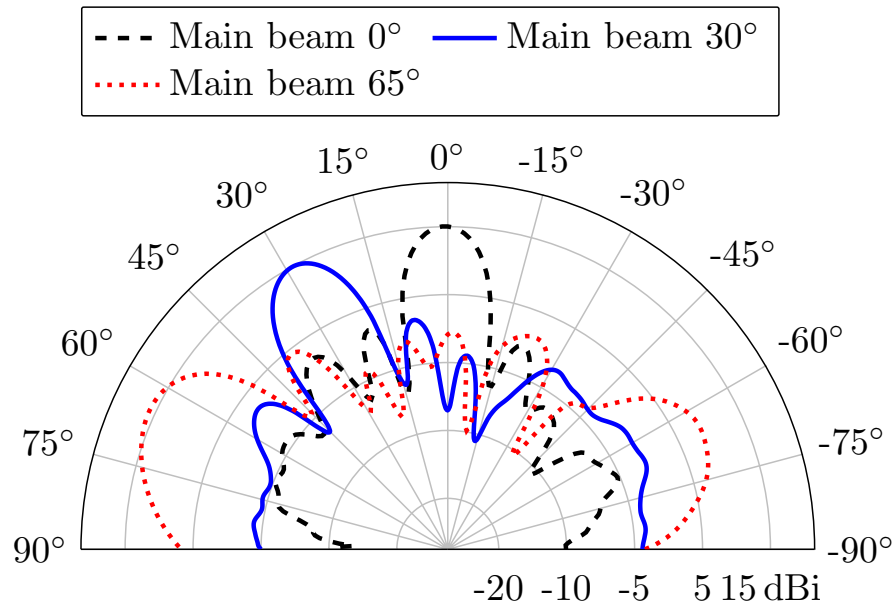


FIGURE 4.11: Antenna pattern of the fabricated fixed beam array, consisting of tilted DRA as radiating elements.

also different with different connectors, which can result in some small degradation from one to the other.

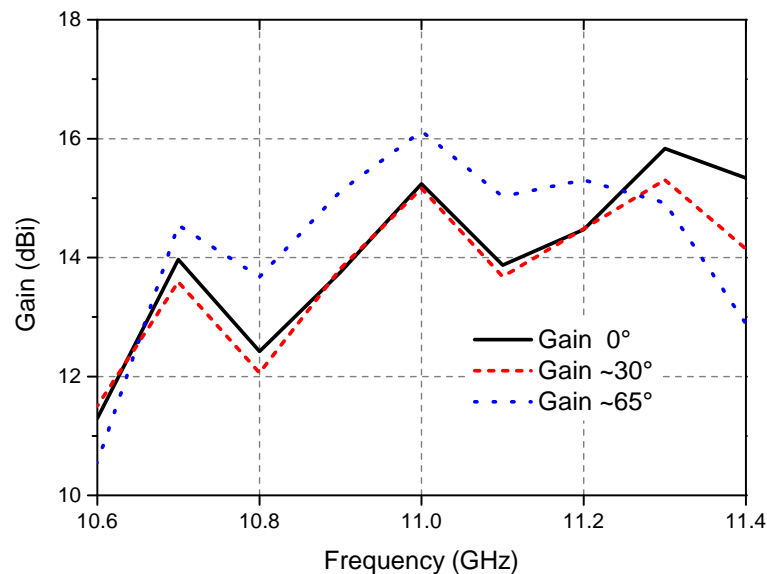


FIGURE 4.12: Measured gain of the three fabricated fixed beam arrays vs frequency.

Fig. 4.13 shows the beam direction in the frequency range of 10.6 to 11.4 GHz. It shows almost constant behavior. Some anomalies can be attributed to the measurement accuracy. At the same time, the complex interaction of the tilted DRAs mutual coupling would result in some gain and direction unexpected values, which the simulation usually can not predict. The coupling within the feed network also has some degradation effect. There was some magnitude fluctuation in the different branches of the feed network.

This fluctuation is shown in Fig. 4.15. The fluctuation is frequency dependent, and therefore, some gain fluctuation also results as was seen in the measurements. For a more accurate comparison, low mutual coupling lines must be used, e.g. by fencing the branches with grounded Vias.

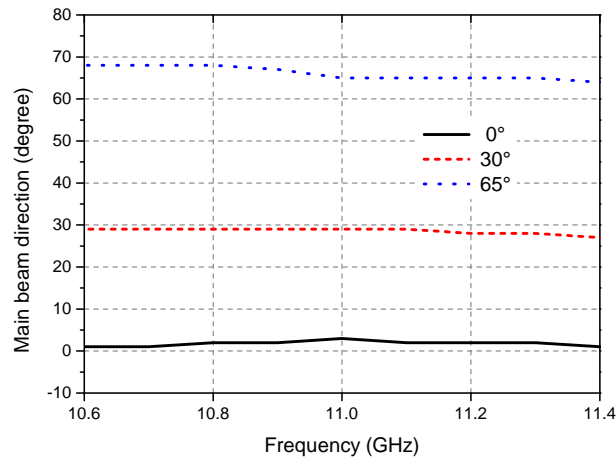


FIGURE 4.13: Measured main beam direction of the three fabricated fixed beam arrays vs frequency.

Nonetheless, it is interesting to note the maximum absolute difference in the gain. The gain reduction for 30° and 65° beams as compared to that of the broadside gain as plotted in Fig. 4.14. It can be noted that the difference of gain remains close to 1 dB. The gain degradation for scanning beam is specified by the equation

$$G_{loss} \approx (\cos\theta)^\alpha, \quad (4.6)$$

where θ is the scanned beam direction and α is a factor depending on the geometry of the array and radiating elements. A typical value of α is 1.5. The gain loss from equation 4.6 will be 1 dB and 5.6 dB for the 30° and 65° fixed beam array, respectively. But due to the tilted beam of the radiating elements it bound in the range close to 1 dB. Such a low scanning gain loss is almost impossible to achieve with the usual patch antenna array with planar (not conformal) substrate.

4.2 Beam-steering DRA based arrays

There are three main components of any phased array antenna as shown in Fig. 4.1, the radiating elements, the phase shifters for delay, and the feeding network. Out of these three main parts, phase shifters are usually the most expensive and complex component,

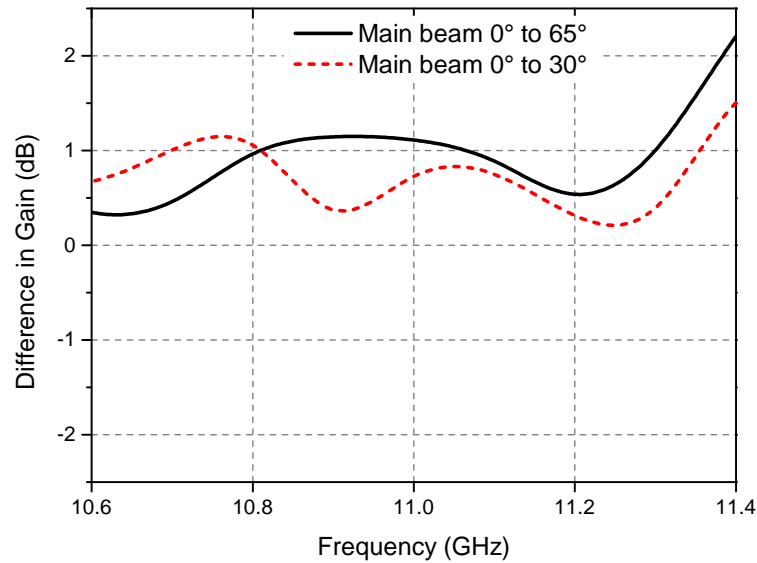


FIGURE 4.14: The gain difference of the fixed beam fabricated prototype between the broadside to 30° and broadside to 65° .

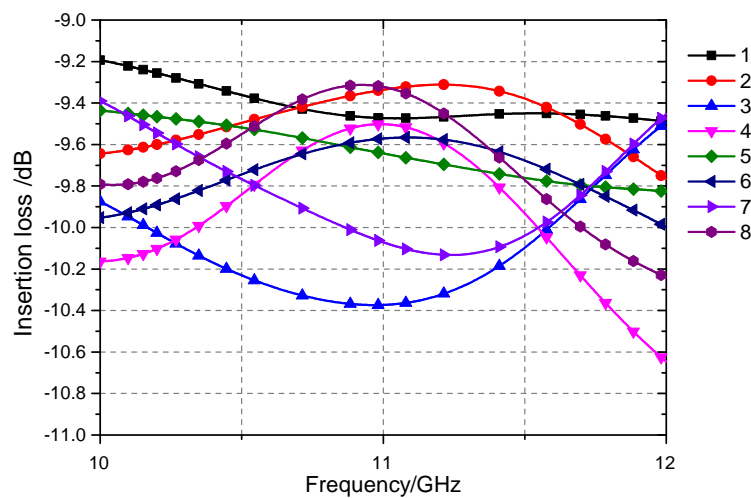


FIGURE 4.15: The simulated insertion loss at the 8 branches of the feed network for the 30° fixed beam array.

which dictates the cost and performance of a beam-steering array. Phase shifters are required to have a maximum phase shift capability (maximum is 360°), low insertion loss, enough bandwidth, high RF power handling, very low power consumption, negligible amplitude variations, low complexity of control signal and small size (to fit between the array elements) [53]. The control complexity should be as low as possible. One control signal is preferred. Moreover, the amplitude variations vs. phase control should be small. All those constraints make the design of integrated phase shifters a challenging task.

There are four main technologies used for phase shifters based on semiconductor, microelectromechanical systems (MEMS), ferrite and tunable materials. The phased arrays

demonstrators presented in this chapter utilizes the passive phase shifter technology based on tunable material which change its permittivity with an applied voltage. The first prototype utilizes a Liquid Crystal (LC) based phased shifter, while the second one uses Barium-strontium-Titanate (BST) based phase shifter technology. The basics of both technologies will be explained here for the purpose of completeness and understanding its principles. The reader is referred to [54] and [55] for a detailed knowledge of LC and [56], [57] and [58] for BST. In the following section, phased array antennas in the context of the DRA radiating elements will be discussed.

Comparison of patch antennas and DRAs as radiating elements in phased arrays

Patch antennas have been used extensively as radiating element in phased arrays due to their ease of fabrication, cost and low profile. Phased arrays with microstrip patch antenna elements have been shown to effectively steer the beam from -50° to $+50^\circ$ with a reduction of 5 to 6 dB in the gain [59]. In [60] the authors have reported an LC based beam steering array with microstrip patch elements used as radiators. It has been discussed that at wide scan angles (more than 40°) the gain reduces dramatically. Surface waves cause extra losses and also mutual coupling when planar structures are used [61]. Extra effort, e.g. using electromagnetic band gap structures, must be done to mitigate the effects of the surface waves [62].

Alternatively DRA is will have no surface waves when used without a substrate or thin substrate. It also offers other attractive features of better bandwidth, low loss and flexibility of feeding [63]. DRA uses high permittivity material where the electromagnetic energy is contained in the DRA. Therefore, DRAs need no or thin substrate to achieve desirable bandwidths. While on the other hand, patch antennas need thick or lower permittivity substrate for achieving any practically acceptable bandwidths. This means that with DRAs in array configuration, one can use thinner substrates. This will result in better efficiencies and higher scan angles due to less effects of substrate waves. Phased arrays consisting of DRAs as the radiating elements have already been demonstrated in [64] with 320 radiating elements. In [65] the authors have concluded that at 25 GHz DRA arrays out performed the patch arrays in both gain and bandwidth. The performance difference gap is expected to increase further as patch elements will have even more conductor losses at higher frequencies. The comparison of a patch and DRA in the context of usage as array elements will be discussed here with respect to two main phenomenon: Surface waves and mutual coupling.

Surface or substrate waves

Narrow impedance bandwidth, low gain and surface wave losses are the most notable of these limitations [66]. The unwanted substrate waves (also sometimes referred to as surface waves) is one of the main performance hindrance for patch antennas. These waves exist when ever there is a conductor-substrate interface. A simple illustration of surface waves generated by a patch antenna is shown in Fig. 4.16. For an angle $\theta_c = \sin^{-1}\left(\frac{1}{\sqrt{\epsilon_r}}\right)$ the waves are trapped inside the substrate, which when radiated at the end of the substrate cause degradation in the far-field pattern [67]. Such waves cause mutual coupling when there are other radiating elements in the vicinity. For arrays, this means also some effect on the side lobe levels and active element impedance.

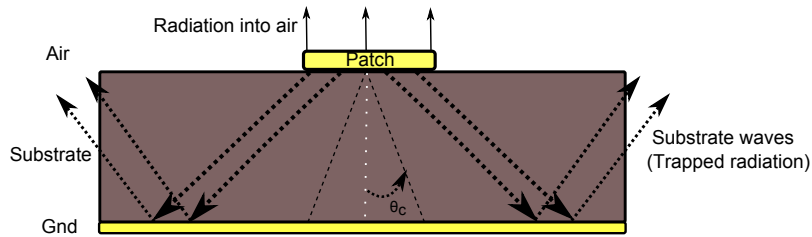


FIGURE 4.16: Simple illustration of substrate wave phenomenon in a patch antenna on a grounded substrate.

With n as the mode index and c as speed of light, the cutoff frequency in the substrate of height h is given by [68]

$$f_c = \frac{n \cdot c}{4h\sqrt{\epsilon_r - 1}} \quad (4.7)$$

Both TE and TM surface waves can exist in a substrate with a ground plane. The first TM_0 mode unfortunately has no lower cutoff frequency. Hence, it will always exist in the grounded substrate. As the substrate becomes electrically large or the dielectric constant of the substrate become large, the cut off frequency is lowered, i.e. more modes are excited in thick substrates, and hence, amount of energy lost due to the surface waves increase.

In [69], simple closed form formulas were derived for the radiation efficiency of rectangular patch antennas which is define as

$$e_r = \frac{P_r^h}{P_r^h + P_{SW}^h} \quad (4.8)$$

where the superscript h refers to Hertzian dipole. P_r^h means the radiated power while P_{SW}^h means the power in the surface waves. The formulas were actually derived for

Hertzian dipole placed over a ground substrate with relative permittivity and permeability of ϵ_r and μ_r and height h . The formulas were then adopted for the rectangular patch antenna by considering the patch as consisting of many small dipoles and integrating the surface current.

The radiated power P_r is given by

$$P_r^h \simeq \frac{1}{\lambda_0^2} (k_0 h) \left[80\pi^2 \mu_{r2} \left(1 - \frac{1}{n^2} + \frac{0.4}{n^4} \right) \right], \quad (4.9)$$

while P_{SW}^h is given by

$$P_{SW}^h \sim \frac{1}{\lambda_0^2} (k_0 h)^3 \left[60\pi^3 \mu_{r3} \left(1 - \frac{1}{n^2} \right)^3 \right]. \quad (4.10)$$

The parameter $n = \sqrt{\epsilon_r \mu_r}$ is a more generalized substrate as it contains both the permittivity and permeability terms. The most important parameters to note from equation 4.10 is that the surface wave power increase with the height of the substrate and relative permittivity (or permeability).

Fig. 4.17 shows how the bandwidth and surface wave loss of the patch antenna vary with increasing substrate thickness. The bandwidth increases as the substrate height is increased but at the same time surface wave losses increase too. This is a dilemma which the patch antennas suffer from, as higher bandwidth is required with low surface wave loss.

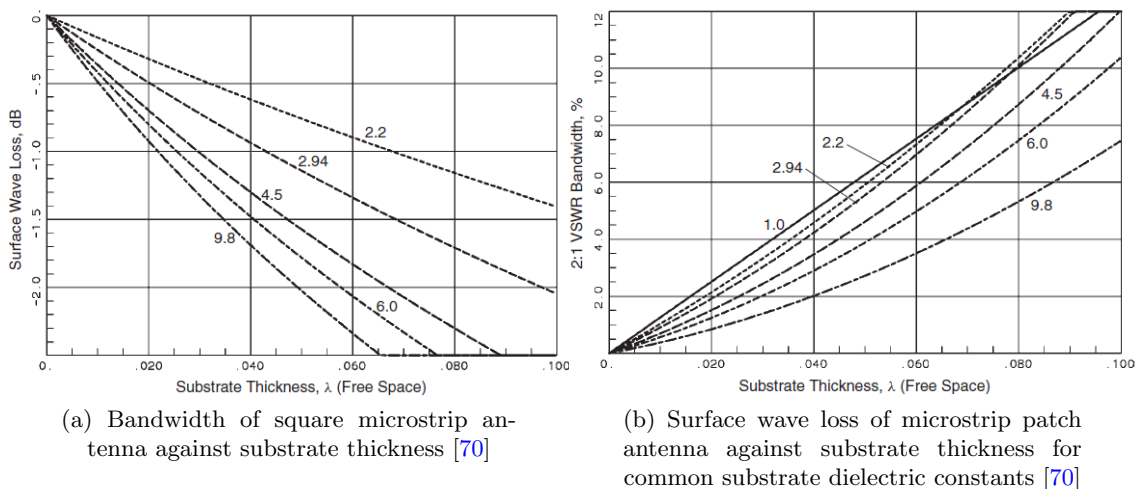


FIGURE 4.17: Microstrip patch antenna bandwidth and surface wave loss versus substrate thickness

This is one main reason why DRA antennas will be beneficial in both, single antenna and array antenna configuration. For the case of single antenna, this is not a critical issue as there are some remedies to get rid of the surface wave problem. The simplest solution is to remove the substrate which is unnecessary called partial substrate removal as done in [71]. Another difficult but more beneficial method is to actually remove the substrate below the patch [72]. Another reduced surface wave antenna was presented in [73] which introduce a cavity filled with specific permittivity material such that the dominant TM_0 mode is suppressed. Placing a superstrate above the patch has also been shown to suppress the radiation in the substrate [74]. Another more general approach is to use some electromagnetic band gap structures on the substrate of the patch [75]. All these methods however come at the cost of either complexity, size increasing of the patch, bandwidth reduction or cost. Also these methods are more suited for a single antenna. But almost all of the methods mentioned are not suited for an array configuration.

This is where DRAs can be used to replace the patch antenna and corresponding arrays. Since a DRA does not practically require a substrate above the ground plane, it can be designed with no or very thin substrate such that no substrate waves exist at all. This in turn means less mutual coupling for the same or more bandwidth as compared to patch antennas. In the master thesis [76], DRA arrays were practically designed without any top substrate, i.e. pure metal plate. Such design is not possible for patch antennas, as they always require a dielectric for support. One can at the same time argue, for using foam substrates with very low permittivity (close to air), but in such scenarios the size of the patch antenna increases, which again is not practical for array configurations.

Mutual coupling

A very important criteria for a radiating element in an array configuration is the mutual coupling between the adjacent elements. A DRA will usually be more compact because of high permittivity material. From this, it would seem that a DRA would have less mutual coupling between them. This argument however, ignores the fact that as the DRA size in lateral plane reduced, at the same time the height of the DRA is introduced (which is not the case for patch antennas). In fact, in some studies the mutual coupling is found to be more for DRAs instead of patch antennas [77]. To investigate the mutual coupling, simulations were performed between two patch and two DRA elements at 12 GHz on the 0.81 mm substrate with $\epsilon_r = 3.55$.

The mutual coupling result is shown in Fig. 4.18. It was observed that there was no advantage of using DRA over a patch antenna in terms of the mutual coupling. The

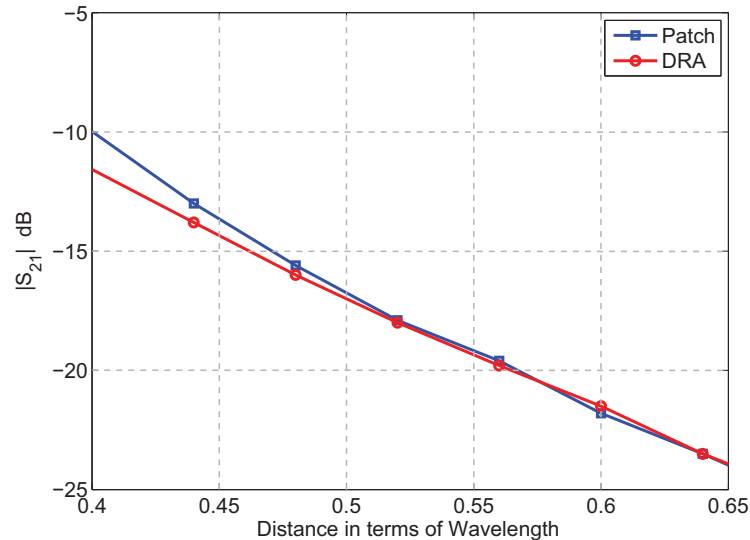


FIGURE 4.18: Mutual coupling between side by side (E-plane) placed patches and DRAs.

configuration was simple slot fed patch and DRA. Many different configurations, e.g. direct microstrip coupling and different substrate heights also had similar results.

A final comparison of patch and DRA as radiating element in a phased (or fixed beam) array can be concluded as follows

- DRAs do not offer any significant advantage in terms of mutual coupling.
- DRA arrays offer higher bandwidth than patch antenna arrays without the necessity of thick substrate.
- A DRA array can be constructed without any substrate at all, i.e. above a metallic ground plane. This will be beneficial for eliminating or at least suppressing substrate waves.
- A DRA array will perform better in comparison with patch antenna arrays as the frequency raises because of no conduction losses.
- Patch antenna arrays still offer a more cost effective and already matured process for manufacturing. DRA arrays needs complex machining. The placement of the DRA array elements is also a major problem, since accurate and cost effective manufacturing (especially at higher frequencies) is still a challenge for mass production. Some plastic ceramics [78] in this regard might be suitable to exploit a plastic injection molding technique for cost-effective manufacturing of DRAs.

4.2.1 Liquid Crystal based phased array

Liquid crystal has a unique property, since microwave losses decrease as frequency increase. In contrast, at higher frequencies, the usual patch antennas would have increasing losses due to conductor. Therefore, combination of LC material with DRAs is a more feasible combination for higher frequencies. Hence, a prototype was fabricated, combining these two technologies for a phased array antenna. The four element rectangular DRA array have been used as the radiating element along with tunable LC phase shifter in inverted microstrip line (IMSL) topology.

Liquid Crystal technology

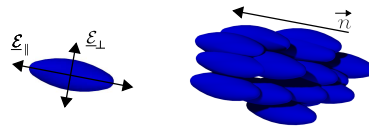


FIGURE 4.19: Liquid crystal molecule and bulk material.

LC materials have been very well known from display and optical applications. LC material is made up of anisotropic rod-like molecules as shown in Fig. 4.19. This irregularity in shape causes an anisotropy in dielectric constant values. This means that the effective dielectric constant depends on the direction of the electric field relative to the orientation of the molecule. The rod-shaped molecules are inclined to be orientated, i.e. the entire bulk orients in the same direction. This orientation is aided or dictated by the alignment layer that is used on the surface which the liquid touches. It causes an effective relative dielectric permittivity $\epsilon_{r\perp}$ and dielectric loss $\tan\delta_{\perp}$ respectively, which are along the alignment layer, i.e. perpendicular to the later applied electric field.

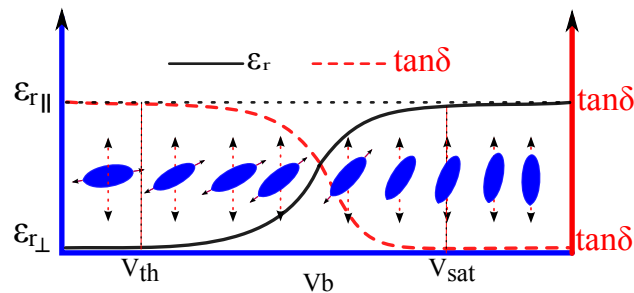


FIGURE 4.20: Continuous tuning of dielectric quantities [79].

The LC molecules begins to align themselves with the application of an external electric field, reaching an effective maximum $\epsilon_{r||}$ and $\tan\delta_{||}$ for a certain saturation voltage [80]. The amount of orientation is determined by the field strength. By means of the anisotropy of the LC molecules, the electric field can be applied to adjust the effective

permittivity of the LC layer inside the device continuously. This mechanism makes it possible to have a continuous tunability of the LC material. Preferential direction can be reoriented by means of mentioned applied voltage. As shown in Fig. 4.20, when the applied voltage V_b exceeds a saturation voltage V_{sat} , a corresponding permittivity and loss tangent is determined by the extent to which electrical field is incident on the molecules [79].

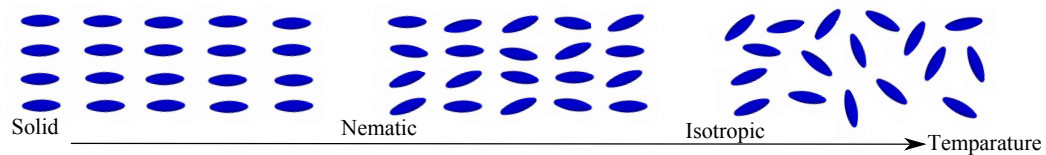


FIGURE 4.21: Temperature dependency of LC molecules.

Fig. 4.21 shows the temperature behavior of the LC molecules in a bulk. The starting orientation of molecules are depending on temperature. Because of anisotropy, all molecules tend to align parallel in room temperature. The molecule configuration changes from a relatively ordered state at a certain temperature, in which a preferential direction of the molecules can exist. If the temperature is increased further, all molecules are oriented randomly, into the so called isotropic phase [81]. In this case, molecules are not any more capable for tunability of phase shifter. Therefore, for the design of LC based phase shifter, temperature should be also taken into account.

There are two main topologies of tunable phase shifter depending on the technology. First method is periodically loaded transmission line topology, which assumes that the periodic structure is composed of pieces of non tunable transmission lines and shunt varactors. And these varactors determine the tuning capability of this kind of phase shifter. Another topology is the inverted microstrip line (IMSL), which is studied and proposed in this work. In this approach, the insertion loss is low, which makes this topology preferable. Moreover, inverted microstrip line is much easier to design and fabricate. In the following part of the thesis, the working principle of inverted microstrip line is explained.

Inverted microstrip line topology

The working principle of an inverted microstrip line is demonstrated in Fig. 4.22 [79]. The microstrip line and ground electrodes are present at the top and bottom of the substrates as shown in Fig. 4.22a. If the space between the substrates are filled with LC, a microstrip line can be constructed for which the LC layer acts as a dielectric-substrate material. A voltage source is connected to parallel plate substrates (Fig. 4.22c), which encapsulate the liquid crystal in between. The change of the applied voltage forms

orientation of LC molecules, which in turn changes the dielectric of IMSL. By applying a bias voltage, the dielectric constant of the LC is changed from $\epsilon_{r\perp}$ to $\epsilon_{r\parallel}$ continuously. This change is demonstrated in Fig. 4.22c and 4.22d.

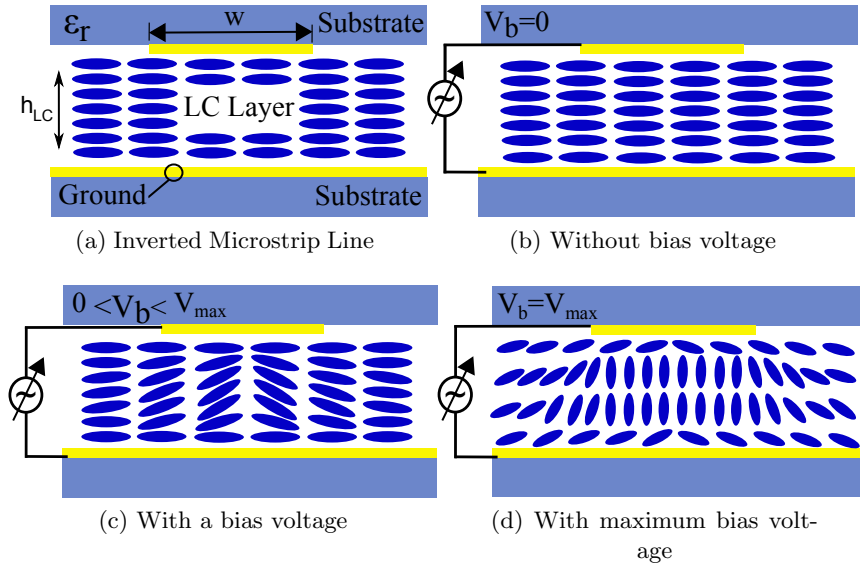


FIGURE 4.22: Cross section of an inverted microstrip line [54]

Antenna design

The perspective layered view of the proposed antenna is shown in Fig. 4.23. The two glasses at top and bottom are used as substrate for the antenna structure. The ground plane is present on the bottom of the top glass. The slots are etched in the ground plane for coupling the electromagnetic energy to the resonators. The DRAs are placed on the top of the upper glass. An inverted microstrip line based corporate feed network is implemented on the top of the bottom glass. The same plane also contains the biasing pads, the transition from coplanar waveguide to microstrip line for the measuring probes and bias lines. All the metal patterning is formed on the glass substrates by using standard photolithography process. This includes evaporating 20nm/60nm chromium/gold seed layer, photo resist spin coating, UV exposure, gold plating and gold/chromium etching. The same chromium layer which is needed as a seed layer for gold adhesion is then also used as the bias lines [82]. The lower conductivity of chromium metal ensures less influence on the microwave signal.

The glass substrates used here have three unique advantages. First, they offer great mechanical stability, which is very important in handling of the prototype during fabrication. Second, the substrates have uniform smooth surface which is required to achieve a uniform LC layer thickness. Third, the glass substrates are transparent which enables

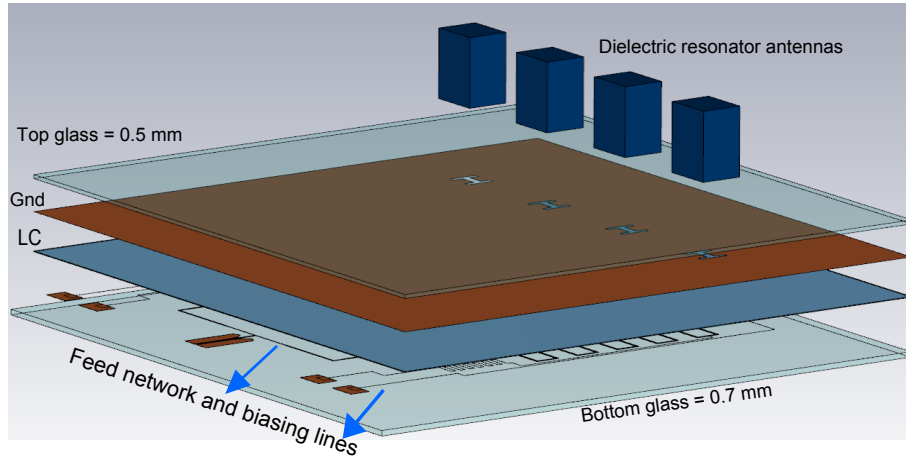


FIGURE 4.23: Exploded view of the LC based phased array with DRAs.

easy alignment by using markers on the different layers. Commercially available borosilicate float glass material, which is commonly known as borofloat 33, with permittivity of $\epsilon_r = 4.4$ and $\tan\delta = 0.0073$ at around 5 GHz has been used [83]. The LC material is sandwiched between 0.1 mm gap present between the two glass substrates. The gap of 0.1 mm is achieved by using 0.1 mm spacers between the glass layers. This fabrication technique is not new but rather is very mature process that has been used in the LC display industry for many years. Therefore, a possibility of mass production can be automated easily due to the well known fabrication process in industry. The substrates are then aligned by using complimentary alignment markers with the help of mask aligner and bonded with glue from every side except a small hole for filling the LC. After the LC material is filled into the cavity and the structure is fully sealed to prevent any LC leakage.

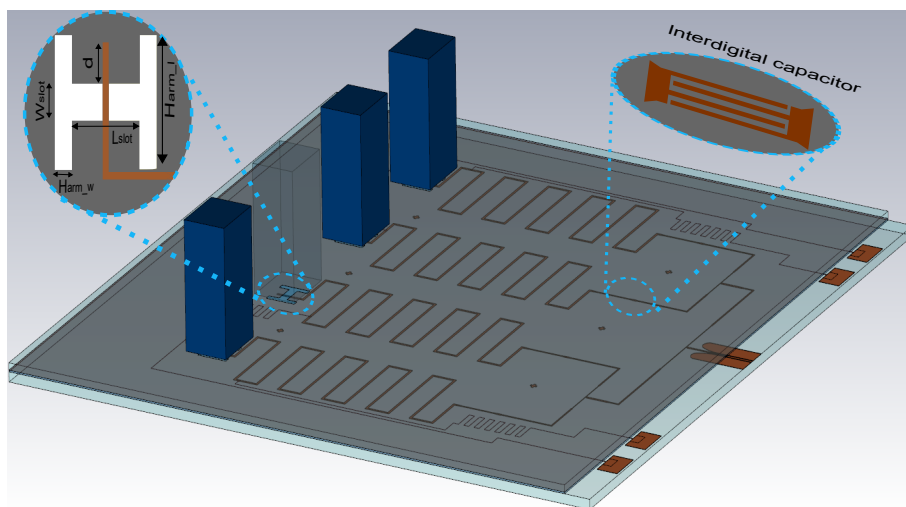


FIGURE 4.24: Two glass layers of the structure.

The DRA elements are manufactured made from bulk-glass ceramic material from

SCHOTT AG, with permittivity of $\epsilon_r = 22$ and $\tan\delta = 0.005$ at around 8 GHz. The DRAs are placed on the top of the upper glass with the help of glue. Bulk-glass ceramics are a new class of material which possess good microwave properties [13] and have already been used in making DRA [84]. The DRAs must be positioned on the right place over the H-shape slot. The dimensions of the slot are shown in Fig. 4.24(a). The placement was aided by markers on the top of the second glass. The thickness of the top glass is important as it is directly under the DRAs with slots on the other side. A thinner glass would ensure good coupling but at the same time the mechanical stability has to be kept in mind while choosing the thickness. A careful choice of 0.5 mm was made for the top glass thickness. A thickness of 0.7 mm was chosen for more mechanical robustness for the bottom glass.

Simulation procedure

At first, simple rectangular slots were employed, but the coupling was very weak. After looking for other possibilities of slot shapes, simulations showed that the coupling of the H-shaped slots was reasonable. These H-shaped slots were able to couple the energy into the dielectric resonator from the inverted microstrip line through the slots in the ground plane below the top glass. DRAs of $4 \text{ mm} \times 5 \text{ mm} \times 9 \text{ mm}$ were found to have a good matching with the slot at 10 GHz. This means that the DRAs are actually longer than their length for the first fundamental resonance. Longer DRAs here means the radiations happens away from the ground plane, and therefore will have less effect on the ground plane currents.

The differential phase shift between the array elements was simulated by changing the LC permittivity under the individual inverted microstrip line branch separately. According to Fig. 4.20, simulations were performed for a change in permittivity of the LC material from $\epsilon_{\perp} = 2.1$ to $\epsilon_{\parallel} = 3.3$ ($\Delta\epsilon_r = 1.2$), which corresponds to the LC material being used. The LC material with variable permittivity is shown in green color in Fig. 4.25. As can be seen the left most branch of the inverted microstrip line in the feeding network has a change in the permittivity of the whole LC material of $\epsilon_{\parallel} = 3.3$ between the inverted microstrip line and ground electrode. The next two branches in the feed network from the left has two third ($\epsilon_{\perp} + \frac{2}{3}\Delta\epsilon_r$) and one third ($\epsilon_{\perp} + \frac{1}{3}\Delta\epsilon_r$) changed LC material permittivity. While the last branch on the most right has no change in permittivity of the LC material. This causes a corresponding progressive phase shift between the radiating elements. As the permittivity value is changed by an applied electrostatic field, the beam is scanned as shown in Fig. 4.26. A maximum of 52° is achieved, when the permittivity of the LC material reached its maximum value of 3.3.

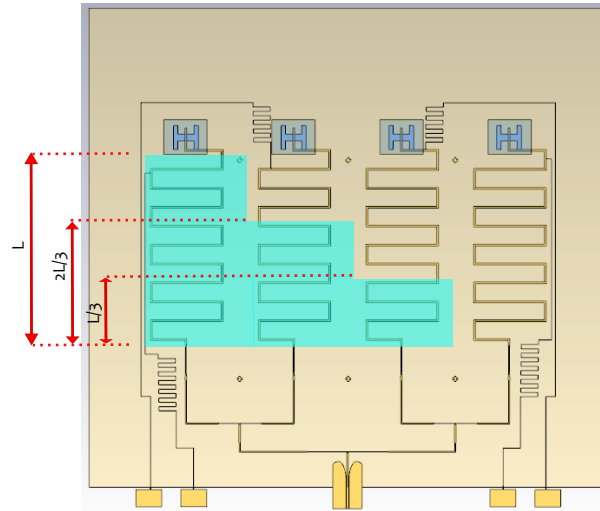


FIGURE 4.25: Simulating the differential phase shift by changing the LC permittivity.

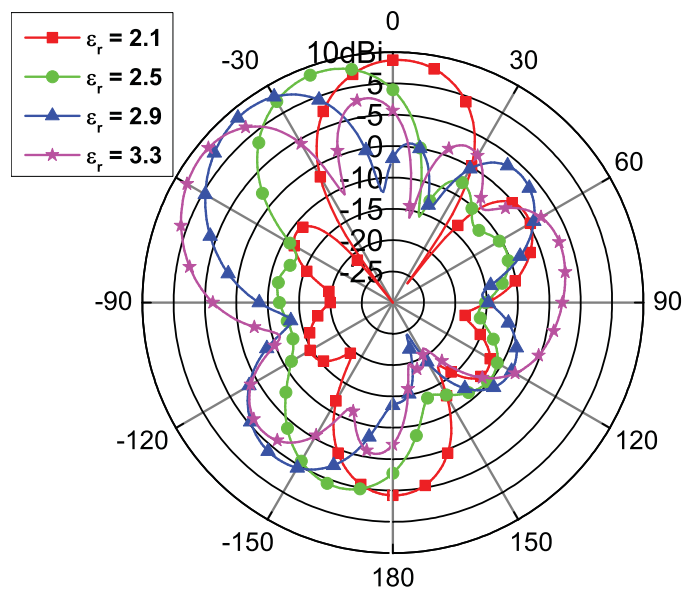


FIGURE 4.26: Simulated beam directions with different LC permittivity at 10 GHz.

Measurement results of phase shifter

The first step in the measurement was to characterize the phase shifter capabilities. Since the phase shifters in the fabricated array were not measurable (unless near field scanning would be usable), a separate phase shifter was fabricated with similar dimensions as the one in the phased array antenna. The stand alone phase shifter is shown in Fig. 4.27

The only difference to that of the phase shifters in the antenna array is that it contains two interdigital capacitors (IDC) and two inverted microstrip line to coplanar waveguide transitions in order to measure the S-parameters. The other physical difference is that the ground plane is actually a 0.5 mm copper plate for the stand alone phase shifter.

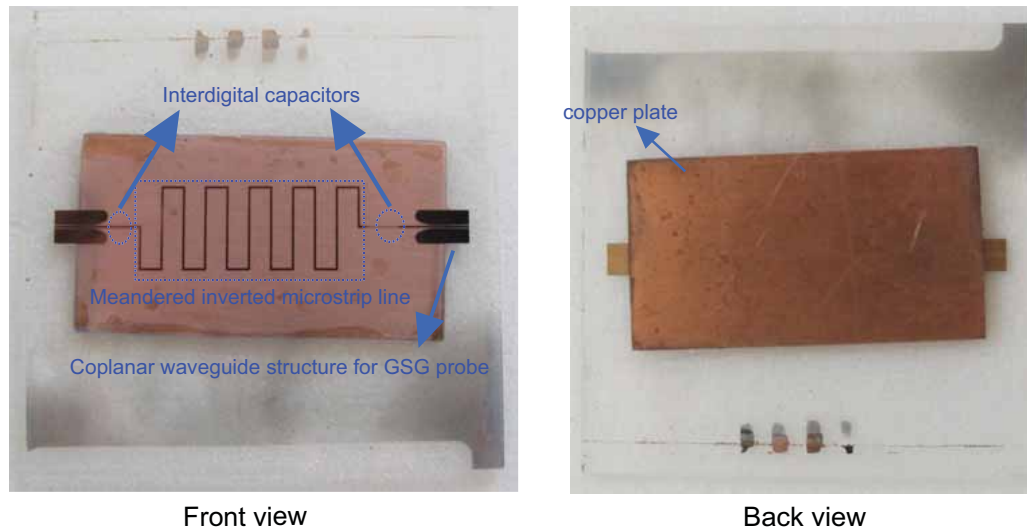


FIGURE 4.27: Fabricated inverted microstrip line based stand alone phase shifter.

The ground plane in the antenna is the copper plated glass. This is electrically the same. The important parameter for the copper plate is the flatness of the surface. Since the glass is assumed to be very flat, the copper plate should also be as flat as possible.

The measured S-parameters of the meander delay line phase shifter are shown in Fig. 4.28. The results are for the unbiased ($V_b=0$ V) and full-biased $V_b = 40$ V cases are shown in bold lines. These two extreme boundaries will define the minimum and maximum LC dielectric losses at the corresponding orientations of the molecules, respectively [60]. The return loss is noted to be about -17 dB. The insertion loss of the phase shifter with the two CPW to microstrip line transitions and interdigital capacitors is around -3.8 dB. From the simulations of the transition and inter digital capacitor is known that, the insertion loss due to interdigital capacitor and transition is around -0.5 dB. Thus the maximum insertion loss of the inverted microstrip line is actually close to -2.5 dB.

In Fig. 4.29, differential phase shift $\Delta\Phi$ over voltage is illustrated. The threshold voltage is around 7 V. The slope of the curve between the range of 10 to 15V is very high, which makes the voltage adjustment very sensitive. After about 20V, the dependency has a nearly linear nature. With the maximum applied voltage, the maximum amount of differential phase shift is $\Delta\Phi=200^\circ$. The insertion loss is around -2.5 dB. Therefore, the figure of merit ($FoM = \Delta\Phi/IntertionLoss$), can be calculated as $FoM=80^\circ/\text{dB}$.

Antenna prototype

The fabricated antenna prototype with four DRA elements on top is shown in Fig. 4.30. The simulated and measured return loss for this prototype is shown in Fig. 4.31. The possible reasons for difference in both curves are imperfect fabrication, leakages of the

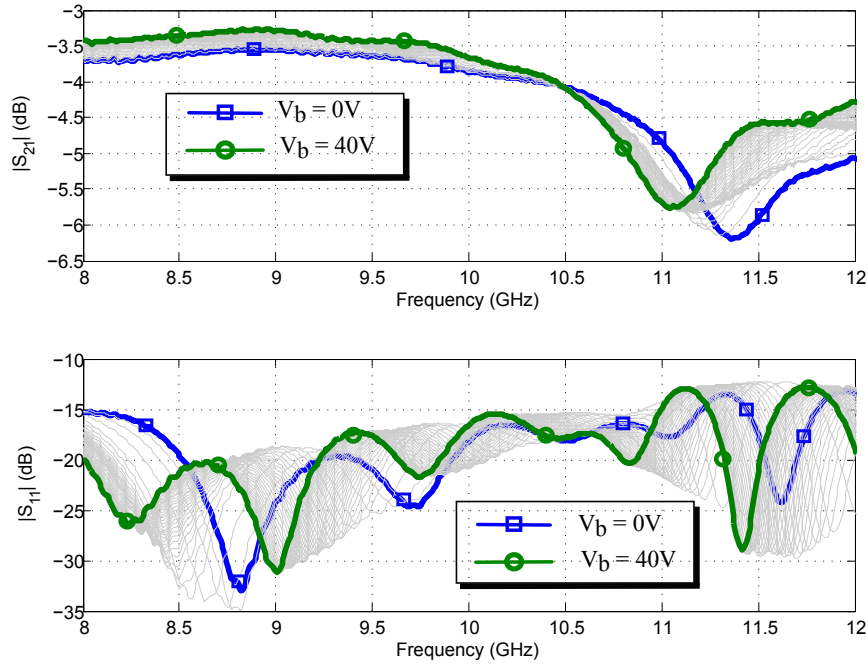


FIGURE 4.28: Magnitude of the transmission coefficients of the inverted microstrip line for different applied voltages V_b

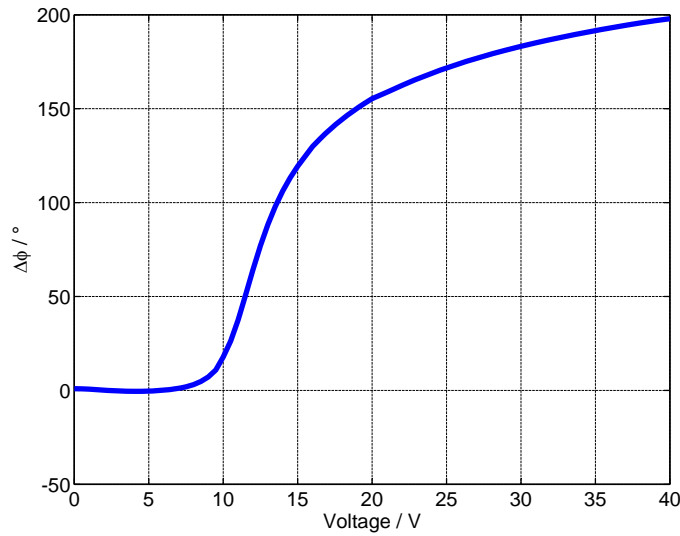


FIGURE 4.29: Differential phase shift $\Delta\Phi_b$ characteristics of the inverted microstrip line versus an applied voltage at 10 GHz

glue into the LC layer between the two glasses, the spacers in the LC layer and more metalization losses than expected. Since the dielectric elements were also fixed by hand with the help of glue over the slots, some misalignment is expected there too. Another important factor that might have caused the difference in the measurement was the surrounding in which the measurement of the return loss was undertaken. Since it was measured on a manual wafer-probe with a GSG probe of 250 μm pitch, a lot of metallic structure around the antenna was present, where the interaction of the metallic

surroundings with the near field or leaking radiations cause disruptions in the measurements. Nevertheless, there are resonances around 9.6 GHz and 10 GHz that correspond to the simulations.

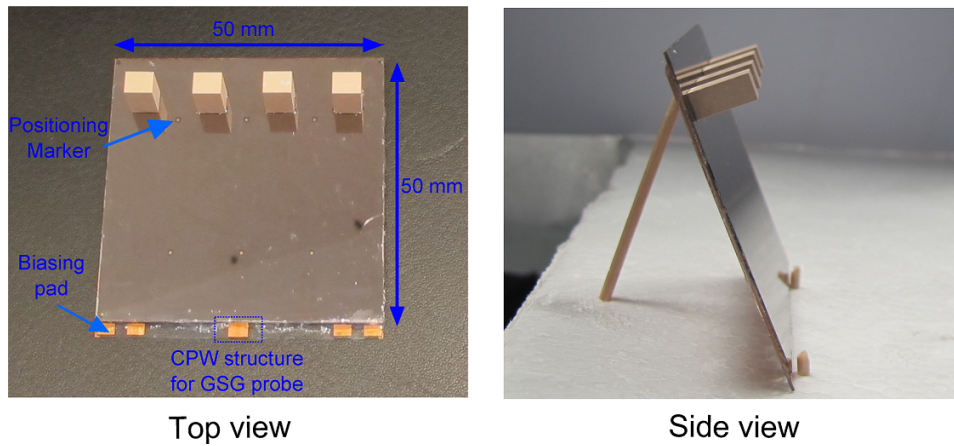


FIGURE 4.30: Fabricated antenna prototype

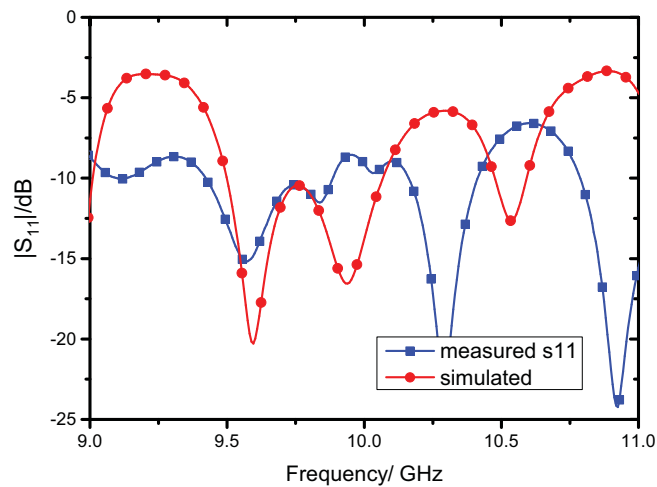


FIGURE 4.31: Simulated and measured return loss of the fabricated antenna array.

From the measurements in the anechoic chamber, the main beam was found to be at 10 GHz, which is a little deviated from what is evident from the reflection results. It is due to the fact that the measurement setups for the reflection loss and far field pattern were different. The simulated and measured E-plane far field patterns at 10 GHz are shown in Fig. 4.32. The measurement results show a very good agreement with the simulations. Side lobe level of -13 dB is measured corresponding exactly to the simulated value. There are some small differences between simulated and measured results, due to the experimental setup. The experimental setup for far field pattern included a special structure for keeping the contacting ground-signal-ground (GSG)

probe firm with the help of adjustment knobs and holder. Since this structure was made of metal, some interaction with the fields was inevitable even though many absorbing material strips were used to minimize the effects. In addition, the biasing wires could also cause some degree of distortion. There is -16 dB difference, between co- and cross-polarization making it a linearly polarized antenna.

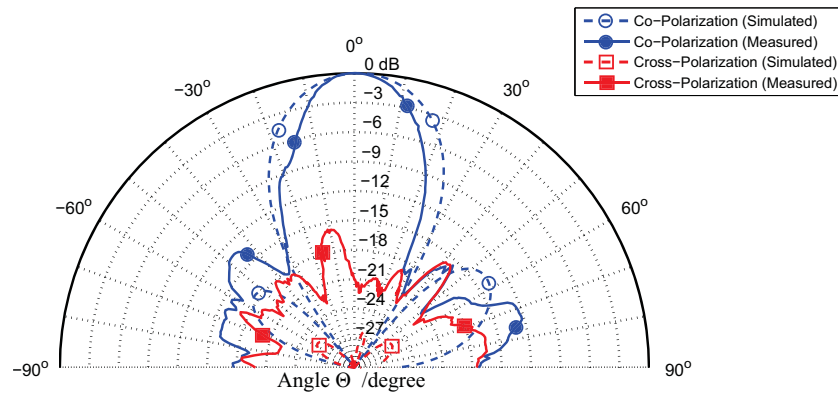


FIGURE 4.32: Measured E-plane of antenna at 10 GHz.

Fig. 4.33 shows the H-plane far field pattern of the antenna, which shows the primary lobes of the measured patterns are in agreement with the simulations. An exception in the form of a dip around 50° can be noted, which is a due to the measurement setup as has been explained earlier. The difference between the co- and cross-polarization in the H-plane is around -13 dB.

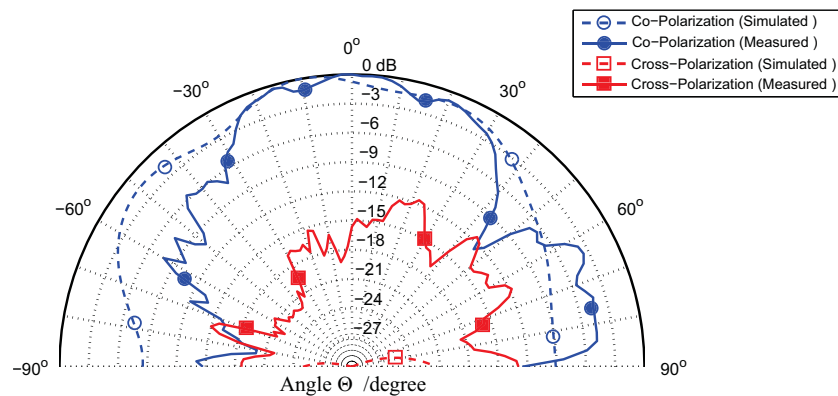


FIGURE 4.33: Measured H-plane of the antenna at 10 GHz.

The beam steering capability of the prototype was tested by applying differential phase shift between the radiated elements. The phase shift is achieved by applying different bias voltages between the feed network branches and ground electrodes. The voltage was first determined by characterizing a standalone phase shifter as discussed earlier.

Fig. 4.34 shows different steered beams for the prototype. A beam steering angle of nearly $\pm 25^\circ$ is achieved. This demonstrates successfully the beam steering capability of this antenna array. A significant fact which can be noticed from Fig. 4.34 is that the

beam with main direction $+15^\circ$ degrades only about 0.5 dB from that of the reference beam at 0° . The degradation in the $\pm 25^\circ$ beams can be attributed to the interaction of the antenna with the setup.

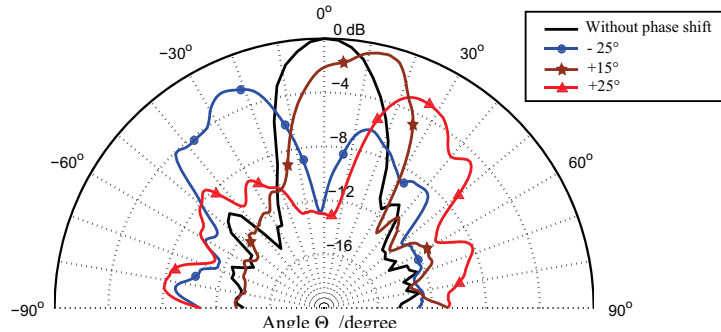


FIGURE 4.34: Measured scanned far field patterns at 10 GHz

4.2.2 Barium Strontium Titanate based phased array

Barium Strontium Titanate (BST) is another promising material with a tunable ϵ . The advantage of BST is the fact that it is solid (as opposed to LC material), and hence, relatively easy to handle. A comprehensive work about BST can be found in [58], [56], [57]

A BST phase shifter based phased array with wideband stacked dielectric resonator antenna elements has been designed. It is also for the first time that BST phase shifter and DRA elements have been combined and demonstrated in a phased array setup.

Wideband stacked DRA elements

The BST phase shifters (or any phase shifter) which employ non-resonant structures have a very wide bandwidth. To put the wide bandwidth of the phase shifters to full use the radiating elements must also be broadband. The design of the wideband element based on stacked dielectric resonator antenna is explained first. This element is then tested in a 1×4 phased array configuration with BST phase shifters.

The requirement for a radiating element for any phased array is to be compact in size and wide bandwidth. The compact size is important in order to have less mutual coupling between the adjacent array elements. The basic configuration of the stacked DRA antenna element is shown in Fig. 4.35. The design consists of two substrates. The top substrate is Rogers 4003C, while the bottom substrate is alumina. Presence of alumina substrate is a necessity dictated by the use of the BST phase shifters. The BST is a

ceramic which needs high sintering temperature, therefore, alumina has been used as the carrier substrate of choice, because of its stability at high temperatures.

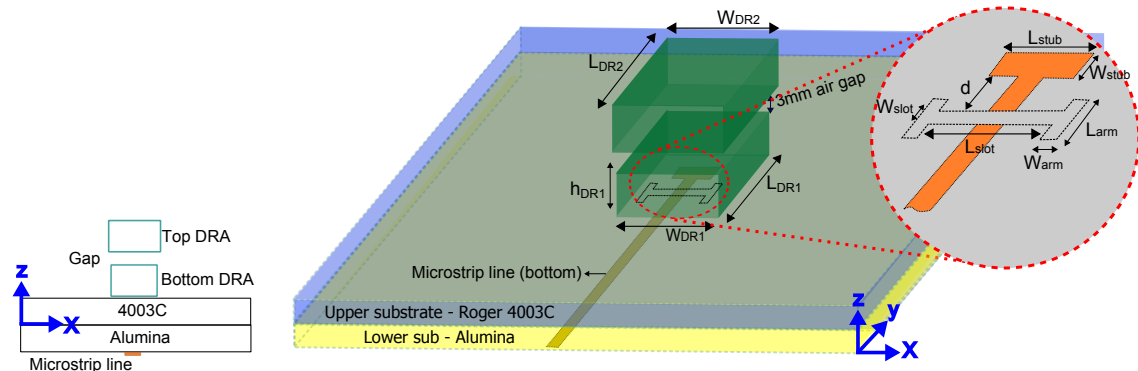


FIGURE 4.35: Design of a stacked DRA element.

A 50Ω microstrip line is printed on the bottom of the alumina substrate. A higher permittivity of bottom substrate helps in reducing the radiation from the microstrip line in the lower half space, which is also known as back radiation. A ground plane containing an H-shaped slot with dimensions $L_{slot} = 4.5$ mm, $W_{slot} = 0.35$ mm, $L_{arm} = 2.3$ mm and $W_{arm} = 0.6$ mm is present on the bottom of the top substrate. This slot couples the electromagnetic energy from the MSL to the stacked DRA.

The two DRAs are placed on the top of the slot. The lower DRA is a little smaller than the top DRA with length $L_{DR1} = 7.7$ mm, width $W_{DR1} = 6.7$ mm and height $h_{DR1} = 2.5$ mm. The upper DRA dimensions of $L_{DR2} = 8.7$ mm, width $W_{DR2} = 7.7$ mm and height $h_{DR2} = 3.3$ mm. There is a gap of 2 mm between the two DRAs. High permittivity low loss bulk-glass ceramic material from SCHOTT AG with ϵ_r of 33.4 and loss tangent of 0.0016 at 7.3 GHz is used to manufacture the DRAs.

The dimensions of the lower DRA is adjusted with the slot such that the dominant TE_{111} mode is excited at the frequency of interested. This frequency was chosen because of some practical limitation of the clean room and ease of manufacturing for the DRAs. Keeping in mind the in-house photolithography process limitation and the maximum size of Alumina substrates with BST printing the frequency was fixed at about 8 GHz. At this frequency, the a 1×4 array would be possible to manufactured with the in-house facilities.

The return loss of the stacked DRA element is shown in Fig. 4.36 for different air gap values. The air gap between two DRAs effects the bandwidth. A bandwidth of 23.5% was achieved with air gap of 2 mm. When there is no air gap, i.e. the top DRA is placed directly on the lower DRA, the matching is distorted totally. This is understandable, as by placing the top and bottom DRAs together, is similar to one DRA with a bigger

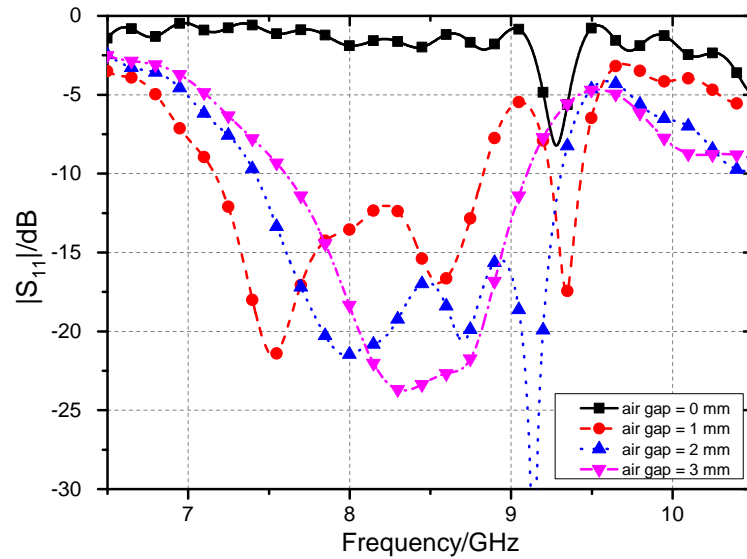


FIGURE 4.36: Simulation of the air gap influence on the matching bandwidth.

dimension. Therefore, the matching at this particular frequency (in this case around 8 GHz) is disturbed.

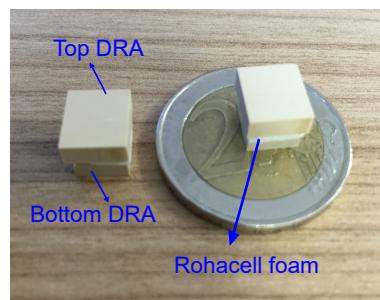


FIGURE 4.37: The stacked DRA element with ROHACELL as the air gap.

The stacked DRA is made by precisely machining the rectangular individual DRAs from bulk-glass ceramic material. The two DRAs are then stacked over each other by using ROHACELL $\text{\textcircled{R}}\text{HF}$ foam [85] as shown in Fig. 4.37. This foam simulates the air gap between the two DRAs as it is very low loss and with permittivity close to 1. The foam is mechanical stiff, and hence, the stacked DRA structure is stable. A daily use quick glue is used to stick the two DRAs to the foam.

The stacked DRA is then placed over the two substrates. The two substrates and SMA connector are housed in a fixture for stability and alignment. The fixture was simulated along with the antenna to see the influence. It was found to have negligible effect. The stacked DRA is also glued with a common daily use quick glue. The glue should be used in as little as possible quantity as the height of the DRA on the substrate influences the matching bandwidth. The fabricated single element DRA antenna is shown in Fig. 4.38.

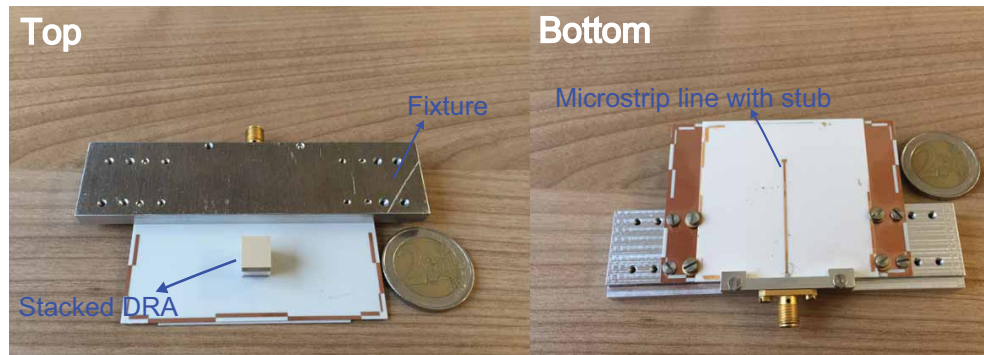


FIGURE 4.38: Stacked DRA antenna prototype.

The measured return loss is shown in Fig. 4.39. The simulation and measurements agree very well to each other. The measured -10 dB bandwidth is close to 20% starting from 7.5 GHz to 9.1 GHz. This misplacement and inaccuracies in the stacked DRA caused a little differences between measured and simulation curves. The glue also has some effect as it introduces some gap between the radiating element and the substrate.

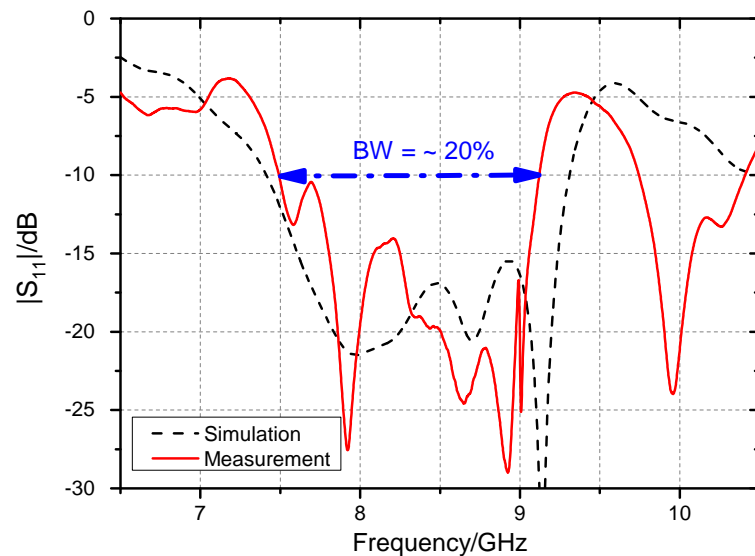


FIGURE 4.39: Reflection loss measurement of the Stacked DRA element.

The two principal planes of radiation for the stacked DRA antenna are shown in Fig. 4.40. The antenna far field is linearly polarized as depicted by the difference of around 20 dB between the co- and cross-polarization levels. The gain measured at 8 GHz was 7.2 dBi, which is very close to the simulated value.

The stacked DRA antenna with maximum dimension of only $0.23 \lambda_0$ has proved to be a compact radiating element with a wide bandwidth suitable for an array configuration. This radiating element is then used in a 1×4 array configuration with phase shifters which is explained in next section.

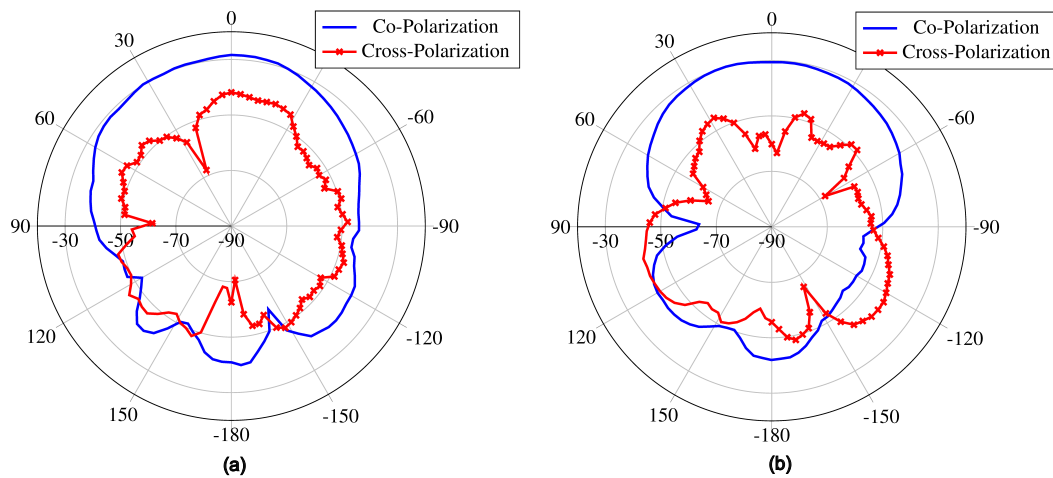


FIGURE 4.40: (a) E-plane (b) H-plane measurement in anechoic chamber.

1×4 phased array antenna based on BST phase shifters

The 1×4 array configuration is chosen as a proof-of-concept of stacked DRA elements and BST based phased shifters in a loaded line topology with metal-insulator-metal (MIM) capacitors.

The array contains the corporate feeding network, the BST phase shifters, the bias lines and the stacked DRA elements as shown in Fig. 4.41. The corporate feeding network is a simple power divider such that each branch gets equal power. Each branch of the feeding network contains a phase shifter, thus, the phase of each element can be individually and independently changed. It is in reality not just a phase shifter but rather a true delay line, which is superior to a pure phase shifter because there is no dispersion affect.

MIM based phase shifter design

A small introduction about the tunable BST MIM technology for capacitor-loaded phase shifters is given here for completeness. For more details the reader is referred to [56].

In order to achieve phase shifter for microwave applications, capacitance values in the sub-picofarad (1 pF) range are needed. A MIM capacitor achieves such values easily because of the high capacitance density. The high capacitance density comes from the high dielectric constant of BST thin films. So they need either sub-micron lithography or series connection of capacitors, both of which require expensive multi-layer photolithography.

A MIM based varactor has the following advantages:

- Lower tuning voltages in the range of 5–30 V, and

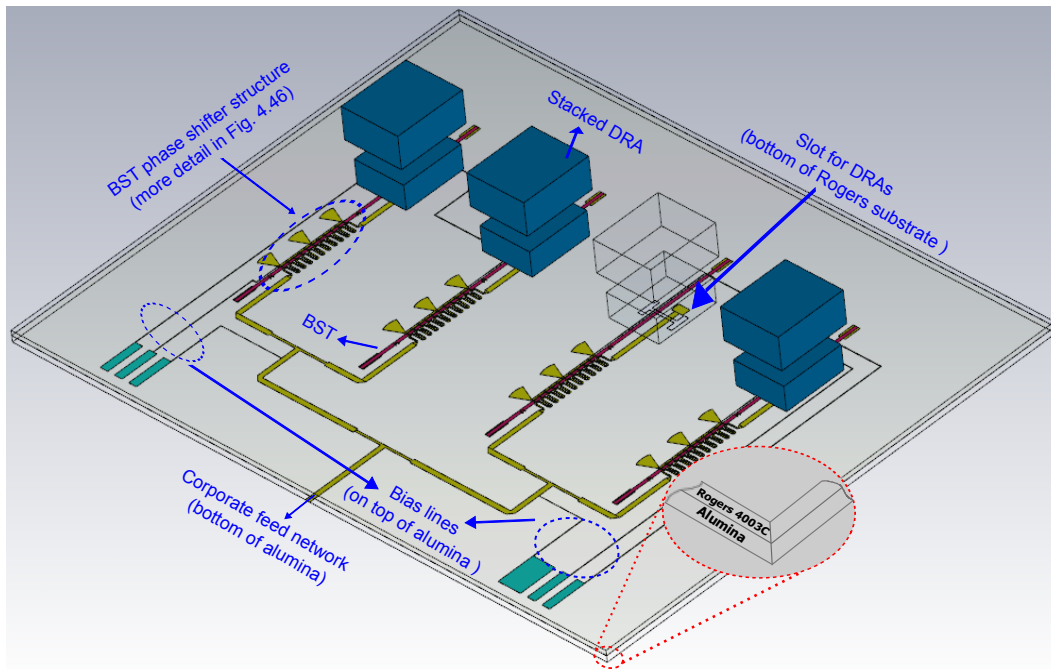


FIGURE 4.41: 1×4 phased array configuration with BST phase shifters and stacked DRAs.

- Very high capacitance density in the range of $10 - 40 \text{ fF}/\mu\text{m}^2$.

Its disadvantages are:

- Not capable of handling high power compared to interdigital capacitors (IDCs),
- Poor linearity,
- Growth of thick bottom electrode required for high Q capacitors can be challenging, and
- Processing steps are more complex as compared to planar IDC-based varactors.

The layout MIM varactor unit cell used in the phase shifter is shown in Fig. 4.42. It consists of three layers, the top and bottom conductor with the tunable dielectric sandwiched in between. The MIM capacitance is formed by the intersection of the top and bottom electrode. Thickness of the BST layer defines the distance between the two metals. Thicknesses of $1 \mu\text{m}$ or even a little below can be achieved, which results in lower maximum voltage requirement for tunability.

To measure the capacitance, two lines that behave as parasitic inductance with $350 \mu\text{m}$ gap were attached to the varactor. These lines are indicated as signal and ground lines in the Fig. 4.42.

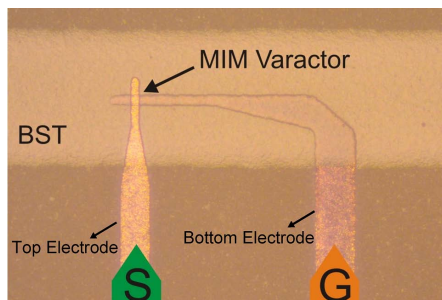


FIGURE 4.42: Layout and equivalent circuit of the MIM varactor.

The fabrication is done on a Al_2O_3 substrate, which is used as carrier substrate (height of $0.635\ \mu\text{m}$ and relative permittivity of about 10). The first layer is gold bottom electrode. For better adhesion between bottom electrode and the alumina substrate chrome-nickel/gold (20 nm / 80 nm) seed layer is evaporate prior to gold deposition. The patterning of the RF electrodes was done by photolithography and gold electroplating process followed by etching of the gold seed layer.

Inkjet printing was used to deposit BST lines with a width of approximately $300\ \mu\text{m}$ and a thickness of $1.1\ \mu\text{m}$ at the specified locations on the substrate. The alumina substrate with the BST lines is then sintered at $850\ ^\circ\text{C}$ for 1h. The material properties of the BST layer are obtained by S-parameter measurements of a coplanar waveguide patterned on top of the BST films are shown in Table 4.1

Frequency	10 GHz
Relative Permittivity	133
Tunability	23%(10V/ μm)
Loss Tangent	0.07

TABLE 4.1: The characteristics of an inkjet printed BST film.

The relative permittivity ϵ_r of 133, $\tan\delta = 0.07$ and tunability of 23% by applying $10\ \text{V}/\mu\text{m}$ at 10 GHz are measured. Finally, $3\ \mu\text{m}$ top electrodes are patterned with electroplating similar to the bottom electrodes.

Tunable Loaded Line Phase Shifter

The basic MIM unit cell is then used in the loaded line topology for constructing the tunable phase shifter. Each unit cell consist of one varactor and inductance line. Input impedance and phase velocity are defined by:

$$Z_0 = \sqrt{\frac{L_t}{C_t}}, \quad v = \frac{1}{\sqrt{C_t \times L_t}} \quad (4.11)$$

A total of 11 unit cells were used to construct the whole phase shifter, which is shown in Fig. 4.43.

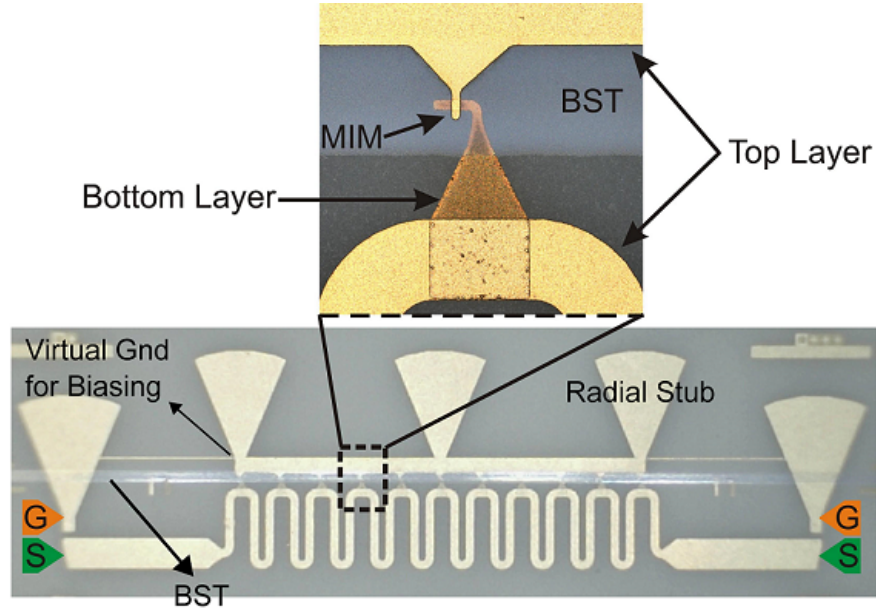


FIGURE 4.43: Layout of the 11 unit cell loaded line phase shifter. The ground-signal probes with 350 μm pitch are used for measurements.

Its insertion loss and return loss are measured with a vector network analyzer shown in Fig. 4.44. The biasing voltage was applied through a bias-T between the signal and ground electrode.

Phase shifter prototyping and measurement results

To evaluate the total performance of the phase shifter, a figure of merit (FoM) is introduced, which is defined by:

$$FoM = \frac{\Delta\varphi}{IL_{max}} \quad (^\circ/\text{dB}), \quad (4.12)$$

where $\Delta\varphi$ represents the maximum phase shift in degree, while IL_{max} is the maximum insertion loss. A maximum measured phase shift of 260° is achieved by applying a maximum bias voltage of 50V. The maximum insertion loss of the phase shifter in the untuned state is 5.9 dB which provides a figure of merit (FoM) of $44^\circ/\text{dB}$ at 8 GHz. Fig. 4.45 shows the FoM and phase shift as calculated from the measurement data.

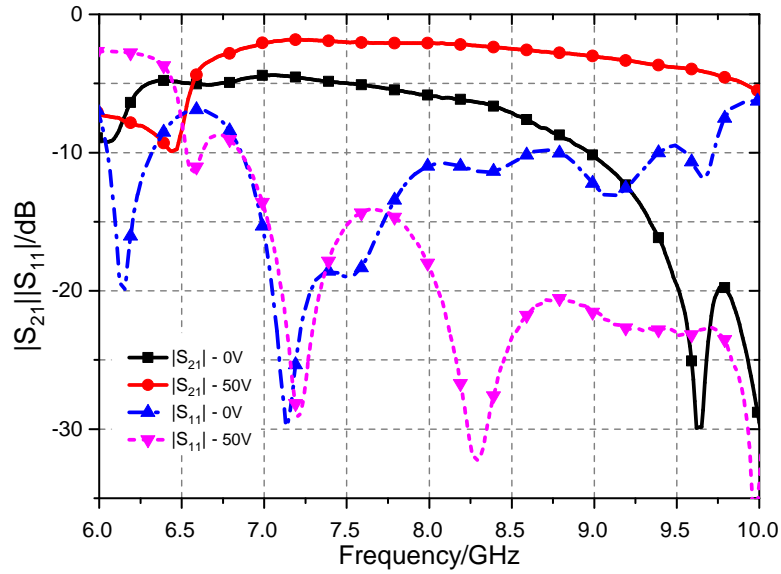


FIGURE 4.44: Measurement results of the 11 unit cells loaded line phase shifter with 0V and 50V bias voltage.

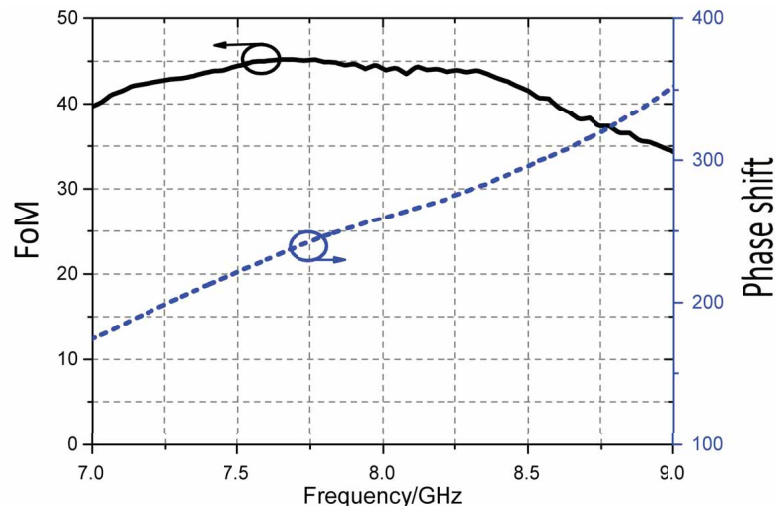


FIGURE 4.45: FoM and phase shift of the 11 unit cell loaded line phase shifter as calculated from the measured data with maximum bias voltage of 50V.

The 1×4 phased array is constructed by making 4 phase shifters in each branch of corporate feeding network. The bias lines are $20 \mu\text{m}$ lines. They are expected to behave almost invisible for the RF signal due to their high impedance. The two substrates are aligned with the fixture, which also contains the SMA connector. The stacked DRA as discussed previously are placed on the top over the slots at precise locations. The fabricated antenna array is shown in Fig. 4.46.

The simulated and measured return loss of the fabricated array antenna without a bias voltage (0V) is shown in Fig. 4.47. The matching around the center frequency is quite good. The -10 dB bandwidth is observed from 7.0 to 8.4 GHz. It should be noted that

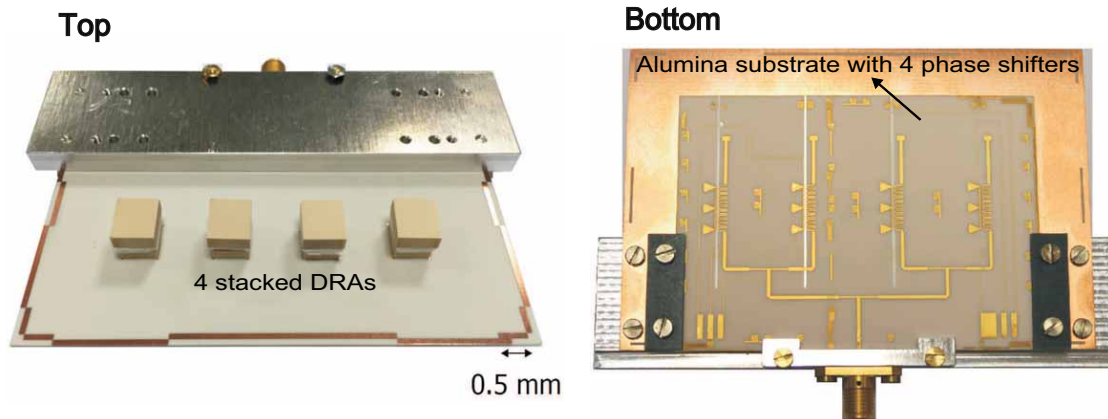


FIGURE 4.46: Fabricated 1×4 phased array with stacked DRA elements and BST-based MIM-varactor loaded line phase shifters.

the simulated S_{11} does not include the phase shifter losses. Therefore, there is an offset in the return loss measurement, which is equal to the loss of the phase shifters. The notch behavior is typical to array antennas, and hence, expected.

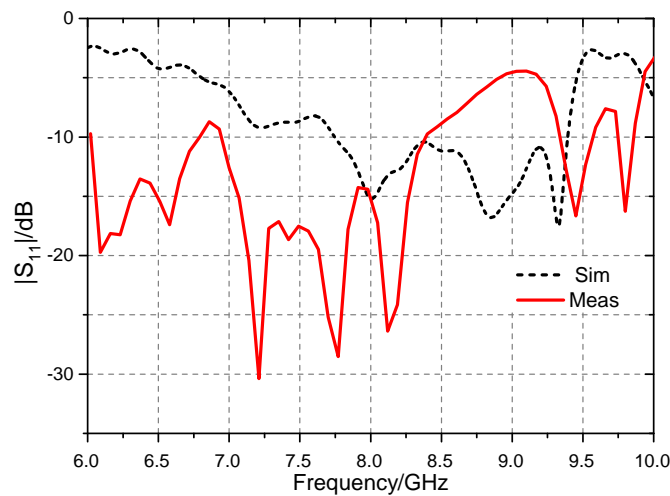


FIGURE 4.47: Return loss of the Fabricated 1×4 phased array without any bias voltage.

Beam steering was evaluated by performing the far field pattern measurements in an anechoic chamber. The measured and simulated far-field pattern is shown in Fig. 4.48. A differential phase shift of 80° has been applied between each antenna element through proper bias voltage. Broadside pattern is obtained when no bias voltage is applied, i.e. the BST is in an untuned state. Beam steering is about $\pm 30^\circ$ when a differential phase shift of 80° is applied between each element. The gain loss with the beam steering to $\pm 30^\circ$ is less than 1 dB, which is quite low.

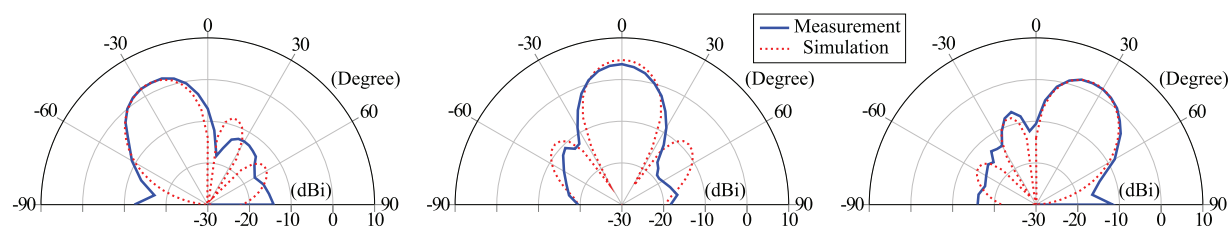


FIGURE 4.48: Far-field gain pattern of scanned beam for the fabricated 1×4 phased array.

Chapter 5

Summary and Outlook

The work was concerned mainly to investigate novel concepts using dielectric resonator antennas (DRA) based on different microwave materials: glass, ceramics and glass-ceramics. The microwave characterization of newly formulated glass-ceramic materials was performed. New glass and glass-ceramic materials with ϵ_r in range 17 to 38 and Qf values of 1500 to 10 000 GHz were found. The temperature coefficient of resonance frequency $|\tau_f|$ of many compositions were $< 50ppm/K$, which is already adequate for many applications. As compared to sintered ceramic, which is commonly available material, the glass-ceramic material offers advantages of more homogeneity, pore-free structure, less shrinkage upon ceramization and less batch to batch variation of microwave properties. The production is also comparatively less complex.

After characterization, the material was used to demonstrate its usability for fabrication of various DRAs and arrays. Dielectric loaded antennas in the form of a patch which could potentially benefit from advantages offered by the glass-ceramics, were fabricated and tested successfully. The less batch to batch variation and pore-free structure of glass-ceramics has large potential for replacing the conventional ceramics used presently. The material however, remains to be tested with mass production processing methods, i.e. screen printing, which is currently used for low cost manufacturing of the dielectric loaded patch antennas.

In addition, not only the ceramized glass-ceramic, which is opaque, but the non-ceramized glass, which is in transparent form with different colors was utilized to make DRA. The transparent glass was characterized for the microwave properties, and it was found to be suitable for making DRA. The non-ceramized form was hence used in fabrication of transparent DRA. Due to the high value of ϵ_r and adequate losses, small aesthetically pleasing transparent antennas could be fabricated using the glass. A transparent antenna from another production grade clear glass LASF35 was then used to make a

transparent antenna on the top of a solar cell module. An off the shelf solar cell module was used to demonstrate this antenna concept. Further research for optimization can be done in this area, especially when a fabrication facility of solar cell layers is available. Then, a complete array, using the same concept of integrated solar cell layer with the transparent DRA on the top, can be manufactured, which could have applications in the satellite or even daily consumer electronics market.

Another novel concept of directed beam DRA was introduced. It was fabricated using a tilted DRA. The tilt of the DRA guided the far-field pattern to be tilted along with the tilt of the DRA. Such antennas could potentially have applications where a radiation towards a specific direction is required without tilting the whole antenna (radiating element plus ground plane). The tilted antenna element was also used in a fixed beam array configuration, with the advantage of covering low elevation angles with adequate gain. The fabrication of the tilted DRAs was done piecewise with the aid of laser cutting of alumina substrate. This method could also be potentially a cheap production for DRAs especially for higher frequencies where one dimension of the DRA is close to the maximum substrate height which the laser could cut. A further work in this direction would be to make a full 2D steerable array with tilted elements such that the gain of array is more or less constant from broadside to very low elevation angles.

Apart from the single element DRA, beam steering arrays with passive phase shifting technologies based on Liquid Crystal (LC) and Barium Strontium Titanate (BST) were also investigated. The beam steering of LC based phase shifters at 10 GHz was demonstrated with a 1×4 array configuration. The array successfully showed steering of the beams in -25° and $+25^\circ$ direction. Using LC material based beam steering has some potential at millimeter and THz frequencies, since LC is a material which has a decreasing $\tan\delta$ with increasing frequency. Similarly, DRAs are beneficial at higher frequencies too, due to higher efficiencies. Therefore, a combination of both, LC and DRAs, would be crucial for higher frequency applications. Further work in this regard would be to extend the prototypes frequency range in the millimeter wave regime, thus benefiting from both, the lower losses of LC and higher efficiency of DRAs.

Moreover, a 1×4 BST based beam steering array was also fabricated which showed beam steering of -30° and $+30^\circ$ at 8 GHz. It used stacked DRA elements for wideband operation. The stacked elements made use of ROHCACELL material mimicking the air gap between the two dielectric pieces. The BST offers advantage of being solid, and hence, easier to handle. It also offers lower losses at lower frequencies, which when combined with wideband features of DRAs makes a good combination.

In essence, the thesis has in particular validated the whole life cycle of glass-ceramic materials. For which, glass-ceramics compositions were prepared and characterized first.

Then, the characterized data was used in simulating different antennas by using 3D simulation software. In the end, the fabrication and antenna measurements, substantiating the characterized values and the simulation models. Thus, making glass-ceramics as one of the possible materials to be used in the field of miniaturized, efficient and possibly cost effective microwave antennas.

Bibliography

- [1] R. Richtmyer, “Dielectric resonators,” *J.Appl. Phys.*, vol. Vol. 10, pp. 391–398, 1939.
- [2] S. A. Long, M. W. McAllister, and L. C. Shen, “The resonant cylindrical dielectric cavity antenna,” *IEEE Transactions on Antennas and Propagation*, vol. 31, May 1983.
- [3] M. T. Sebastian, *Dielectric Materials for Wireless Communication*. Elsevier Science, 2008.
- [4] A. Petosa and A. Ittipiboon, “Dielectric resonator antennas: A historical review and the current state of the art,” *IEEE Antennas and Propagation Magazine*, vol. 52, pp. 91–116, Oct 2010.
- [5] A. Petosa, *Dielectric Resonator Antenna Handbook*. Artech House, 2007.
- [6] E. H. Lim and K.-W. Leung, “Dielectric resonator antennas,” 2003.
- [7] S. P. Kingsley, B. S. Collins, D. Iellici, J. W. Kingsley, S. G. O’Keefe, and T. J. Palmer, “Advancements in antennas, the development of dielectric antenna technology,” *Additional Conferences (Device Packaging, HiTEC, HiTEN, & CICMT)*. Accessed: 2016-08-15.
- [8] L. Huitema and T. Monediere, “Dielectric materials for compact dielectric resonator antenna applications,” *J.Appl. Phys.*, 2012.
- [9] A. Perron, T. A. Denidni, and A. R. Sebak, “Computer-aided design and analysis of dielectric resonator antennas,” *International Journal of RF and Microwave Computer-Aided Engineering*, vol. 20, no. 1, pp. 42–50, 2010.
- [10] W. Häland and G. H. Beall, *Glass-Ceramic Technology*. John Wiley Sons, Inc., 2012.
- [11] M. Vallet-Regí, “Ceramics for medical applications.” <http://pubs.rsc.org/en/content/articlehtml/2001/dt/b007852m>. Accessed: 2016-09-30.

-
- [12] I. M. Reaney and D. Iddles, "Microwave dielectric ceramics for resonators and filters in mobile phone networks," *Journal of the American Ceramic Society*, vol. 89, no. 7, pp. 2063–2072, 2006.
- [13] H. Braun, "Glass-ceramics with paraelectric phases for mobile applications in the GHz-range," *Master thesis*, 2011.
- [14] C. Barry, M. Carter, and G. Norton, *Ceramic Materials - Science and Engineering*. Springer-Verlag New York, 2013.
- [15] E. D. Zanotto, "A bright future for glass-ceramics." http://ceramics.org/wp-content/uploads/2010/09/bulletin_oct-nov2010.pdf. Accessed: 2016-06-30.
- [16] M. Mirsaneh, B. Zalinska, O. P. Leisten, and I. M. Reaney, "Bismuth niobate-based glass-ceramics for dielectrically loaded microwave antennas," *Functional Materials Letters*, vol. 01, no. 01, pp. 25–30, 2008.
- [17] R. Jakoby, "Glass ceramics with ferro- and paraelectric phases for microwave antennas - GLACER," *DFG project report*, 2014.
- [18] B. Hakki and P. Coleman, "A dielectric resonator method of measuring inductive capacities in the millimeter range," *IRE Transaction on Microwave Theory and Techniques*, vol. 15, pp. 402–410, 1960.
- [19] J. Baker-Jarvis, M. D. Janezic, B. Riddle, C. L. Holloway, N. G. Paulter, and J. Blendell, "Dielectric and conductor-loss characterization and measurements on electronic packaging materials," *NIST Technical Note 1520*, 2001.
- [20] H. Braun, "Titanate-based paraelectric glass-ceramics for applications in GHz electronics," *PhD thesis*, 2015.
- [21] S. B. Cohn and K. C. Kelly, "Microwave measurement of high-dielectric-constant materials," *IEEE Transactions on Microwave Theory and Techniques*, vol. 14, pp. 406–410, Sep 1966.
- [22] L. F. Chen, C. K. Ong, C. P. Neo, V. V. Varadan, and V. K. Varadan, *Microwave electronics measurement and materials characterisation*. Chichester: John Wiley, 2004.
- [23] W. E. Courtney, "Analysis and evaluation of a method of measuring the complex permittivity and permeability microwave insulators," *IEEE Transactions on Microwave Theory and Techniques*, vol. 18, pp. 476–485, Aug 1970.

- [24] L. Li, J. Y. Zhu, and X. M. Chen, "Measurement error of temperature coefficient of resonant frequency for microwave dielectric materials by $TE_{m01\delta}$ - mode resonant cavity method," *IEEE Transactions on Microwave Theory and Techniques*, vol. 64, pp. 3781–3786, Nov 2016.
- [25] J. Flemming, R. Cook, K. Dunn, and J. Gouker, "Cost-effective precision 3d glass microfabrication for advanced packaging applications," *Additional Conferences (Device Packaging, HiTEC, HiTEN, & CICMT)*, vol. 2012, no. DPC, pp. 000791–000810, 2012.
- [26] J. M. Nagarath and D. A. Wagenaar, "Ultradeep fused silica glass etching with an hf-resistant photosensitive resist for optical imaging applications," *Journal of Micromechanics and Microengineering*, vol. 22, no. 3, 2012.
- [27] C. Iliescu, B. Chen, and J. Miao, "Deep wet etching-through 1mm pyrex glass wafer for microfluidic applications," in *2007 IEEE 20th International Conference on Micro Electro Mechanical Systems (MEMS)*, pp. 393–396, Jan 2007.
- [28] W. Paper, "1/4 printed monopole antenna for 2.45ghz," *Nordic Semiconductor ASA*, pp. 1 – 6, 2005.
- [29] A. Kumar, V. Hamsakutty, J. Yohannan, and K. Mathew, "Microstripline fed cylindrical dielectric resonator antenna with a coplanar parasitic strip," *Progress in Electromagnetics Research*, vol. 60, pp. 143 – 152, 2006.
- [30] R. K. Mongia and P. Bhartia, "Dielectric resonator antennas—a review and general design relations for resonant frequency and bandwidth," *International Journal of Microwave and Millimeter-Wave Computer-Aided Engineering*, vol. 4, no. 3, pp. 230–247, 1994.
- [31] T. Yasin, "Optically transparent antennas for small satellites.," *Master thesis*, 2010.
- [32] M. J. R. Ons, *Integration of Antennas and Solar Cells for Autonomous Communication Systems*. PhD thesis, Dublin Institute of Technology, Dublin, 2010.
- [33] M. Tanaka, Y. Suzuki, K. Araki, and R. Suzuki, "Microstrip antenna with solar cells for microsattellites," *Electronics Letters*, vol. 31, pp. 5–6, Jan 1995.
- [34] O. Yurduseven, D. Smith, and M. Elsdon, "A dual-polarized solar cell stacked microstrip patch antenna with a $\lambda/4$ DC/RF isolation circuit for 5.8 ghz band wimax networks," in *The 8th European Conference on Antennas and Propagation (EuCAP 2014)*, pp. 1382–1385, April 2014.

- [35] O. O’Conchubhair, P. McEvoy, and M. J. Ammann, “Integrated antenna currents on a polycrystalline silicon solar cell,” in *2015 9th European Conference on Antennas and Propagation (EuCAP)*, pp. 1–4, May 2015.
- [36] S. V. Shynu, M. J. R. Ons, P. McEvoy, M. J. Ammann, S. J. McCormack, and B. Norton, “Integration of microstrip patch antenna with polycrystalline silicon solar cell,” *IEEE Transactions on Antennas and Propagation*, vol. 57, pp. 3969–3972, Dec 2009.
- [37] T. Yasin, “Transparent antennas for solar cell integration.,” *PhD thesis*, 2013.
- [38] T. W. Turpin and R. Baktur, “Meshed patch antennas integrated on solar cells,” *IEEE Antennas and Wireless Propagation Letters*, vol. 8, pp. 693–696, 2009.
- [39] S. Vaccaro, J. R. Mosig, and P. de Maagt, “Two advanced solar antenna ”solant” designs for satellite and terrestrial communications,” *IEEE Transactions on Antennas and Propagation*, vol. 51, pp. 2028–2034, Aug 2003.
- [40] J. R. Saberlin and C. Furse, “Challenges with optically transparent patch antennas for small satellites,” in *2010 IEEE Antennas and Propagation Society International Symposium*, pp. 1–4, July 2010.
- [41] A. Katsounaros, Y. Hao, N. Collings, and W. A. Crossland, “Optically transparent ultra-wideband antenna,” *Electronics Letters*, vol. 45, pp. 722–723, July 2009.
- [42] SCHOTT North America Incorporation, “New lasf35.” http://www.us.schott.com/d/advanced_optics/a01d62be-180d-498d-a796-d6293bc86387/1.0/schott-lasf35-april-2015-us.pdf.
- [43] S. Baglio, S. Gagliano, D. Neri, N. Savalli, and G. Tina, “Optimal design of photovoltaic systems for wireless sensor networks,” in *2008 IEEE International Symposium on Industrial Electronics*, pp. 2108–2113, June 2008.
- [44] K. Isoyama, T. Ohkuma, and D. Kawasaki, “Power saving wireless telemetering system.” <http://www.google.tl/patents/US7301477>, Nov. 27 2007. US Patent 7,301,477.
- [45] X. Jiang, J. Polastre, and D. Culler, “Perpetual environmentally powered sensor networks,” in *IPSN 2005. Fourth International Symposium on Information Processing in Sensor Networks, 2005.*, pp. 463–468, April 2005.
- [46] B. Pattan, *Satellite-Based Cellular Communications*. McGraw-Hill School Education Group, 1997.
- [47] L. A. Kosyachenko, *Solar Cells - Silicon Wafer-Based Technologies*. InTech, 2011.

- [48] C. COMPONENTS, “Solarzelle polykristallin conrad components yh-57x65 5 v 81 ma.” <https://www.conrad.de/de/solarzelle-polykristallin-conrad-components-yh-57x65-5-v-81-ma-191321.html?ref=list>.
- [49] E. Gazit, “Improved design of the vivaldi antenna,” *Microwaves, Antennas and Propagation, IEE Proceedings H*, vol. 135, pp. 89–92, Apr 1988.
- [50] J. Sor, W. Deal, Y. Qian, and T. Itoh, “A broadband quasi-yagi antenna array,” in *Microwave Conference, 1999. 29th European*, vol. 3, pp. 255–258, Oct 1999.
- [51] “A.L.L LASERTECHNIK GmbH.” <http://all-laser.de/>. Accessed: 2016-09-30.
- [52] W. L. Stutzman and G. A. Thiele, *Antenna Theory and Design, 3rd Edition*. John Wiley and Sons, Inc., 3 ed., June 2012, 2013.
- [53] F. Ellinger, *Radio Frequency Integrated Circuits and Technologies*. Berlin, Heidelberg: Springer Berlin Heidelberg, 2007.
- [54] O. H. Karabey, *Electronic Beam Steering and Polarization Agile Planar Antennas in Liquid Crystal Technology*. PhD thesis, Technische Universität, Darmstadt, 2014.
- [55] A. Gaebler, *Synthese steuerbarer Hochfrequenzschaltungen und Analyse Flüssigkristall-basierter Leitungsphasenschieber in Gruppenantennen für Satellitenanwendungen im Ka-Band*. PhD thesis, Technische Universität, Darmstadt, 2015.
- [56] M. Nikfalazar, *Beam-Steering Passive Phased Array with Integrated Printed Ferroelectric Phase Shifters*. PhD thesis, Technische Universität, Darmstadt, 2016.
- [57] C. Kohler, *Anorganische Barium-Strontium-Titanat-Komposite für die Hochfrequenztechnik : Material- und Bauteilentwicklung*. PhD thesis, TU Darmstadt, April 2016. Dissertation, Technische Universität Darmstadt, 2016.
- [58] M. Sazegar, *Phasedarray-Antennen mit integrierten Phasenschiebern auf ferroelektrischen Dickschichten*. PhD thesis, Technische Universität, Darmstadt, 2013.
- [59] Y.-Y. Bai, S. Xiao, M.-C. Tang, Z.-F. Ding, and B.-Z. Wang, “Wide-angle scanning phased array with pattern reconfigurable elements,” *Antennas and Propagation, IEEE Transactions on*, vol. 59, no. 11, pp. 4071–4076, 2011.
- [60] O. H. Karabey, “A 2-d electronically steered phased-array antenna with 2x2 elements in lc display technology,” *IEEE Tans. on Microwave Theory and Techniques*, vol. 60, pp. 1297–1305, 2012.

- [61] R. Coccioli and T. Itoh, "Design of photonic band-gap substrates for surface waves suppression," in *Microwave Symposium Digest, 1998 IEEE MTT-S International*, vol. 3, pp. 1259–1262 vol.3, 1998.
- [62] M. El Sabbagh and R. Mansour, "Ultra-wide suppression band of surface waves using periodic microstrip-based structures," *Microwave Theory and Techniques, IEEE Transactions on*, vol. 56, no. 3, pp. 671–683, 2008.
- [63] A. Kishk and W. Huang, "Size-reduction method for dielectric-resonator antennas," *Antennas and Propagation Magazine, IEEE*, vol. 53, no. 2, pp. 26–38, 2011.
- [64] A. Petosa, R. Larose, A. Ittipiboon, and M. Cuhaci, "Active phased array of dielectric resonator antennas," in *Antennas and Propagation Society International Symposium, 1997. IEEE., 1997 Digest*, vol. 2, pp. 690–693 vol.2, 1997.
- [65] A. Petosa, S. Thirakounc, M. Zuliani, and A. Ittipiboon, "Comparison between planar arrays of perforated dras and microstrip patches," in *Antennas and Propagation Society International Symposium, 2005 IEEE*, vol. 2A, pp. 168–175 vol. 2A, 2005.
- [66] R. Garg, P. Bhartia, I. Bahl, and A. Ittipiboon, *Microstrip Antenna Design Handbook*. Artech House Inc, 2000.
- [67] E. R. Brown, C. D. Parker, and E. Yablonovtich, "Radiation properties of a planar antenna on a photonic-crystal substrate," *J.Opt. Soc. Am. B*, vol. 10, pp. 404–407, Feb 1993.
- [68] D. Pozar, "Considerations for millimeter wave printed antennas," *IEEE Transactions on Antennas and Propagation*, vol. 31, pp. 740–747, Sep 1983.
- [69] D. R. Jackson and N. G. Alexopoulos, "Simple approximate formulas for input resistance, bandwidth, and efficiency of a resonant rectangular patch," *IEEE Transactions on Antennas and Propagation*, vol. 39, pp. 407–410, Mar 1991.
- [70] T. A. Milligan, *Modern antenna design*. Wiley-IEEE Press, 2005.
- [71] V. R. Komanduri, D. R. Jackson, J. T. Williams, and A. R. Mehrotra, "A general method for designing reduced surface wave microstrip antennas," *IEEE Transactions on Antennas and Propagation*, vol. 61, pp. 2887–2894, June 2013.
- [72] J.-G. Yook and L. P. B. Katehi, "Micromachined microstrip patch antenna with controlled mutual coupling and surface waves," *IEEE Transactions on Antennas and Propagation*, vol. 49, pp. 1282–1289, Sep 2001.

- [73] D. G. Fang, C. Z. Luan, and Y. P. Xi, "Mutual coupling in microstrip antenna array: evaluation, reduction, correction or compensation," in *IWAT 2005. IEEE International Workshop on Antenna Technology: Small Antennas and Novel Materials, 2005.*, pp. 37–40, March 2005.
- [74] M. M. Nikolic, A. R. Djordjevic, and A. Nehorai, "Microstrip antennas with suppressed radiation in horizontal directions and reduced coupling," *IEEE Transactions on Antennas and Propagation*, vol. 53, pp. 3469–3476, Nov 2005.
- [75] E. Rajo-Iglesias, O. Quevedo-Teruel, and L. Inclan-Sanchez, "Mutual coupling reduction in patch antenna arrays by using a planar ebg structure and a multilayer dielectric substrate," *IEEE Transactions on Antennas and Propagation*, vol. 56, pp. 1648–1655, June 2008.
- [76] M. A. Khalid, "Mutual coupling and beam steering analysis of patch and dielectric resonator antenna arrays," *Master thesis*, 2015.
- [77] R. Chair, A. A. Kishk, and K.-F. Lee, "Comparative study on the mutual coupling between different sized cylindrical dielectric resonators antennas and circular microstrip patch antennas," *IEEE Transactions on Antennas and Propagation*, vol. 53, pp. 1011–1019, March 2005.
- [78] PREMIX, "Preperm® – dielectric plastics for optimal rf performance." <http://www.premixgroup.com/product-cats/hf-plastics/preperm/>, 2016.
- [79] K. Onur and B. Saygin, "Continuously polarization reconfigurable antenna element by using liquid crystal based tunable coupled line," *Electronic*, vol. 48, p. 3, 2012.
- [80] K. Onur, "Tunable loaded line phase shifters for microwave applications," *IEEE MTT-S International*, vol. 1, pp. 1–4, 2011.
- [81] F. Goelden, *Liquid Crystal Based Microwave Components with Fast Response Times: Material, Technology, Power Handling Capability. PHD.Thesis*. PhD thesis, Technische Universitaet Darmstadt, 2009.
- [82] M. Sazegar, A. Mehmood, Y. Zheng, H. Maune, and R. Jakoby, "Integrated resistive bias network for tunable devices on ferroelectric ceramics," in *Microwave Conference (EuMC), 2011 41st European*, pp. 1071–1074, Oct 2011.
- [83] SCHOTT, "Schott borofloat 33." http://psec.uchicago.edu/glass/borofloat_33_e.pdf.
- [84] A. Mehmood, Y. Sun, Y. Zheng, O. H. Karabey, H. Braun, M. Hovhannisyan, M. Letz, and R. Jakoby, "Compact dual-band hybrid dielectric resonator antenna

based on new glass-ceramic material,” in *Microwave Conference (EuMC), 2013 European*, pp. 763–766, 2013.

- [85] EVONIK, “Rohacell® hf: negligible absorption in the high frequency range.” <http://www.rohacell.com/product/rohacell/en/products-services/rohacell-hf/pages/default.aspx>, 2016.

Awards and Publications

Award

1. Best paper award for paper "Dual Band Dielectric Resonator Antenna For Hiperlan Based on Transparent Glass Material," in German Microwave Conference (GeMIC) - 2014 , Aachen-Germany.

Journals

1. Arshad Mehmood, Onur Hamza Karabey, Rolf Jakoby, "Dielectric Resonator Antenna with Tilted Beam", IEEE Antennas and Propagation Letters. December-2016
2. Hubertus Braun, Arshad Mehmood, Martun Hovhannisyan, Huairuo Zhang, Damoon Sohrabi Baba Heidary, Clive Randall, Michael T Lanagan, Rolf Jakoby, Ian M Reaney, Martin Letz, Hans-Joachim Elmers, "Microwave properties and structure of La-Ti-Si-B-O glass-ceramics for applications in GHz electronics", Journal of the European Ceramic Society, Aug 2016
3. Arshad Mehmood, Yuliang Zheng , Hubertus Braun, Martun Hovhannisyan , Martin Letz , Rolf Jakoby, "High dielectric low loss transparent glass material based dielectric resonator antenna with wide bandwidth operation", Frequenz 2015 , 69(1-2): 21-27
4. Karabey, O.H.; Mehmood, A.; Ayluctarhan, M.; Braun, H.; Letz, M.; Jakoby, R., "Liquid crystal based phased array antenna with improved beam scanning capability," Electronics Letters , vol.50, no.6, pp.426,428, March 13 2014
5. M. Nikfalazar ; A. Mehmood ; M. Sohrabi ; M. Mikolajek ; A. Wiens ; H. Maune ; C. Kohler ; J. R. Binder ; R. Jakoby, "Steerable Dielectric Resonator Phased-Array Antenna Based on Inkjet-Printed Tunable Phase Shifter With BST Metal-Insulator-Metal Varactors," in IEEE Antennas and Wireless Propagation Letters, vol. 15, no. , pp. 877-880, 2016.

6. Mohammad Nikfalazar ; Christian Kohler ; Alex Wiens ; Arshad Mehmood ; Mojtaba Sohrabi ; Holger Maune ; Joachim R. Binder ; Rolf Jakoby "Beam Steering Phased Array Antenna With Fully Printed Phase Shifters Based on Low-Temperature Sintered BST-Composite Thick Films," in IEEE Microwave and Wireless Components Letters, vol. 26, no. 1, pp. 70-72, Jan. 2016.

Conferences

1. Arshad Mehmood, Onur Hamza Karabey, Muhammed Ayluctarhan, Yuliang Zheng, Hubertus Braun, Martun Hovhannisyan, Martin Letz and Rolf Jakoby, "Dielectric Resonator Antenna Phased Array with Liquid Crystal Based Phase Shifters". Antenna and Propagation (EuCAP) European, April 2014.
2. A. Mehmood, M. Nikfalazar, M. Sohrabi, R. Jakoby, M. Hovhanisyan and M. Letz, "Bulk-glass ceramic based stacked dielectric resonator antenna as phased array element," 2015 European Radar Conference (EuRAD), Paris, 2015, pp. 309-312.
3. M. Nikfalazar ; A. Mehmood ; M. Sohrabi ; A. Wiens ; Y. Zheng ; H. Maune ; R. Jakoby ; M. Mikolajek ; A. Friederich ; C. Kohler ; J. R. Binder, "Low bias voltage tunable phase shifter based on inkjet-printed BST MIM varactors for C/X-band phased arrays," 2015 10th European Microwave Integrated Circuits Conference (EuMIC), Paris, 2015, pp. 413-416.
4. Erick González-Rodríguez ; Arshad Mehmood ; Yuliang Zheng ; Holger Maune ; Lufei Shen ; Jing Ning ; Hubertus Braun ; Martun Hovhannisyan ; Klaus Hofmann ; Rolf Jakoby, "Reconfigurable dualband antenna module with integrated high voltage charge pump and digital analog converter," The 8th European Conference on Antennas and Propagation (EuCAP 2014), The Hague, 2014, pp. 2749-2753.
5. Mehmood, Arshad; Zheng, Yuliang; Braun, Hubertus; Braun, Hubertus; Hovhannisyan, Martun; Hovhannisyan, Martun; Letz, Martin; Jakoby, Rolf, "Dual Band Dielectric Resonator Antenna For Hiperlan Based on Transparent Glass Material," Microwave Conference (GeMIC), 2014 German , vol., no., pp.1,4, 10-12 March 2014
6. Mehmood, A.; Yue Sun; Yuliang Zheng; Karabey, O.H.; Braun, H.; Hovhannisyan, M.; Letz, M.; Jakoby, R., "Compact dual-band hybrid dielectric resonator antenna based on new glass-ceramic material," Microwave Conference (EuMC), 2013 European , vol., no., pp.763,766, 6-10 Oct. 2013
7. M. Sazegar, A. Mehmood, Y. Zheng, H. Maune, R. Jakoby, "Integrated resistive bias network for tunable devices on ferroelectric Ceramics", European Microwave Conference- Publication Year: 2011.

8. Sazegar, M.; Mehmood, A.; Yuliang Zheng; Maune, H.; Xianghui Zhou; Binder, J.; Jakoby, R. "Compact tunable loaded line phase shifter based on screen printed BST thick film" Microwave Conference (GeMIC), 2011 Germany. Publication Year: 2011, Page(s): 1 - 4

Supervised Work

1. Jianchun Mai: Investigation of Multilayer Compact tunable antennas Based on Ferroelectric Ceramics for Multiband Applications. Master thesis D2172. Technische Universität Darmstadt, 2011
2. Yue Sun: Multiband and multiport Dielectric resonator antennas based on Glass-ceramics. Master thesis D2186-M. Technische Universität Darmstadt, 2012
3. Muhammed Ayluctarhan: Investigation on beam steering of dielectric resonator antennas in Liquid Crystal technology. Master thesis D2195-M. Technische Universität Darmstadt, 2013
4. Mojtaba Sohrabi: Dielectric resonator phased array with Inkjet printed tunable ferroelectric MIM-Varactors phase shifters. Master thesis D2224-M. Technische Universität Darmstadt, 2015
5. Muhammad Ali Khalid: Mutual coupling and beam steering of patch and dielectric resonator antenna arrays. Master thesis D2233-M. Technische Universität Darmstadt, 2015

SCHOTT GHz 33 glass-ceramic

Glass-ceramic dielectric for microwave electronics – Preliminary datasheet



Possible shapes of SCHOTT GHz 33 glass-ceramic

Product Information

SCHOTT GHz 33 glass-ceramic is a high performance dielectric material for applications in antenna and filter elements. It offers an excellent material homogeneity and its completely pore free structure allows metallic structures with excellent electrical properties. As a GHz dielectric material SCHOTT GHz 33 glass-ceramic is based on a novel material class: a bulk glass ceramic.

Advantages

SCHOTT GHz 33 glass-ceramic allows to design highly accurate resonating and radiating structures in antenna and filter applications:

- Miniaturization of antenna and filter structures due to a dielectric constant of $\epsilon' = 33.7$
- Low loss material
- High material homogeneity, derived from optical glass production allows highly accurate designs with MHz accuracy in GHz applications.
- Intrinsic pore free structure gives superior metallization properties

SCHOTT GHz 33 glass-ceramic is the dielectric for antenna and filter elements in microwave electronic. Its high homogeneity allows for accurate designs of resonating structures and its intrinsic pore free nature makes superior metal to dielectric interfaces.

About SCHOTT

SCHOTT is an international technology group with 130 years of experience in the areas of specialty glasses and glass ceramics. More than 600 scientists and engineers are working for and with SCHOTT customers all over the world, while setting the pace by developing new, cutting edge technologies for the requirements of today and tomorrow.

The SCHOTT Group with a workforce of about 16,000 employees maintains close proximity to its customers with manufacturing and sales units in 35 different countries.

SCHOTT
glass made of ideas

SCHOTT GHz 33 glass-ceramic

Glass-ceramic dielectric for microwave electronics – Preliminary datasheet

Quantity	Value / Unit	Remark	Measurement
Dielectric constant, ϵ	33.7	at 7.2 GHz	dielectric resonance spectroscopy
Dielectric loss, $\tan\delta$	1.5E-3	at 7.2 GHz	dielectric resonance spectroscopy
Quality factor, Q	653	at 7.2 GHz	dielectric resonance spectroscopy
Q f	4736 GHz	at 7.2 GHz	dielectric resonance spectroscopy
Temperature coefficient of resonance, τ_f	61 ppm/K	at 7.2 GHz	
Material homogeneity $\Delta\epsilon/\epsilon$	<0.1 %	current estimation for later production value	
residual porosity	none		
Knoop hardness	953		
E-modulus	162 GPa		
shear modulus	63 GPa		
Poisson number, ν	0.28		
Available dimensions	thickness: 0.2 mm – 23 mm diameter of round cylinders: 0.5 mm – 115 mm Maximum size of blocks: 115 mm x 300 mm		

Important notice: Listed measured values are from development samples. Production samples may have different values or property combinations. Values for development samples might vary from batch to batch. Samples from the same batch show high homogeneity however.

Further properties

Excellent metal adhesion

SCHOTT AG
Research & Development
Dr. Martin Letz
55128 Mainz, Germany
Phone +49 (0)6131/66-3539
martin.letz@schott.com

www.schott.com

SCHOTT
glass made of ideas

Curriculum Vitae

Personal Details

Name Arshad Mehmood
Date of Birth 01 March 1984
Place of Birth Peshawar, Pakistan

Education

1989-1999 Army Public School (SSC - 10th grade)- Bahawalpur , Pakistan
1999-2001 Army Burnhall College (HSSC - 12th grade) - Abbottabad, Pakistan
2001-2005 Computer Engineering (B.Sc) - COMSATS - Abbottabad, Pakistan
2007-2010 Information and Comm. Engineering (M.Sc) - Technische Universität Darmstadt, Germany

Professional Career

2011-2016 Research Assistant, Institute of Microwave Engineering and Photonics, Technische Universität Darmstadt, Germany
2014-2016 RF/Antenna Engineer ALCAN Project, Institute of Microwave Engineering and Photonics, Technische Universität Darmstadt, Germany

Darmstadt, 30 January 2017